
ETD Archive

2014

Numerical Investigation of Boiling in a Sealed Tank in Microgravity

Sonya Lynn Hylton
Cleveland State University

Follow this and additional works at: <https://engagedscholarship.csuohio.edu/etdarchive>

 Part of the [Mechanical Engineering Commons](#)

How does access to this work benefit you? Let us know!

Recommended Citation

Hylton, Sonya Lynn, "Numerical Investigation of Boiling in a Sealed Tank in Microgravity" (2014). *ETD Archive*. 489.

<https://engagedscholarship.csuohio.edu/etdarchive/489>

This Thesis is brought to you for free and open access by EngagedScholarship@CSU. It has been accepted for inclusion in ETD Archive by an authorized administrator of EngagedScholarship@CSU. For more information, please contact library.es@csuohio.edu.

NUMERICAL INVESTIGATION OF BOILING IN A SEALED TANK IN
MICROGRAVITY

SONYA LYNN HYLTON

Bachelor of Science in Mechanical Engineering
Cleveland State University
June 2007

Submitted in partial fulfillment of requirements for the degree
MASTER OF SCIENCE IN MECHANICAL ENGINEERING
at the
CLEVELAND STATE UNIVERSITY
January 2015

© Copyright by Sonya Lynn Hylton 2014

We hereby approve this thesis for

Sonya Lynn Hylton

Candidate for the Master of Science in Mechanical Engineering degree for the

Department of Mechanical Engineering

and the CLEVELAND STATE UNIVERSITY

College of Graduate Studies

Thesis Chairperson, Dr. Mounir Ibrahim

Department & Date

Thesis Committee Member, Dr. Mohammad Kassemi

Department & Date

Thesis Committee Member, Dr. Olga Kartuzova

Department & Date

Student's Date of Defense: December 3, 2014

ACKNOWLEDGEMENTS

I am very grateful to all of the people who aided me. Without their help, this endeavor would not have been possible.

In particular, I would like to thank Dr. Mounir Ibrahim, my academic advisor, for all of his support and encouragement. I'm also very grateful to Dr. Mohammad Kassemi, my research advisor, for his support, advice, and encouragement. I am indebted to Dr. Olga Kartuzova, my committee member, for all of her help and advice on model development.

Thanks go also to the NASA Microgravity and International Space Station program for their overall support. Dr. Mohammad Hasan's help was also very valuable. Mark Stewart's advice regarding under-relaxation factors was very helpful. I also would like to thank Dr. Jeffrey Moder for his invaluable assistance regarding the specifics of the TPCE/TP experiment and providing access to the movies taken of this experiment. In addition, I would like to thank Michael Bentz for his email correspondence regarding details of the TPCE/TP experiment.

Finally, special thanks go to my friends and family members whose encouragement and support made this work possible.

NUMERICAL INVESTIGATION OF BOILING IN A SEALED TANK IN MICROGRAVITY

Sonya Lynn Hylton

ABSTRACT

NASA's missions in space depend on the storage of cryogenic fluids for fuel and for life support. During long-term storage, heat can leak into the cryogenic fluid tanks. Heat leaks can cause evaporation of the liquid, which pressurizes the tank. However, when the tanks are in a microgravity environment, with reduced natural convection, heat leaks can also create superheated regions in the liquid. This may lead to boiling, resulting in much greater pressure rises than evaporation at the interface between the liquid and vapor phases. Models for predicting the pressure rise are needed to aid in developing methods to control the pressure rise, so that the safety of the storage tank is ensured for microgravity operations.

In this work, a CFD model for predicting the pressure rise in a tank due to boiling has been developed and validated against experimental data. The tank was modeled as 2D axisymmetric. The Volume of Fluid (VOF) model in ANSYS Fluent version 15 was modified using a User Defined Function (UDF) to calculate mass transfer between the liquid and vapor phases. A kinetic based Schrage equation was used to calculate the mass flux for evaporation and condensation at the interface. The Schrage equation and the Lee model were compared for calculating the evaporation due to boiling that occurred in the bulk liquid. The results of this model were validated against microgravity data provided

by the Tank Pressure Control Experiment, a tank pressurization and pressure control experiment performed aboard the Space Shuttle Mission STS-52 that experienced boiling. During this experiment, the tank pressure rose from about 43400 Pa to about 47200Pa, a difference of about 3800 Pa. The heater temperature rose from about 296K to about 303K, a difference of about 7K.

The tank pressure predicted by the CFD model compared well with the experimental pressure data for self-pressurization and boiling in the tank. The validated CFD model uses the Schrage equation to calculate the mass transfer. Three different accommodation coefficients were used, one for evaporation at the interface, one for condensation at the interface, and one for boiling in the bulk liquid. The implicit VOF model with bounded second order time discretization was used.

TABLE OF CONTENTS

ABSTRACT	v
LIST OF FIGURES	x
LIST OF TABLES	xv
NOMENCLATURE	xvi
I. INTRODUCTION	1
II. LITERATURE REVIEW	3
Tank Pressure Models	3
Boiling Models	6
Tank Pressurization due to Boiling	11
III. THE TANK PRESSURE CONTROL EXPERIMENT: THERMAL PHENOMENA	12
Test 6	18
IV. MATHEMATICAL MODEL	31
Schrage Equation	34
Lee Model	37
V. NUMERICAL IMPLEMENTATION	39
Tank Dimensions and Properties	40
Thermistor Locations	42
Fluent Setup	43

Initial Location of the Ullage.....	45
VI. RESULTS	46
CFD Model of the TPCE—Preliminary Numerical Verification.....	46
Mesh Independence	46
Gravity Study.....	51
CFD Simulation of the Self-Pressurization Period during Test 6	54
Time Step Size Independence Study for Self-Pressurization Period.....	55
Initial Conditions	57
Results of the Self-Pressurization Study	63
CFD Simulation of the Boiling Period during Test 6	68
Under-Relaxation Factor for Mass Transfer Calculations in the UDF.....	69
Time Step Independence Study for Boiling	70
Boiling Threshold Superheat Temperature Study	72
Mass Transfer Model 1: Lee Model	73
Mass Transfer Model 2: Schrage Equation	75
Final Boiling Model.....	93
VII. SUMMARY AND CONCLUSION	95
Summary of Work Performed	95
Conclusion.....	99
Suggestions for Future Work	100

BIBLIOGRAPHY	102
APPENDIX.....	107
FLUID PROPERTIES	108
CURVE FITS OF THE TEMPERATURE AT HEATER A	116

LIST OF FIGURES

Figure 1: Tank Shape and Dimensions in cm (in) (Hasan, Lin, Knoll, & Bentz, 1996)...	13
Figure 2: Schematic of the Tank Assembly (Bentz, 1993).....	14
Figure 3: Schematic of the Main Components of the Experiment (Bentz, 1993).....	14
Figure 4: Photo of various components inside the tank (Hasan, Lin, Knoll, & Bentz, 1996)	15
Figure 5: Schematic of Heater with Dimensions in cm (in) (Hasan, Lin, Knoll, & Bentz, 1996)	16
Figure 6: Data from TPCE/TP Test 6 (Hasan, Lin, Knoll, & Bentz, 1996): (a) Pressure, (b) Fluid temperatures, (c) Heater temperatures, (d) Power applied to heater A, (e) Flow rate.....	20
Figure 7: Pressure during test 6 of the TPCE/TP experiment (digitized) (dashed vertical lines are to show the times at which images were obtained from the movie of the experiment)	21
Figure 8: Fluid temperatures during test 6 of the TPCE/TP experiment (digitized)	21
Figure 9: Heater temperatures during test 6 of the TPCE/TP experiment (digitized)	22
Figure 10: Pressure and Heater Power during test 6 of the TPCE/TP experiment (digitized).....	22
Figure 11: Pressure and Flow Rate during test 6 of the TPCE/TP experiment (digitized)	23
Figure 12: Images of test 6 taken during the heating phase of the TPCE/TP experiment (NASA STI Program, 2012)	26
Figure 13: Range of superheat temperatures required to initiate boiling in Freon 113 for various cavity sizes	27

Figure 14: Schematic of Computational Domain	31
Figure 15: Thermistor locations in the axisymmetric case setup.....	43
Figure 16: Initial locations of the ullage in the model (a) top of ullage 5mm from heater, (b) top of ullage 30mm from heater	45
Figure 17: Time step size independence study for self-pressurization: Pressure	56
Figure 18: Time step independence study for self-pressurization: Temperature on bottom surface of heater	56
Figure 19: Pressure rise during initial self-pressurization case	58
Figure 20: Temperature at T1 during initial self-pressurization case	58
Figure 21: Temperature at T2 during initial self-pressurization case	59
Figure 22: Temperature at T3 during initial self-pressurization case	59
Figure 23: Temperature at T4 during initial self-pressurization case	60
Figure 24: Temperature at T5 during initial self-pressurization case	60
Figure 25: Curve fit of the initial temperatures in the tank as measured by all six thermistors inside the tank	62
Figure 26: Curve fit of the initial temperatures in the tank as measured by thermistors T1, T2, T3, and T5	62
Figure 27: Initial temperature gradient imposed on the tank (a) top of ullage 5mm from heater, (b) top of ullage 30mm from heater	64
Figure 28: Pressure rise during self-pressurization.....	64
Figure 29: Temperature at T1 during self-pressurization	65
Figure 30: Temperature at T2 during self-pressurization	65
Figure 31: Temperature at T3 during self-pressurization	66

Figure 32: Temperature at T4 during self-pressurization	66
Figure 33: Temperature at T5 during self-pressurization	67
Figure 34: Effect of the under-relaxation factor applied to mass transfer on the pressure rise during boiling	69
Figure 35: Time step size independence study for boiling using the explicit VOF scheme	71
Figure 36: Time step size independence study for boiling using the implicit VOF scheme	72
Figure 37: Effect of different threshold superheats required for boiling to occur	73
Figure 38: Pressure rise: effect of different values for the Lee model coefficient	74
Figure 39: Pressure rise: effect of different Schrage equation accommodation coefficients	75
Figure 40: Pressure rise: effect of varying a single accommodation coefficient.....	76
Figure 41: Pressure rise: different accommodation coefficients used for evaporation and condensation	77
Figure 42: Pressure rise: different accommodation coefficients used for boiling, evaporation, and condensation.....	78
Figure 43: Pressure rise: three different accommodation coefficients: effect of varying condensation accommodation coefficient.....	79
Figure 44: Boiling using the implicit VOF scheme, with bounded second order time discretization	80
Figure 45: Comparison between the PISO and coupled schemes for pressure-velocity coupling.....	81

Figure 46: Effect of varying the threshold temperature for boiling.....	82
Figure 47: Pressure curves from the four best boiling cases (dashed vertical lines are to show the times at which temperature contour plots were taken from the simulations), (a) entire boiling period, (b) beginning of the boiling period	83
Figure 48: Temperature at T1 during the four best boiling cases	84
Figure 49: Temperature at T2 during the four best boiling cases	84
Figure 50: Temperature at T3 during the four best boiling cases	85
Figure 51: Temperature at T4 during the four best boiling cases	85
Figure 52: Temperature at T5 during the four best boiling cases	86
Figure 53: Temperature contour plots for the explicit VOF case using PISO and a threshold temperature of 3K	87
Figure 54: Temperature contour plots for the implicit VOF case using PISO and a threshold temperature of 3K	89
Figure 55: Temperature contour plots for the implicit VOF case using the coupled pressure-velocity coupling scheme and a threshold temperature of 3K	91
Figure 56: Temperature contour plots for the implicit VOF case using PISO and a threshold temperature of 1K	92
Figure 57: Pressure curve calculated using the best boiling model	94
Figure 58: Saturation pressure of Freon 113.....	108
Figure 59: Vapor Density of Freon 113	109
Figure 60: Vapor Thermal Conductivity of Freon 113	109
Figure 61: Vapor Viscosity of Freon 113	110
Figure 62: Vapor Specific Heat of Freon 113.....	110

Figure 63: Vapor Enthalpy of Freon 113	111
Figure 64: Surface Tension of Liquid Freon 113.....	111
Figure 65: Liquid Thermal Conductivity of Freon 113	112
Figure 66: Liquid Viscosity	112
Figure 67: Liquid Specific Heat of Freon 113	113
Figure 68: Liquid Enthalpy of Freon 113	113
Figure 69: Liquid Density of Freon 113	114
Figure 70: Liquid Thermal Expansion Coefficient of Freon 113	115
Figure 71: Curve fits of T3 during test 6	117
Figure 72: Curve fits of T3 during test 6: zoomed in	118

LIST OF TABLES

Table 1: Summary of the various tests performed during the TPCE/TP experiment	17
Table 2: Estimate of the tank's saturation temperature during boiling	29
Table 3: $Gr_x \cdot Pr$ and Gr during test 6 of the TPCE/TP experiment	30
Table 4: Fluid properties used in the cases	42
Table 5: Mesh Independence Study	48
Table 6: Effect of Gravity	53
Table 7: Temperature contours in the tank at the end of the self-pressurization period, as calculated by the model	68
Table 8: Summary of Work Performed	98
Table 9: Curve Fits of T3 during test 6.....	116

NOMENCLATURE

A = Interface area density (1/m)

E = energy (J)

\vec{g} , g = gravity (m/s²)

h = enthalpy (J/kg)

k_{eff} = effective thermal conductivity (W/(m*K))

\dot{m} = mass flux (kg/(s*m²))

M = molecular weight (kg/kmol)

P = pressure (Pa)

r = radius (m)

R_u = universal gas constant (J/kmol*K)

S_h = energy source term (W/m³)

t = time (s)

T = temperature (K)

\vec{v} = velocity (m/s)

v = specific volume (m³/kg), velocity magnitude (m/s)

V = volume (m³)

Greek

α = phase volume fraction (unitless)

β = thermal expansion coefficient (1/K)

μ = dynamic viscosity (kg/(m*s))

ρ = density (kg/m³)

σ = surface tension (N/m), accommodation coefficient (unitless)

Subscripts

b = boiling

c = condensation

$cell$ = conditions in a cell of the mesh

e = evaporation

fg = difference between the saturated liquid and saturated vapor properties

i = interface, phase

j = phase

l = liquid

sat = saturation conditions

sh = superheat temperature

v = vapor

$total$ = vapor and noncondensable gas

Acronyms

CFD: Computational Fluid Dynamics

PISO: Pressure-Implicit Splitting of Operators

TPCE/TP: Tank Pressure Control Experiment: Thermal Phenomena

UDF: User Defined Function

VOF: Volume of Fluid

CHAPTER I

INTRODUCTION

NASA's missions to the moon, Mars, or even the International Space Station depend on cryogenic fluid storage for fuel and for life support systems (Panzarella & Kassemi, 2002). As such, a great deal of work has been put into trying to manage cryogenic fluids, including transferring the liquid, gauging how much liquid remains, and storing cryogenics for long durations (Meyer, et al., 2013). Since cryogenics must be stored at low temperatures, heat from various sources can leak into cryogenic storage tanks. This heat causes the temperature and pressure inside the tank to increase. Models for predicting the pressure rise are needed to aid in developing methods to control the pressure rise.

Since cryogenic tanks are used in a microgravity environment with very little natural convection, it is possible for localized superheats to develop (Hasan & Balasubramaniam, 2012). These superheats can become significantly hotter than the saturation temperature of the tank pressure, and therefore can cause boiling. Boiling can be explosive, and can create pressure spikes in the tank of significant magnitude compared to the tank pressure just before boiling occurred (Hasan, Lin, Knoll, & Bentz, 1996). Limiting the heat flux into the tank to low levels will not necessarily prevent boiling.

In order to control the pressure in a tank in microgravity, it is necessary to be able to predict the pressure rise inside the tank due to boiling. The objective of this thesis is to develop and validate an engineering Computational Fluid Dynamics (CFD) model to capture this phenomenon. A literature review is presented in Chapter 2. Chapter 3 describes the experiment which was used to validate the model. Chapter 4 describes the mathematical model used, while Chapter 5 describes the numerical implementation of this model. The results of the model are presented in Chapter 6, and conclusions and suggestions for future work are discussed in Chapter 7.

CHAPTER II

LITERATURE REVIEW

Tank self-pressurization due to heat leaks has been studied extensively, using experimental, theoretical, and numerical methods (Meyer, et al., 2013). Boiling has also been studied using similar methods. However, the pressure rise inside a tank due to boiling in microgravity has not been studied as extensively.

Tank Pressure Models

The pressure rise inside a tank due to evaporation at the interface has been studied using models of different degrees of complexity. Aydelott (1967) described several small-scale experiments regarding the pressurization of small-scale tanks filled with a mixture of liquid and vapor hydrogen, and compared the pressurization data from these experiments with results from two thermodynamic models. He began by explaining that since liquid hydrogen is stored at a low temperature, it's difficult to prevent heat from leaking into the tank. As this happens, it is possible for the liquid to be subcooled even when the vapor is superheated. The interface between the two phases will be at the saturation temperature of the "system pressure." He used two thermodynamic models to predict the pressure in the experimental tanks over time; one model assumed the temperature in the tank was

homogeneous at all times, while the second model assumed that all of the heat leaking into the tank was used to evaporate the liquid and heat the vapor. He stated that since the tank was not really in a thermodynamic state of equilibrium, a thermodynamic analysis could not predict the pressure rise well; his comparison of the models' predictions to the experimental results showed that his models did not match the data well.

Panzarella and Kassemi (2002) developed an active liquid-lumped vapor (ALLV) model of the pressure in a tank filled with liquid and vapor, which coupled transport equations in the liquid to thermodynamic relations describing the vapor. The mass, momentum and energy equations were solved for the liquid region, allowing the flow in the liquid to affect the pressure rise in the tank. The vapor, however, was treated in a lumped fashion such that the temperature and pressure of the vapor were assumed to be spatially constant throughout the vapor region, though they could vary with time. The liquid and vapor regions were coupled together via heat and mass transfer across the interface. Heat was added to the tank in three different configurations (liquid heating, vapor heating, and uniform heating) and the results from the model were compared to a thermodynamic analysis of the same tank. Once the tank reached a steady state, the rate of pressure rise as calculated by the model was equal to that calculated by the thermodynamic model; however, the initial transients and the actual pressure did not match the predictions made by the thermodynamic model. The general trends resulting from this model were compared to the trends shown by Aydelot; they compare better than the trends predicted by the thermodynamic model.

Barsi et al. (2007) developed an active vapor-active liquid (ALAV) model of a two-phase cryogenic tank. In this model, the mass, momentum, and energy equations were

solved in both the liquid and vapor phases, but the mass transfer between the phases was treated in a lumped fashion. The interface between the phases was sharp and rigid. They used this model to predict the pressure rise in a tank undergoing liquid heating, vapor heating, and uniform heating, and compared the predicted pressure rise to predictions made by the ALLV model developed earlier by Panzarella and Kassemi (2002). The ALAV model (Barsi, Panzarella, & Kassemi, 2007) predicted the same pressure rise as the ALLV model for the liquid heating configuration; however, for the vapor heating configuration it predicted a higher pressure rise. For the uniform heating configuration, it predicted a pressure rise between the other two heating configurations. Barsi et al. explained that the ALLV model assumes that the vapor is saturated, which is a good assumption for the liquid heating configuration. However, since the vapor is superheated in a vapor heating configuration, the predictions of the ALAV model are more accurate.

Kartuzova and Kassemi (2011) developed two models of two-phase cryogenic tanks; one used a sharp interface, and one used the Volume of Fluid (VOF) method. (The sharp interface model uses a sharp interface between the liquid and vapor phases, which does not move. In the VOF model (ANSYS, 2013a), the interface and its motion are captured in a diffuse manner by tracking the volume fraction of each fluid (Kartuzova & Kassemi, 2011).) In both models, the transport equations were solved in both the liquid and vapor phases. At the interface, the mass transfer was calculated and applied via a source term in the VOF model, while the energy, mass, velocity and shear stresses were applied as boundary conditions at the interface. These calculations were performed in User Defined Functions which were used to customize ANSYS Fluent, a commercial CFD code. Kartuzova and Kassemi used these models to study the effect of turbulence at the interface

on the rate of tank pressure, and validated their results against experimental results from the Saturn S-IVB AS-203 experiment. The VOF model was able to predict the pressure rise seen in the experiment better, due in part to the fact that the interface was able to deform in this model. However, the simulations using the VOF model were more computationally intensive than the simulations using the Sharp Interface model.

Boiling Models

Boiling has also been studied using models of varying degrees of complexity. Many of these models attempt to predict the growth rate of the bubbles, since this affects the heat transfer (Mei, Chen, & Klausner, 1995a). van Stralen, Sohal, et al. (1975) surveyed the existing theories of heterogeneous bubble growth, which involved either the evaporation microlayer or the relaxation microlayer. (The microlayer is a thin layer of liquid between a bubble and the heated surface the bubble is growing on. The microlayer transfers heat to the bubble and also provides vapor to the bubble as it evaporates.) They then proposed a theoretical model which incorporates both effects on the growth of a bubble during the time the bubble is in contact with the wall. They also discussed the radius of the contact area between the bubble and the wall, temperature fluctuations at the wall as bubbles grow on it and then leave, and turbulent flow in the liquid and inside the bubble during rapid bubble growth. van Stralen, Cole, et al. (1975) validated their model of heterogeneous bubble growth via an experiment with water boiling at subatmospheric pressures in 1g; their model agrees well with the experimental data.

Mie et al. (1995a) developed a numerical model of bubble growth for a large range of heterogeneous boiling conditions. They used empirical data for the shape of the bubble, and concentrated on the heat transfer from the heater through the liquid microlayer to the

bubble. In particular, they studied how the variation in temperature of the heater surface, with respect to time and space, affects bubble growth. They also limited their analysis to saturation conditions by ignoring the heat transfer to the domed surface of the bubble. Since the hydrodynamics were ignored, the wedge angle of the liquid microlayer between the bubble and the heater wall was determined empirically; this angle was a key factor in enabling their model to predict the rate of bubble growth accurately. In this study, four dimensionless parameters were determined to be most important in affecting the bubble growth rate: Ja (Jacob number), Fo (Fourier number) of the solid, κ (liquid-to-solid conductivity ratio), and α (liquid-to-solid thermal diffusivity ratio). In a following paper, Mie et al. (1995b) studied the effect of each of these dimensionless parameters on both the growth rate of the bubble and on the temperature distribution in the heater.

Lee and Merte (1996) developed a Fortran-based numerical model of homogeneous bubble growth in a superheated liquid. They assumed the bubble would always be spherical, and that the liquid had a uniform temperature. The effects of surface tension, which affects the early growth rate of the bubble, were included. An artificial initial disturbance in the temperature was used to initiate the growth of the bubble. The bubble radius predicted by this model was then compared to experimental results for water; the model agreed fairly well with the data, but the initial disturbance did affect the bubble growth predicted by the model at low superheats. Their model was also compared to previous analytical and numerical models; their model seems to compare well with these other models, with the exception of the initial period which some of these models did not capture, since they neglected the effects of surface tension.

Son et al. (1999) developed a laminar axisymmetric numerical model of bubble growth where the bubble shape was allowed to change using a level set method, which meant that the bubble was able to depart from the heater surface. (The level set method developed by Sussman et al. (1994) was developed for modeling incompressible two-phase flows, where the two phases could have very different densities and viscosities from each other. The interface, which was allowed to move, would remain sharp through the entire simulation. Son et al. (1999) altered this level set method to include phase change.) The computational domain did not extend far into the fluid by the heater's surface. Each bubble was initialized as a nucleus inside the cavity and allowed to grow. The effects of the microlayer between the bubble and the heater wall were included. Constant properties were used for the fluid. In this work, an experiment was performed which they used to validate the results from their model; they also used data from other experiments for validation purposes. The contact angle between the liquid and the wall was varied; larger contact angles caused the bubble growth period and the diameter of the bubble when it left the wall to increase. The superheat at the wall was also varied; as the superheat was increased, the bubble's growth period decreased, and the bubble's diameter at the departure time (the time the bubble departs from the wall) increased.

Building on their previous model for a single bubble (1999), Son et al. (2002) developed a laminar axisymmetric numerical model of bubbles merging. In this model, a single nucleation site was used to generate an initial bubble which would leave the heater surface, followed by a second bubble which would then merge with the first bubble. The waiting period was varied as a parameter, and every bubble was initialized with same volume after this waiting period had elapsed. The computational domain did not extend

far into the fluid by the heater's surface. The fluid properties were kept constant. They performed an experiment which they used to validate their model results.

Mukherjee and Dhir (2004) modeled the lateral merging of two or three bubbles using a three-dimensional grid and the level set method. Their model built on the ones developed by Son et al. (1999), (2002) and therefore included the effect of the microlayer. Again, the bubbles were initially placed at the nucleation sites with an initial size and then allowed to grow using the model. The computational domain did not extend far into the fluid by the heater's surface. They ran an experiment to validate their model against.

Son and Dhir (2008) modeled nucleate boiling at high superheat levels using the level set method, with both two- and three-dimensional grids. Although nucleate boiling is a three-dimensional phenomenon, especially when the bubbles merge laterally, the computational time for 3D cases was prohibitive; therefore, most of their cases were run as 2D. The computational domain did not extend far into the fluid by the heater's surface. The fluid properties were kept constant, and the flow was assumed to be laminar. Small bubbles were placed at the nucleation sites and allowed to grow. The growth and mergers of the bubbles in the 3D simulation were qualitatively similar to the 2D results, but because a coarser grid was used for the 3D case, the model did not fully capture the macrolayer (the liquid which was trapped when the bubbles merged). In particular, the heat flux at the wall calculated by the 3D case differed from that calculated by the 2D case; the 2D case was considered more accurate.

Dhir et al. (2013) reviewed numerical models of pool boiling, providing details of some models, trends, and suggestions for future work. The diameter of a bubble at the departure time decreases linearly with the contact angle until the contact angle is 20° ; for more

wetting fluids, the bubble's departure diameter varies non-linearly with the contact angle. As the concentration of noncondensable gases increases, the bubble's diameter increases; according to Dhir, this is more important in microgravity than in 1g. Noncondensables did not have much effect on the rate of heat transfer from the wall, but they did cause thermocapillary convection, which affects the flow of the liquid around the bubble in microgravity. Microgravity also affects the buoyancy, which in turn affects the departure diameter of bubbles. The heat flux is affected as well; during an experiment in low gravity (0.01g), the heat flux is less than in 1g, while the percentage of the wall's energy that produces vapor increases compared to that in 1g. Among Dhir's recommendations for future work is to model nucleate boiling in 3D; these models have been limited due to the computing power and memory required.

Merte and Lee (1997) examined the Pool Boiling Experiment (PBE), which studied boiling in microgravity at low heat fluxes using a low boiling point refrigerant. The experiment was performed in space shuttles. They used heat fluxes which were up to half of the level needed to cause boiling in 1g, but because the natural convection in microgravity was not strong enough to mix the heated fluid with colder fluid, boiling did occur. The heat was provided by two heaters; the temperatures were recorded by thermistors, and the boiling was recorded by motion photography from two camera angles. The tank pressure was varied as a parameter between tests, in order to control the saturation temperature inside the tank, and therefore control the level of superheat created by the heater. During each test, the tank pressure was held constant. At the lowest levels of heat flux, the boiling appeared to be homogeneous, at medium levels of heat flux, the boiling appeared to be heterogeneous, and at high levels of heat flux, the boiling again appeared to

be homogeneous. These were determined by whether or not the nucleation took place at the same locations on the heaters on different experimental runs.

Tank Pressurization due to Boiling

Tank pressurization due to boiling does not seem to have been studied as much as heat transfer. Hasan and Balasubramaniam (2012) developed an analytical model of the boiling that occurred during the Tank Pressure Control Experiment: Thermal Phenomena (TPCE/TP), which was run in a space shuttle, under long duration microgravity conditions. In this experiment, a tank was partially filled with a refrigerant fluid with a low boiling point, and self-pressurization was induced by two heaters. The results were captured via a video camera along with a pressure transducer and thermistors; they showed pressure spikes due to boiling, and the bubbles generated were visible to the camera. The goal for the model was to predict the tank pressure and the volume of the ullage with respect to time. The vapor was assumed to be an ideal gas, and the liquid was assumed to be incompressible. The bubbles in their model nucleated when a predetermined superheat was reached at the wall as compared to the saturation temperature of the tank pressure. Convection heat transfer was neglected in favor of conduction heat transfer to the bubbles. Multiple bubbles were modeled by calculating the solution for a single bubble and then multiplying by a specified number of nucleating bubbles. As the bubbles grew, the shrinking and condensation of the ullage were also taken into account. The tank heaters were assumed to be turned off during bubble growth, which was not a good assumption for every experimental run, but worked for some. The model was able to predict the magnitude of the pressure spikes due to boiling well, but not the rate of the pressure rise.

CHAPTER III

THE TANK PRESSURE CONTROL EXPERIMENT: THERMAL PHENOMENA

The Tank Pressure Control Experiment (TPCE) was flown on Space Shuttle Mission STS-43 in August 1991 in order to study how liquid superheats, which can cause pressure spikes due to boiling, can be controlled with an axial jet (Bentz, 1993). The experiment consisted of a tank filled with liquid and vapor Freon, held inside a Get-Away Special container. Heaters inside the tank were used to create the superheats. During the experiment, the liquid superheats were followed by pressure spikes; this suggested that boiling occurred, but there was no video of this as only the first two minutes of the heating period were recorded by the camera (Hasan, Lin, Knoll, & Bentz, 1996), (Bentz, 1993). In order to videotape more of the results, the same experiment apparatus was reflown as the Tank Pressure Control Experiment: Thermal Phenomena (TPCE/TP) on the Space Shuttle Mission STS-52 (Hasan, Lin, Knoll, & Bentz, 1996). This time, the entire heating phase was recorded for the first 16 tests.

The experiment used a tank which was cylindrical in shape, with a hemispherical dome on the top and bottom, as shown in Figure 1. Although the tank length is given as 36.6 cm in Figure 1, the actual value is 35.6 cm (14.0 in) (Bentz, 5/15/2014). The tank was made

of two acrylic sheets which were formed into domes and bolted onto a stainless steel ring (Bentz, 1993), as shown in Figure 2; the dimensions of this ring are not provided. All of the components that protrude into the tank, including the thermistors, heaters, and jet nozzle, entered the tank through this steel ring. There were six thermistors which measured temperatures inside the tank, and one which measured the temperature of the liquid jet entering the tank via the nozzle, which was aligned with the central axis of the tank. The uncertainty of each of these thermistors was given as 0.1 °C (Hasan, Lin, Knoll, & Bentz, 1996). The temperature outside of the tank was not provided. The two heaters had the same area; heater B was parallel to the tank axis, and heater A was curved to fit near the wall at the top of the tank (Bentz, 1993), (Hasan, Lin, Knoll, & Bentz, 1996), as shown in Figure 3. The uncertainty of the heater power was given as 0.1W (Hasan, Lin, Knoll, & Bentz, 1996). A pressure transducer monitored the tank pressure during the experiment; its uncertainty was given as 0.35 kPa. Figure 3 shows all of the main components of the experiment. Figure 4 shows a photo of several components inside the tank.

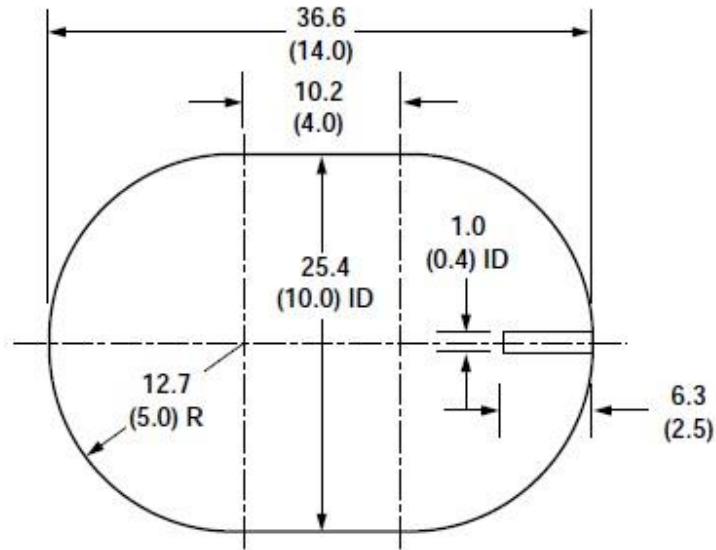


Figure 1: Tank Shape and Dimensions in cm (in) (Hasan, Lin, Knoll, & Bentz, 1996)

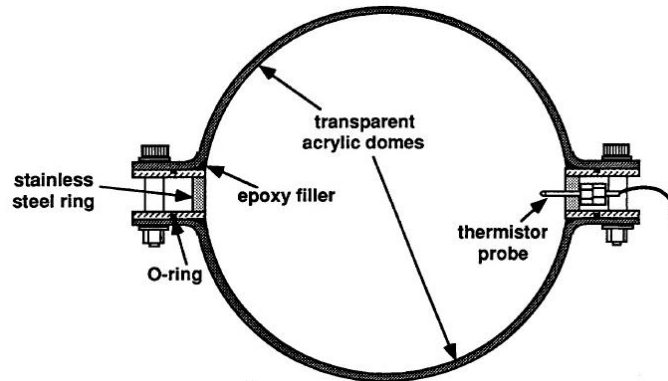


Figure 2: Schematic of the Tank Assembly (Bentz, 1993)

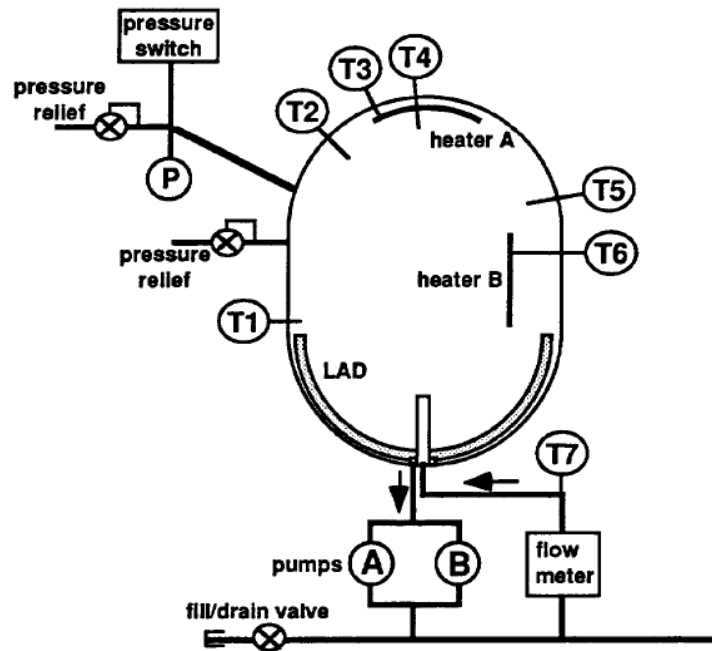


Figure 3: Schematic of the Main Components of the Experiment (Bentz, 1993)

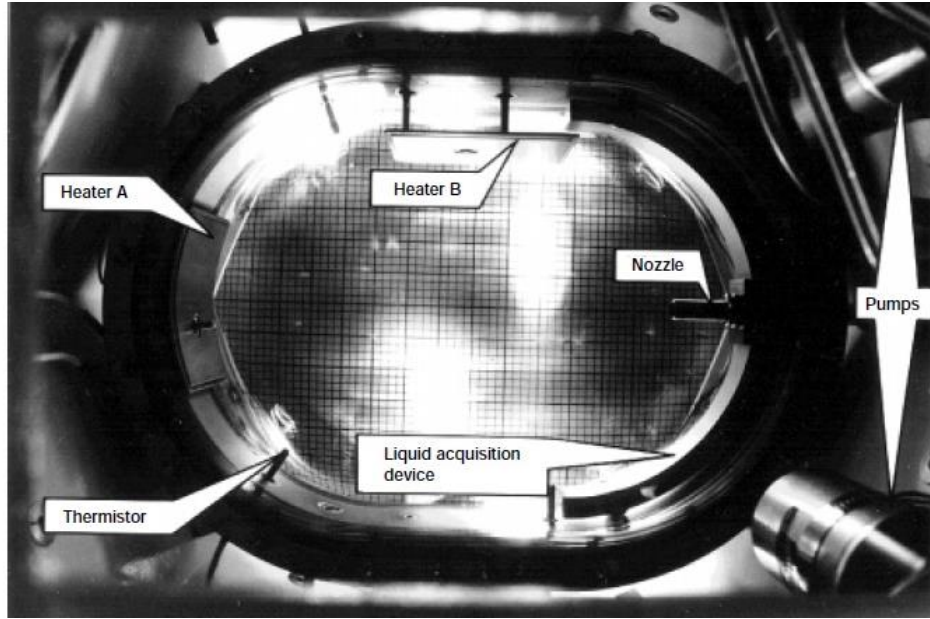


Figure 4: Photo of various components inside the tank (Hasan, Lin, Knoll, & Bentz, 1996)

The tank was filled to 83% by volume with liquid Freon 113 (Hasan, Lin, Knoll, & Bentz, 1996). In TPCE/TP, some non-condensable gas was included; the partial pressure was 1.0 kPa, and the mass fraction was between 0.5 and 2.0%. Since the heaters were immersed, they directly heated the fluid.

Heater A and Heater B had the same outer dimensions (Hasan, Lin, Knoll, & Bentz, 1996), (Bentz, 1993), as shown in Figure 5. Their thickness is given as 0.191 cm (Bentz, 1993). Heater B was kept straight, and was placed along the side of the tank in the cylindrical portion (Hasan, Lin, Knoll, & Bentz, 1996). It was held 0.025m from the tank wall by a standoff tube. Heater A was curved with a 0.121 m radius so that it could be placed near the hemispherical wall at the top of the tank, opposite the nozzle. It was held 0.005 m from the tank wall by a standoff tube. The surface temperature of heater A was measured by thermistor T3, while thermistor T6 measured the surface temperature of heater B, as shown in Figure 3. Both of the heaters were made of the same material, a heating element inside of silicon rubber, with 304L stainless steel plates on the outside. Since both

sides of the heaters were in contact with the liquid, their areas were given as 0.0155m^2 . Their masses were given as 0.214 kg , and their thermal capacitances were given as $0.10\text{kJ}/^\circ\text{C}$.

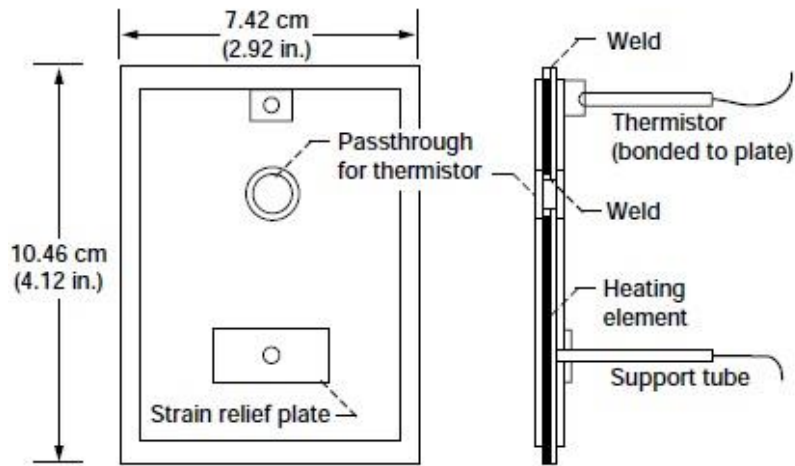


Figure 5: Schematic of Heater with Dimensions in cm (in) (Hasan, Lin, Knoll, & Bentz, 1996)

Since the TPCE/TP experiment was conducted on board a space shuttle, the attitude of the space shuttle affected the accelerations experienced by the experiment (Hasan, Lin, Knoll, & Bentz, 1996). These accelerations were measured along three axes by accelerometers, whose ranges were given as $\pm 0.01g$, with a resolution of $2.4 \times 10^{-6}g$, and an accuracy of $5 \times 10^{-4}g$ absolute or $1.2 \times 10^{-5}g$ relative. However, these accelerometers were intended to measure sudden, large accelerations rather than the typical accelerations the experiment experienced (Bentz, 1993). Therefore, the actual level of acceleration during most of the testing is unknown (Bentz, 1993) (Hasan, Lin, Knoll, & Bentz, 1996). However, during the first flight of the experiment, the average acceleration due to drag was estimated at around $7 \times 10^{-7} g$, which calculates to approximately $6.9 \times 10^{-6} \text{ m/s}^2$ (Bentz, 1993). Since the experiment was flown on Space Shuttles both times, it may be reasonable to assume the same acceleration levels for both flights.

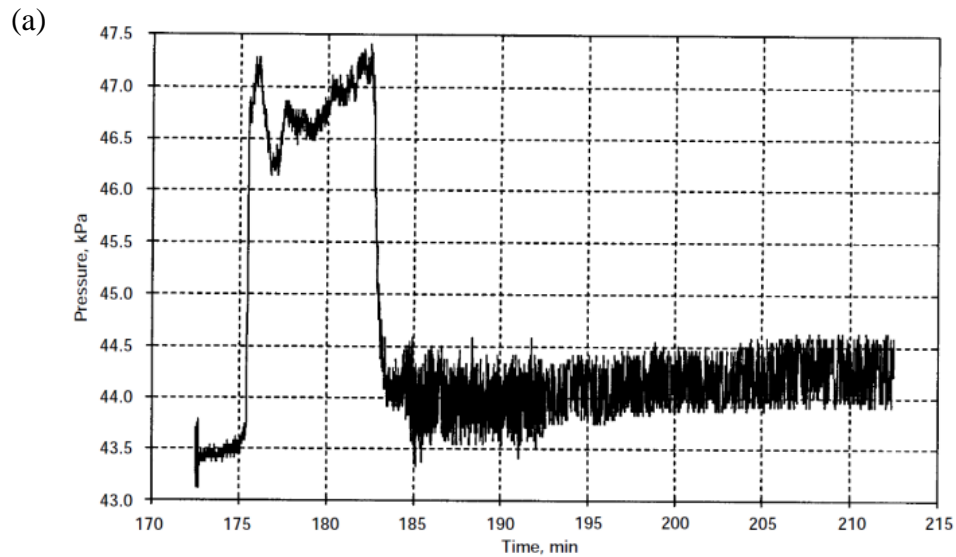
Some of the tests performed in the TPCE/TP experiment were jet mixing only; others used one or both of the tank heaters, which were used for various lengths of time (Hasan, Lin, Knoll, & Bentz, 1996). A summary of the different tests that were performed and the variables which were altered for each is shown in Table 1.

Table 1: Summary of the various tests performed during the TPCE/TP experiment

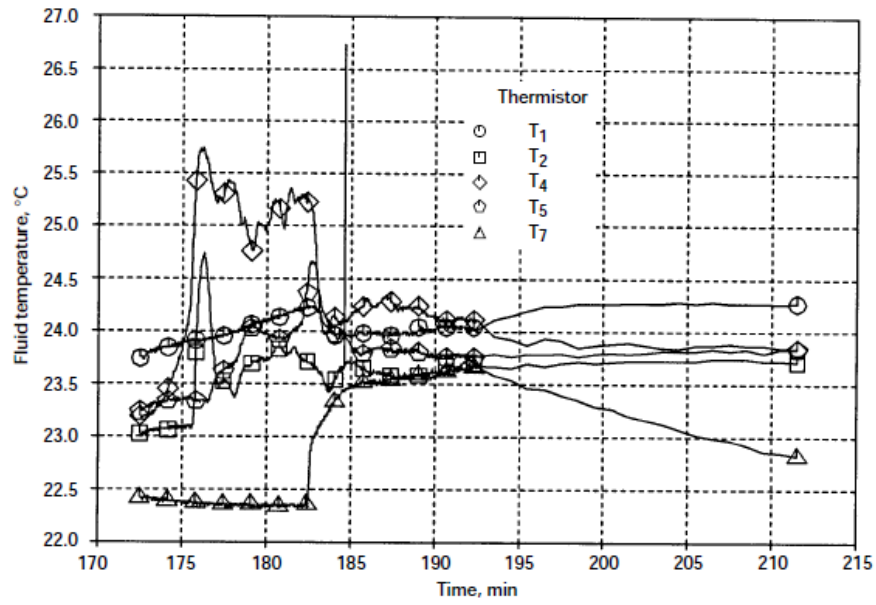
Run	Heater	Camera	Heating Duration	Heat Flux (kW/m ²)	Ullage Location At Start of Boiling	Pressure Spike	Boiling Type	Sleep Period	Orientation
1	Off	On	n/a	n/a	n/a	n/a	n/a	No	?
2	B	On	10.0 min	1.10	Touching heater	No (42.7-40.1)kPa	Nucleate	No	?
3	B	On	10.0 min	1.07	Touching heater	No (46.9-40.6)kPa	Nucleate	No	Tail-first
4	B	On	10.0 min	1.06	Touching heater	No (46.1-42.1)kPa	Nucleate	No	Tail-first
5	Off	On	n/a	n/a	n/a	n/a	n/a	No	Tail-first
6	A	On	10.0 min	1.07	Nearly touching	(46.9-44.1) kPa	Nucleate	Yes	Tail-first
7	A	On	10.0 min	1.04	Not touching	(58.2-46.7) kPa	Explosive	Yes	Tail-first
8	A	On	10.0 min	1.03	Not touching	(61.4-49.6) kPa	Explosive	Yes	Tail-first
9	Off	On	n/a	n/a	n/a	n/a	n/a	Yes	Tail-first
10	B	On	18.0 min	0.98	Touching heater	No (51.7-46.0)kPa	Nucleate	Yes	Tail-first
11	B	On	18.0 min	0.95		No (?)	Nucleate	Yes	Tail-first
12	A	On	18.0 min	0.98	Not touching	(67.4-54.8)kPa	Explosive	Yes	Tail-first
13	A	On	18.0 min	0.97	Far from heater	(70.0-50.7)kPa	Explosive	Yes	Tail-first
14	Off	On	n/a	n/a	n/a	n/a	n/a	Yes	Tail-first
15	A and B	On	18.0 min	0.23	n/a		None	Yes	Tail-first
16	A and B	On	18.0 min	0.23	n/a		None	Yes	Tail-first
17	A	Off	20.0 min	0.95	Uncertain	(72.7-56.9)kPa	Explosive	No	Tail-first
18	B	Off	20.0 min	0.89	Uncertain; possibly far from heater	Yes (73.8-56.8)kPa	Explosive	No	?
19	A and B	Off	40.0 min	0.23	Uncertain	Yes	Probably Explosive	No	?
20	B	Off	40.0 min	0.86	Uncertain	No (?)	Nucleate	No	?
21	A	Off	40.0 min	0.89	Uncertain; probably nearly touching	(70.6-68.5)kPa	Nucleate?	No	?

Test 6

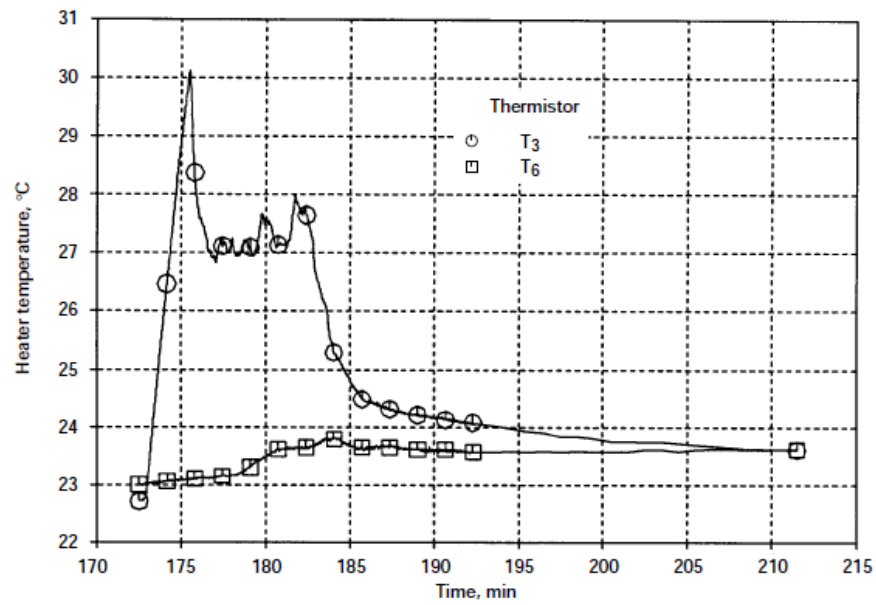
Test 6 from the TPCE/TP experiment, summarized in Table 1, was chosen to validate the model developed in this work. The space shuttle attitude was constant and known during this test, and there were no sudden accelerations during the heating period (Hasan, Lin, Knoll, & Bentz, 1996). Heater A was on, and heater B was off, making the tank fairly axisymmetric. The tank underwent nucleate boiling, rather than the explosive boiling experienced in many other tests. The pressure, temperature, and flow rate data were plotted against time in Tank Pressurization and Pressure Control: Thermal Phenomena in Microgravity (Hasan, Lin, Knoll, & Bentz, 1996). The program Engauge Digitizer was used in this work to digitize the data so that detailed comparisons between the model predictions and the experimental results could be made. The original graphs are shown in Figure 6.



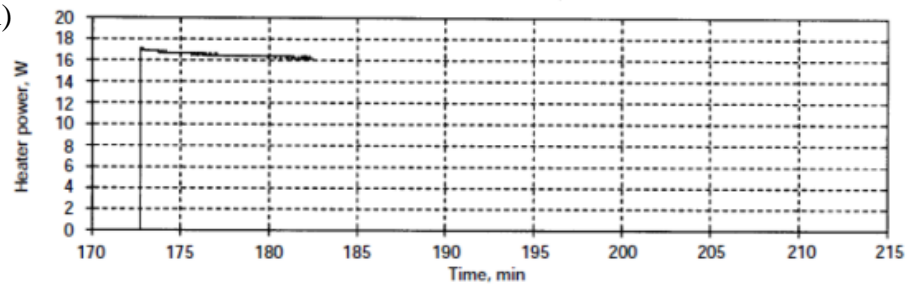
(b)



(c)



(d)



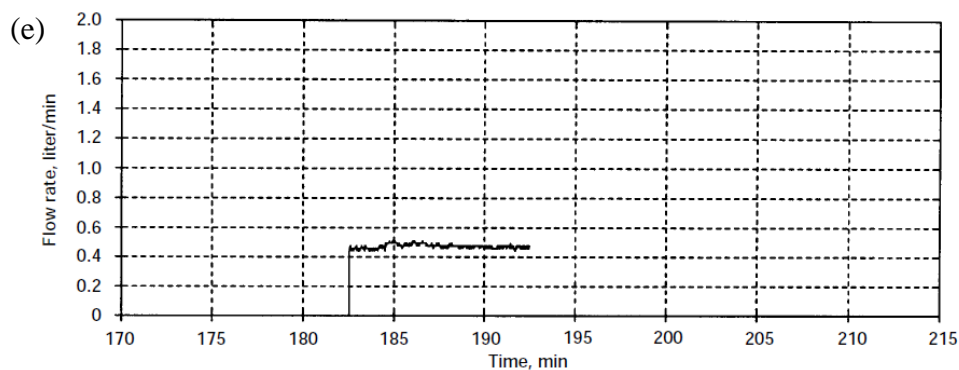


Figure 6: Data from TPCE/TP Test 6 (Hasan, Lin, Knoll, & Bentz, 1996): (a) Pressure, (b) Fluid temperatures, (c) Heater temperatures, (d) Power applied to heater A, (e) Flow rate

In order to make comparisons with the cases easier, the digitized graphs were altered from what is shown in Figure 6. The time was converted to seconds, and the temperatures were converted from Celsius to Kelvin. The time at which the heater was turned on was subtracted from all of the other data in order to set the initial time of the test to zero. Plots of the digitized data are shown in Figure 7 through Figure 11. The points in the graphs show the locations at which the data was digitized; error bars based on the uncertainties reported for the instruments (Hasan, Lin, Knoll, & Bentz, 1996) are shown as well.

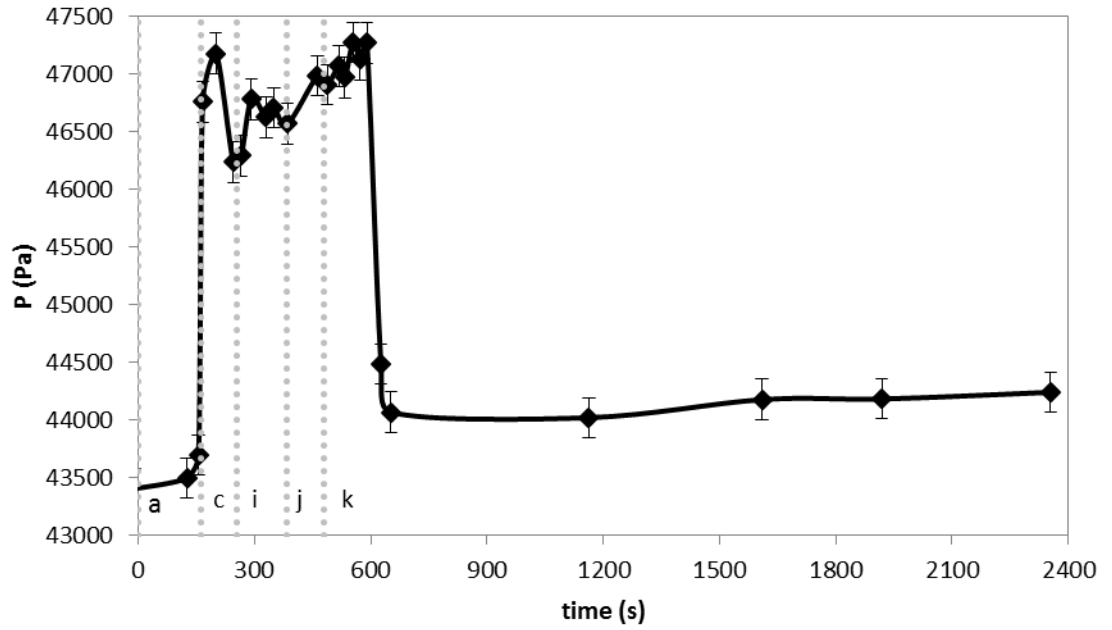


Figure 7: Pressure during test 6 of the TPCE/TP experiment (digitized) (dashed vertical lines are to show the times at which images were obtained from the movie of the experiment)

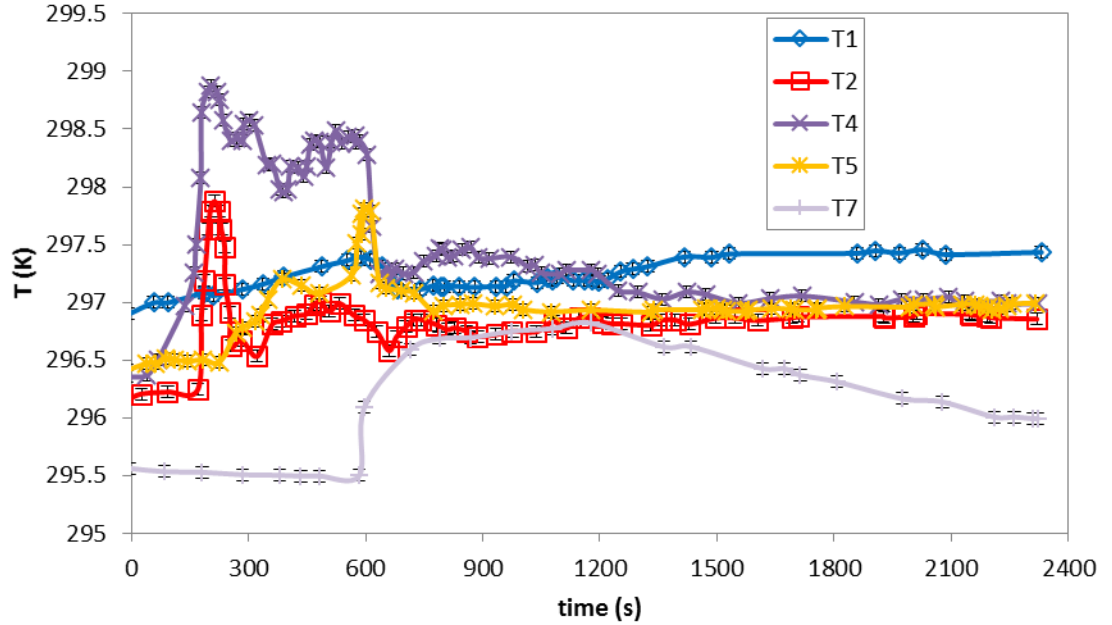


Figure 8: Fluid temperatures during test 6 of the TPCE/TP experiment (digitized)

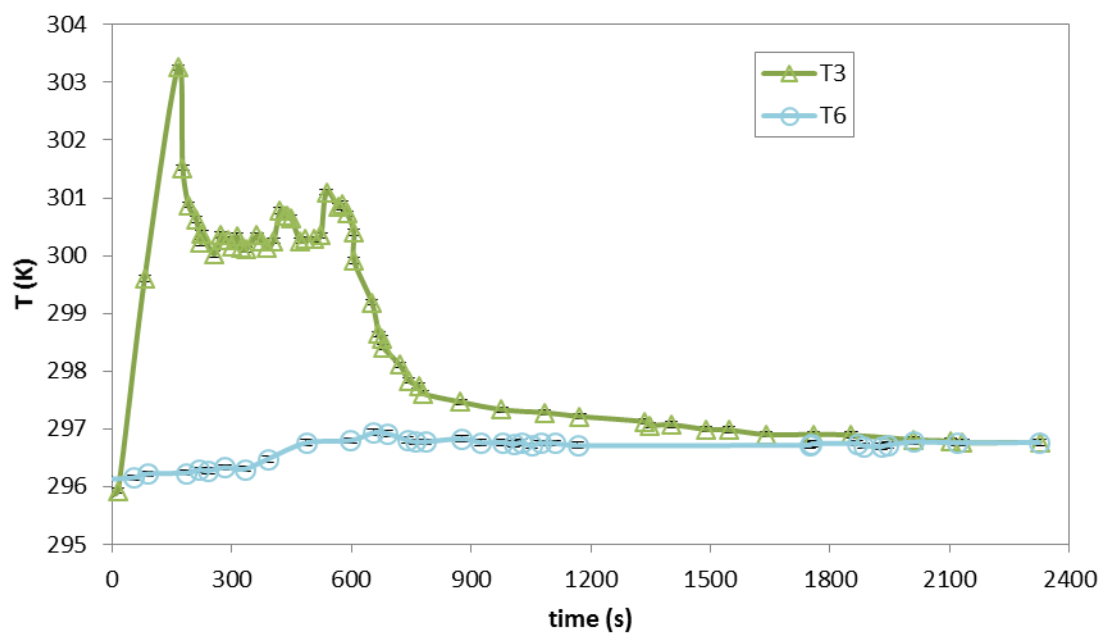


Figure 9: Heater temperatures during test 6 of the TPCE/TP experiment (digitized)

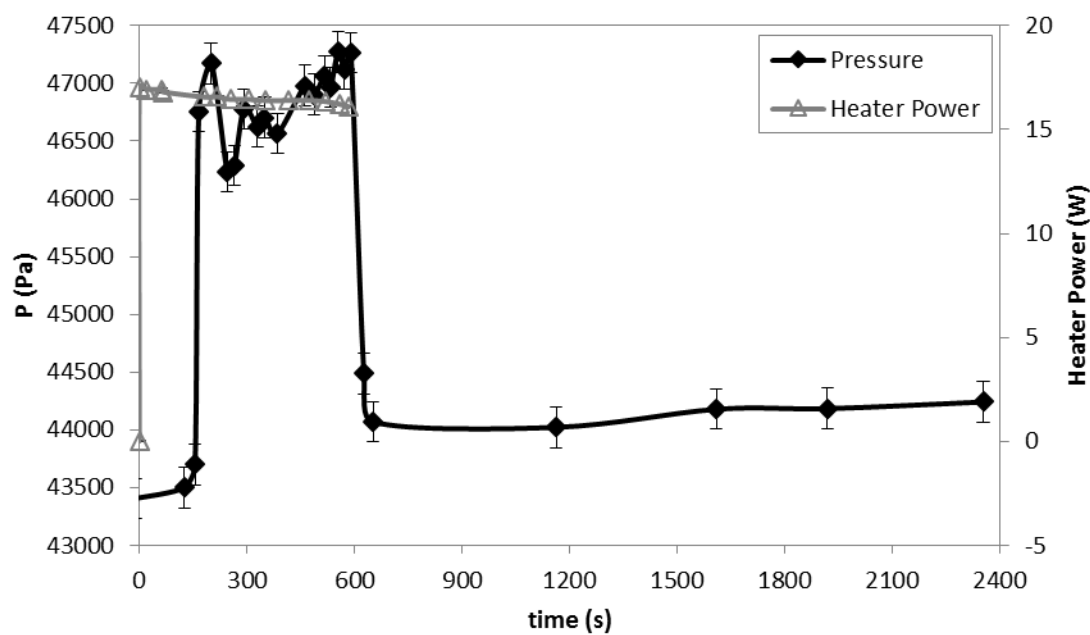


Figure 10: Pressure and Heater Power during test 6 of the TPCE/TP experiment (digitized)

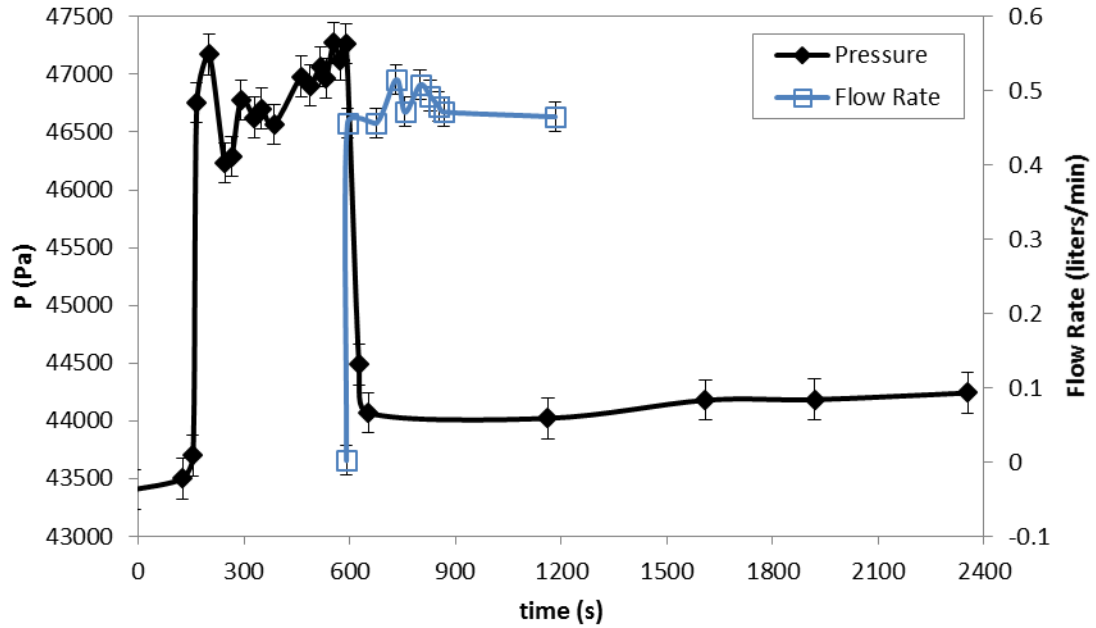
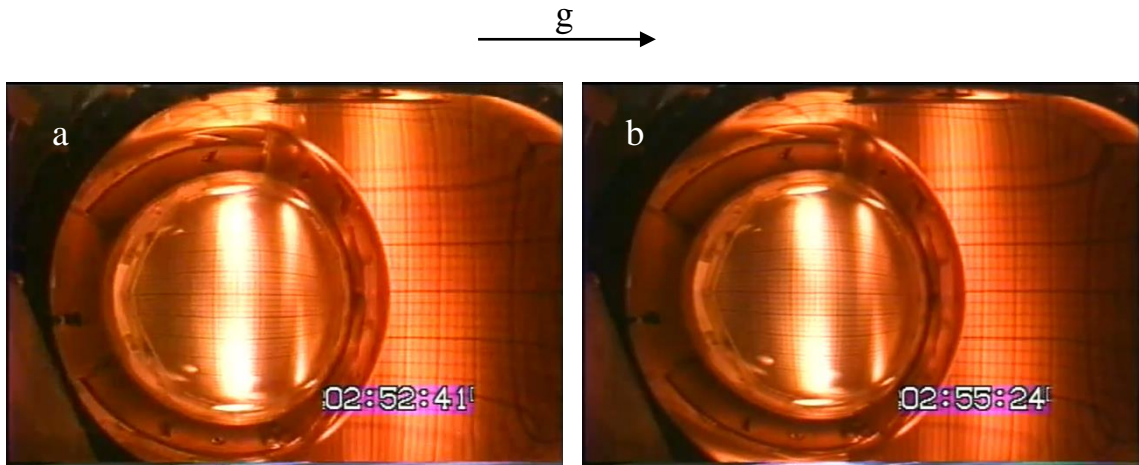


Figure 11: Pressure and Flow Rate during test 6 of the TPCE/TP experiment (digitized)

During test 6 of the TPCE/TP experiment, video data was also taken of the tank (Hasan, Lin, Knoll, & Bentz, 1996). Images from this video (obtained from YouTube (NASA STI Program, 2012)) are shown in Figure 12. The vertical dashed lines in Figure 7 indicate the times at which certain of these images were taken from the video (again, the time at which the heater was turned on was subtracted from each of these times). Additionally, the heater power and jet flow rate were plotted along with the pressure curve from test 6 of the TPCE/TP experiment in Figure 10 and Figure 11, to show the effects of turning the heater and pump on and off.

From Figure 8 and Figure 9, it can be seen that when the heater was turned on, the temperature of the fluid began to stratify, with hot liquid around the heater. As the heat reached the interface between the liquid and vapor, evaporation occurred, which caused the pressure in the tank to increase, as shown in Figure 10. After some time, the hot liquid around the heater began to boil, as shown in photo (c) of Figure 12. Between images (c)

and (i) in Figure 12, bubbles continued to form and join with the ullage. Whenever a bubble joined the ullage, the shape of the ullage was deformed. This process continued for some time, as shown by the rest of the images in Figure 12; sometimes a small drop of liquid seems to have moved through the ullage when a bubble joins the ullage, as shown in photo (j). It is difficult to determine whether the ullage grows in volume during this process; although evaporation was occurring at the heater, condensation was likely to have occurred at the interface of the ullage, since the temperature of the liquid surrounding the ullage was likely to be lower than the saturation temperature of the pressure in the tank. A comparison between Figure 10 and Figure 11 indicates that the jet was turned on at about the same time the heater was turned off, mixing the stratified fluid. At this point, the pressure began to drop. This was the pressure control period of the experiment, which was not simulated in this work.





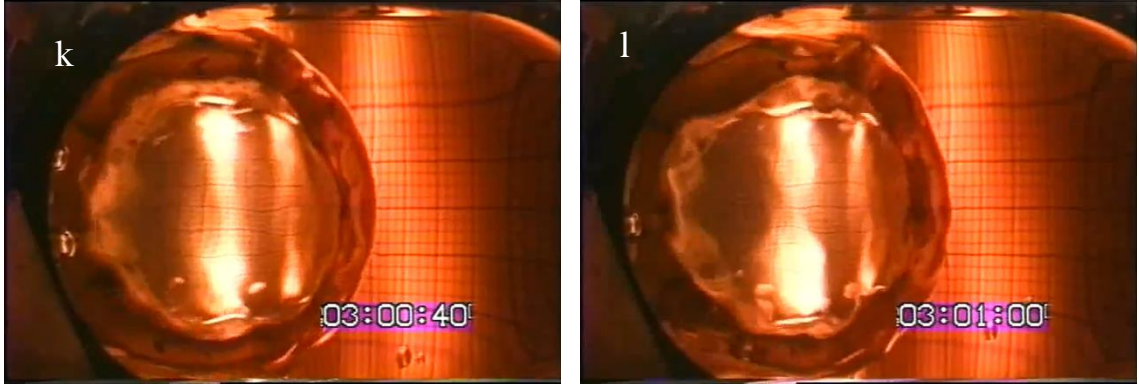


Figure 12: Images of test 6 taken during the heating phase of the TPCE/TP experiment (NASA STI Program, 2012)

The superheat temperature above the saturation temperature in the tank which is necessary to initiate boiling can be calculated from the fluid properties and from the sizes of the cavities on the heated surface, as shown in Equation 1 (Muduwar, 2014). However, the cavity sizes in the surfaces of the heaters were not given by either Bentz (1993) or by Hasan et al. (1996). Using typical surface finishes obtained by a variety of machining and polishing processes (Engineer's Handbook, 2006), a range of potential superheat temperatures required to initiate boiling might be estimated, as shown in Figure 13.

$$T_{sh} - T_{sat} = \frac{T_{sat} \nu_{fg}}{h_{fg}} \frac{2\sigma}{r} \quad \text{Equation 1}$$

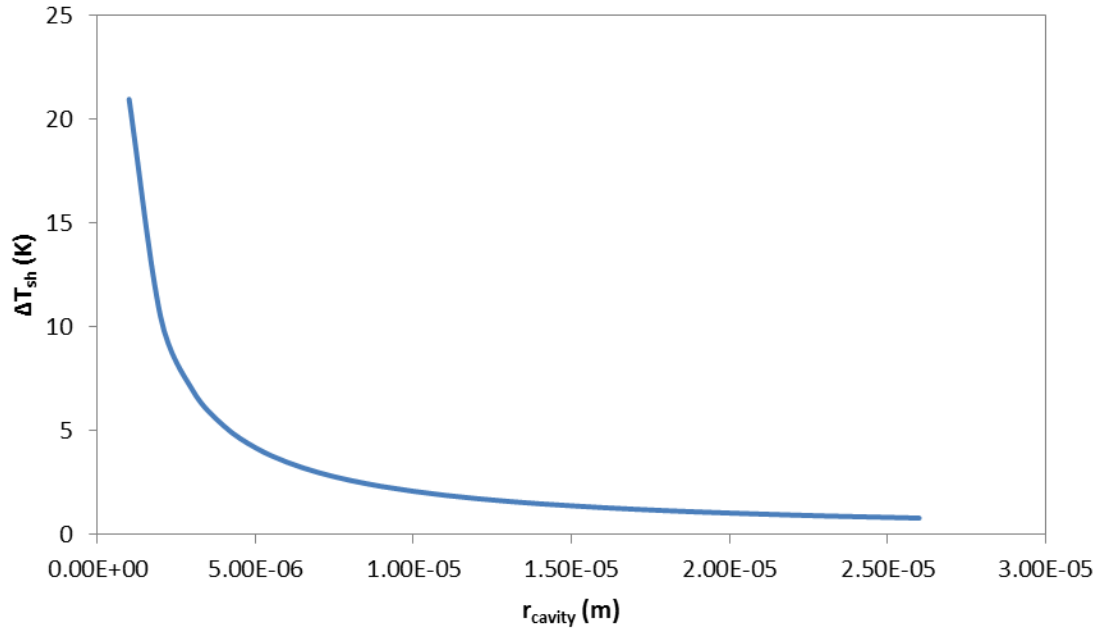


Figure 13: Range of superheat temperatures required to initiate boiling in Freon 113 for various cavity sizes

However, Figure 9 and the images in Figure 12 show that the heater temperature rose quite a lot before falling at about the time when boiling began. This kind of hysteresis is common for highly-wetting fluids such as Freon, as the liquid tends to fill the cavities in the heated surface (Muduwar, 2014). If this occurs, a larger superheat temperature is needed for a bubble embryo to form in a cavity in the heated surface. This means that, for highly wetting fluids, the onset of boiling is unpredictable. Once boiling has started, however, the bubble can activate other cavities. At this point, boiling will continue at the lower superheat temperature determined by the cavity size.

The superheat at which the boiling continued in the experiment can be estimated using the pressure shown in Figure 7 and the heater temperature shown in Figure 9. The pressure during the boiling period (between about 300 and 600s) was between about 46000 and 47000Pa. However, there was a small amount of noncondensable gas inside the tank; the

mass fraction of this gas was estimated by Hasan et al. (1996) as varying between about 0.5% and 2.0%. The composition of this gas does not appear to be specified.

In the original flight, the noncondensable gas was meant to be mostly helium (Bentz, 1993). However, when the composition of the noncondensable gas was measured after the experiment, it was found to be a mixture consisting of nitrogen, water vapor, helium, oxygen, carbon dioxide, and argon, in descending order of prevalence. This suggested that air replaced much of the helium in the tank. It seems reasonable to assume that air might have leaked into the tank in the reflight, as well; therefore, the composition of the noncondensable gas was assumed to be air for the purpose of calculating the superheat temperature. The partial pressure of the vapor can be calculated from the total pressure using the mole fraction of vapor, as shown in Equation 2 (Cengel & Boles, 2006):

$$P_v = P_{total}x_v \quad \text{Equation 2}$$

Where the mole fraction of vapor can be calculated from the mole fraction of the noncondensable gas as:

$$x_v = 1 - x_g \quad \text{Equation 3}$$

Taking the maximum value, the partial pressure of the Freon 113 vapor would have been about 45800 to 46800Pa. Using the Clausius Clapeyron equation, the saturation temperature of the pressure can be determined (Cengel & Boles, 2006). In order to bracket the actual temperature, the saturation temperature was calculated for a mass fraction of noncondensable gas equal to 0% as well as 2.0%; these saturation temperatures are shown in Table 2. Estimating the maximum temperature of the liquid as equal to the heater temperature (which is shown in Figure 9) gives a range of about 300 to 301K during the

boiling period (after the pressure spike). Subtracting the saturation temperature from the maximum liquid temperature gives the amount of superheat at which boiling occurred as between about 0.5 to 2.2K.

Table 2: Estimate of the tank's saturation temperature during boiling

No Noncondensables		with Noncondensables	
P (Pa)	Tsat (K)	P (Pa)	Tsat (K)
46000	298.9	45855.33	298.8
47000	299.5	46852.19	299.4

In order to determine whether the fluid flow in the tank was laminar or turbulent during test 6 of the TPCE/TP experiment, the Grashof number for free convection was calculated using two methods: a formulation for vertical and inclined surfaces with a constant heat flux, and for a surface with a temperature difference from the surrounding fluid. Since the actual acceleration due to gravity during the experiment is unknown (Hasan, Lin, Knoll, & Bentz, 1996), (Bentz, 1993), the Grashof number was calculated at various accelerations due to gravity.

The Grashof number times the Prandtl number was calculated using a formulation from Holman (2002) for vertical or inclined surfaces with a constant heat flux using two different characteristic dimensions. Column 2 of Table 3 shows $Gr_x * Pr$ for vertical and inclined surfaces using the area of the heater divided by the perimeter of the heater as the characteristic dimension. Column 3 shows $Gr_x * Pr$ for vertical and inclined surfaces using the diameter of the tank as the characteristic dimension. According to Holman (2002), the range at which boundary-layer transition begins is $3*10^{12} < Gr_x * Pr < 4*10^{13}$.

The Grashof number was also calculated using a formulation from Cengel and Ghajar (2007), using the difference between the averaged initial temperature measured in the

liquid and the maximum heater temperature achieved during the experiment. Column 4 of Table 3 shows the Grashof number using the area of the heater divided by the perimeter of the heater as the characteristic dimension. Column 5 shows the Grashof number using the diameter of the tank as the characteristic dimension. According to Cengel and Ghajar (2007), the critical Grashof number for a vertical plate is about 10^9 .

Since all of the Grashof numbers calculated in Table 3 are smaller than the critical Grashof numbers given by Holman (2002) and Cengel and Ghajar (2007), the flow during test 6 of the TPCE/TP experiment was assumed to be laminar.

Table 3: $Gr_x \cdot Pr$ and Gr during test 6 of the TPCE/TP experiment

Acceleration due to gravity (m/s^2)	Column 2 $Gr_x \cdot Pr$	Column 3 $Gr_x \cdot Pr$	Column 4 Gr_L	Column 5 Gr_L
10^{-3}	2.76E+05	5.17E+09	6.52E+02	1.05E+06
10^{-4}	2.76E+04	5.17E+08	6.52E+01	1.05E+05
10^{-5}	2.76E+03	5.17E+07	6.52E+00	1.05E+04
10^{-6}	2.76E+02	5.17E+06	6.52E-01	1.05E+03

CHAPTER IV

MATHEMATICAL MODEL

A 2D axisymmetric model was used for both the self-pressurization and boiling simulations, as shown in Figure 14. The tank was partially filled with liquid Freon 113.

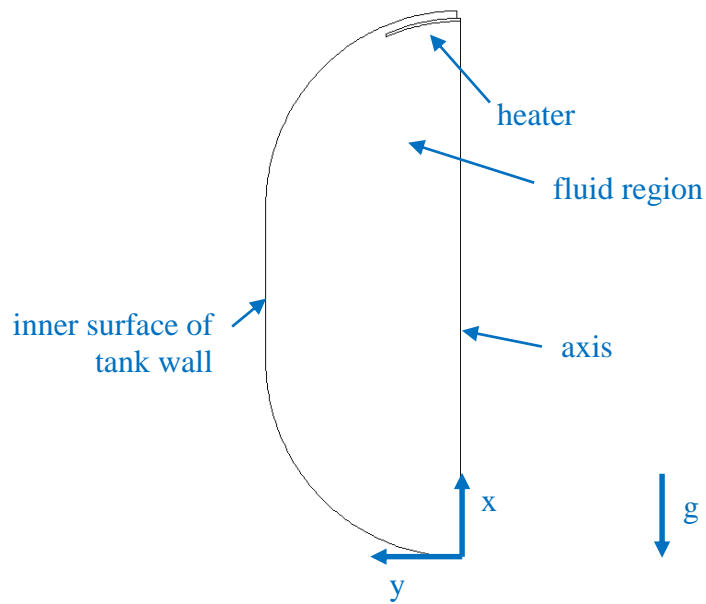


Figure 14: Schematic of Computational Domain

The continuity, momentum, and energy equations (ANSYS, 2013a) were solved for the fluid:

$$\frac{\partial \rho}{\partial t} + \nabla \cdot (\rho \vec{v}) = 0$$

Equation 4

$$\frac{\partial}{\partial t}(\rho \vec{v}) + \nabla \cdot (\rho \vec{v} \vec{v}) = -\nabla P + \nabla \cdot [\mu(\nabla \vec{v} + \nabla \vec{v}^T)] + \rho \vec{g} + \vec{F}_{vol} \quad \text{Equation 5}$$

$$\frac{\partial}{\partial t}(\rho E) + \nabla \cdot (\vec{v}(\rho E + P)) = \nabla \cdot (k_{eff} \nabla T) + S_h \quad \text{Equation 6}$$

The liquid was modeled as incompressible; however, its density was allowed to vary with temperature in the body force term of the momentum equation using the Boussinesq model (ANSYS, 2013b):

$$(\rho - \rho_0)g \approx -\rho_0 \beta (T - T_0)g \quad \text{Equation 7}$$

where ρ_0 is the constant density of the fluid, and T_0 is the operating temperature.

The Volume Fraction of Fluid (VOF) model in Fluent v 15 was used to track the location of the liquid-vapor interface, which evolves with time. The VOF model tracks the interface by solving a continuity equation for the volume fraction of each phase; the equation takes the following form for the q^{th} phase (ANSYS, 2013a):

$$\frac{1}{\rho_q} \left[\frac{\partial}{\partial t} (\alpha_q \rho_q) + \nabla \cdot (\alpha_q \rho_q \vec{v}_q) \right] = S_{\alpha_q} \quad \text{Equation 8}$$

In this case the volume fraction for the primary phase is found from (ANSYS, 2013a):

$$\sum_{q=1}^n \alpha_q = 1 \quad \text{Equation 9}$$

The implicit and explicit VOF time discretization schemes were compared. For the implicit scheme, the face fluxes for all cells are calculated from the current time step using (ANSYS, 2013a):

$$\frac{\alpha_q^{n+1} \rho_q^{n+1} - \alpha_q^n \rho_q^n}{\Delta t} V + \sum_f (\rho_q^{n+1} U_f^{n+1} \alpha_{q,f}^{n+1}) = \left[S_{\alpha_q} + \sum_{p=1}^n (\dot{m}_{pq} - \dot{m}_{qp}) \right] V \quad \text{Equation 10}$$

Where $n + 1$ is the index of the current time step, n is the index of the previous time step, $\alpha_{q,f}$ is the face value of the q^{th} volume fraction, V is the cell volume, and U_f is the volume flux through the face based on the normal velocity.

For the explicit scheme, the face fluxes are calculated from the previous time step (ANSYS, 2013a):

$$\frac{\alpha_q^{n+1} \rho_q^{n+1} - \alpha_q^n \rho_q^n}{\Delta t} V + \sum_f (\rho_q U_f^n \alpha_{q,f}^n) = \left[\sum_{p=1}^n (\dot{m}_{pq} - \dot{m}_{qp}) + S_{\alpha_q} \right] V \quad \text{Equation 11}$$

The surface tension forces were modeled using the Continuum Surface Force model, and were applied using the source term (ANSYS, 2013a):

$$F_{vol} = \sum_{pairs\ i,j, i < j} \sigma_{ij} \frac{\alpha_i \rho_i \kappa_j \nabla \alpha_j + \alpha_j \rho_j \kappa_i \nabla \alpha_i}{\frac{1}{2}(\rho_i + \rho_j)} \quad \text{Equation 12}$$

where κ is the curvature of the surface, calculated from the unit normal, \hat{n} , at the interface (ANSYS, 2013a):

$$\kappa = \nabla \cdot \hat{n} \quad \text{Equation 13}$$

The fluid properties were calculated as volume-fraction averages of the property in question; for example, the density was calculated as (ANSYS, 2013a):

$$\rho = \sum_{q=1}^n \alpha_q \rho_q \quad \text{Equation 14}$$

The energy and the temperature were calculated as mass-averaged variables (ANSYS, 2013a):

$$E = \frac{\sum_{q=1}^n \alpha_q \rho_q E_q}{\sum_{q=1}^n \alpha_q \rho_q} \quad \text{Equation 15}$$

The mass source term S_{a_q} in Equation 8 is a volumetric mass source, with units of $\text{kg}/(\text{m}^3 \cdot \text{s})$. The mass transfer at the interface, due to both evaporation and condensation, was calculated using the Schrage equation (Schrage, 1953), (Marek & Straub, 2001), (Sharma, 2006), while the mass transfer in the bulk liquid due to boiling was calculated using either the Schrage equation or the Lee model (ANSYS, 2013a). In both cases, the mass transfer due to boiling was limited to regions in the bulk liquid where the superheat temperature was greater than a set threshold:

$$T_{sh} - T_{sat} > threshold \quad \text{Equation 16}$$

In order to make sure that the mass transfer that occurs in a given cell in each time step does not exceed the mass in that cell, the volumetric mass source term must be limited.

This was done for some cases by limiting the source as described by Equation 17:

$$S_{a_q} \leq \frac{\alpha_l \rho_l}{time\ step\ size} \text{ (or)} \quad \text{Equation 17}$$

$$S_{a_q} \leq \frac{\alpha_v \rho_v}{time\ step\ size}$$

In order to aid the convergence of the cases during boiling, an under-relaxation factor was used for the mass transfer:

$$S_{a_q} = (1 - UR)S_{a_q,n} + UR * S_{a_q,n+1} \quad \text{Equation 18}$$

Schrage Equation

The mass transfer at the interface was modeled as a source term in Equation 8 (Kartuzova & Kassemi, 2011):

$$S_{a_q} = \vec{m} \cdot \vec{A}_l \quad \text{Equation 19}$$

where \vec{A}_l is the interfacial area density vector (Kartuzova & Kassemi, 2011):

$$\vec{A}_l = |\nabla\alpha| \quad \text{Equation 20}$$

For some cases, the mass transfer due to boiling was also modeled as a source term in Equation 8:

$$S_{a_q} = \vec{m} \cdot \frac{1}{V_{cell}^{1/3}} \quad \text{Equation 21}$$

where V_{cell} is the volume of the cell.

For both Equation 19 and Equation 21, \vec{m} is a mass flux vector. The mass flux which was applied to a cell could be calculated using the Schrage equation (Schrage, 1953):

$$\dot{m} = \sigma \sqrt{\frac{M}{2\pi R_u T_{sat}}} (P_{sat} - P_v) \quad \text{Equation 22}$$

where σ is the accommodation coefficient, P_{sat} is the saturation pressure based on the cell temperature, calculated using the Clausius-Clapeyron relation, and P_v is the vapor pressure. According to Schrage, Equation 22 can only be applied when the interfacial temperature for the vapor may be almost equal to the interfacial temperature for the liquid. This condition is required because of the assumptions made in the derivation of Equation 22. Schrage stated that this condition might occur when “the energy transfer necessary for condensation or evaporation occurs through the condensed (or liquid) phase rather than the gas (or vapor) phase.”

The Hertz-Knudsen-Schrage equation can be used to describe both evaporation and condensation along an interface (Marek & Straub, 2001), (Sharma, 2006):

$$\dot{m} = \frac{2}{2-\sigma_c} \left(\frac{M}{2\pi R_u} \right)^{\frac{1}{2}} \left(\sigma_c \frac{P_{sat}}{\sqrt{T_l}} - \sigma_e \frac{P_v}{\sqrt{T_v}} \right) \quad \text{Equation 23}$$

where σ_c is the condensation coefficient, and σ_e is the evaporation coefficient. According to Cipolla Jr. et al. (1974), condensation can be thought of as vapor molecules hitting the interface. Some of these molecules may reflect back into the vapor, but some will enter the liquid as a condensate. The fraction of molecules which condense are represented by the condensation coefficient. Similarly, the evaporation coefficient represents a limit on the evaporation rate. Under equilibrium conditions, when the mass transfer due to condensation matches the mass transfer due to evaporation, the evaporation and condensation coefficients are equal to each other. Using equal values for both also works under near-equilibrium conditions. If the condensation and evaporation coefficients are assumed to be equal to each other, Equation 23 becomes (Marek & Straub, 2001), (Sharma, 2006):

$$\dot{m} = \frac{2\sigma}{2-\sigma} \left(\frac{M}{2\pi R_u} \right)^{\frac{1}{2}} \left(\frac{P_{sat}}{\sqrt{T_l}} - \frac{P_v}{\sqrt{T_v}} \right) \quad \text{Equation 24}$$

If $T_l = T_v = T_{cell}$, this becomes:

$$|\vec{\dot{m}}| = \frac{2\sigma}{2-\sigma} \sqrt{\frac{M}{2\pi R_u T_{sat}}} (P_{sat} - P_v) \quad \text{Equation 25}$$

According to Barrett and Clement (1992), who studied evaporation and condensation coefficients for water and liquid metals, evaporation and condensation are independent processes, except in high-density gases. The values of the accommodation coefficients depend in part on the shape of the interface; for aerosols, they can be larger than 0.2, while for flat interfaces, they can be less than 0.05. Noncondensables also have an effect on

condensation, but not on evaporation; mass fractions of air of 0.5% can reduce the rate of mass transfer due to condensation by 50%. Marek and Straub (2001) stated that the accommodation coefficients are higher for “dynamically renewing” surfaces than for stagnant surfaces. They added that their study of water suggests that the evaporation and condensation coefficients may not be constant properties, but instead may vary with temperature and pressure for a fluid. The evaporation coefficient may also be affected by impurities at the surface. According to Young (1991), the accommodation coefficient can be used to enable a model to match the experiment.

Lee Model

For some cases, the mass transfer due to boiling was calculated using the Lee model, provided on pages 591-593 of the Fluent version 15 Theory Guide (ANSYS, 2013a). Although Fluent has a built-in Lee model for calculating the mass transfer, this work does not use that built-in model. Instead, the equations provided in the Theory Guide were entered into a UDF. The mass transfer due to boiling was limited to cells that satisfied the superheat temperature condition given in Equation 16. The mass transfer at the interface was calculated using the Schrage equation.

In order to calculate the mass transfer, the Lee model uses the difference between the temperature in a cell and the saturation temperature of the vapor pressure. Equation 26 can be used to calculate evaporation, while Equation 27 can be used to calculate condensation:

$$S_{a_q} = coeff * \alpha_l \rho_l \frac{T_l - T_{sat}}{T_{sat}} \quad \text{Equation 26}$$

$$S_{a_q} = coeff * \alpha_v \rho_v \frac{T_{sat} - T_v}{T_{sat}} \quad \text{Equation 27}$$

A theoretical calculation for the value of *coeff* was provided based on the accommodation coefficient from the Hertz-Knudsen equation for mass transfer at a flat interface. The Fluent Theory Guide (ANSYS, 2013a) states that the value for evaporation may not be the same as the value for condensation, and that the range of *coeff* is large; it could be 0.1 or it could have an order of magnitude of 10^3 . The value of *coeff* can be changed to enable the model to match experimental data.

CHAPTER V

NUMERICAL IMPLEMENTATION

The goal of this work was to develop and validate a CFD model which could predict the pressure rise in a closed tank due to boiling. To this end, it was decided to model the tank as axisymmetric, since the computational efficiency of axisymmetric models would allow many parameters to be studied. Although boiling is a 3D phenomenon, it has been modeled using axisymmetric models with acceptable success (Son, Dhir, & Ramanujapu, 1999), (Son, Ramanujapu, & Dhir, 2002), (Son & Dhir, 2008). And the macrolayer could actually be resolved better in an axisymmetric case than in a 3D case, since the entire tank had to be meshed.

The TPCE/TP experiment was chosen to validate the model. Unfortunately, several important details needed for model validation were not measured and/or reported in the experiment. The temperature outside the tank was not measured (Bentz, 1993); this important boundary condition could not therefore be included in the model. Additionally, the dimensions of the steel ring, which would have acted as a heat sink, are not provided. The acceleration due to gravity was estimated to be around $7 \times 10^{-7}g$ for the first flight of the experiment (Bentz, 1993), but the actual value for either flight is unknown. A trace

amount of dye (less than 0.5ppm) was added to the fluid for visualization purposes during the first flight of the experiment (Bentz, 1993); whether this dye was included in the second flight, and the effect of the dye on the fluid properties, are unknown. A small amount of noncondensable gases were present during the experiment. The amount of these gases was estimated as varying between about 0.5% and 2.0% (Hasan, Lin, Knoll, & Bentz, 1996), but their composition was not reported. The locations of the thermistors were not provided in great enough detail (Bentz, 1993) to locate them exactly in the model. And, although it was shown in the movie recorded from the experiment (NASA STI Program, 2012), the location of the ullage at the beginning of the test was somewhat difficult to determine. Because of these unknown boundary and initial conditions, it was only possible to compare the predictions made by the model to the general trends of the experiment.

Tank Dimensions and Properties

The tank used for the TPCE/TP experiment does not lend itself to an axisymmetric model, as shown in Figure 2 and Figure 3, so some simplifications of the experiment were required. In the experiment, the tank heaters were both rectangular, as shown in Figure 5. As shown in Figure 3, heater B was placed along the side of the tank, while heater A was at the end opposite the nozzle. In order to create an axisymmetric model, heater B was left out, and heater A was altered from a rectangular heater into a circular one. The surface area of the heater, given as 0.0155m^2 , and radius of curvature, given as 0.121m , were kept as close as possible to the actual values. For the model, the surface area of the top and bottom of the heater was 0.0153m^2 ; if the side of the heater is included, the surface area was 0.0159m^2 .

The mass of the heater was given as 0.214 kg (Hasan, Lin, Knoll, & Bentz, 1996); this was divided by the volume of the CFD model of the heater, to get the density of the heater. The thermal capacitance of the heater was given as 0.10kJ/°C (Hasan, Lin, Knoll, & Bentz, 1996). The thermal conductivity was assumed to be equal to that of the steel that encased the heating element, 16.2 W/(m*K) at 100°C (AK Steel Corporation, 2007). The heat flux was given for each test (Hasan, Lin, Knoll, & Bentz, 1996); this heat flux was multiplied by the heater area to get a heater power. This heater power was then divided by the volume of the heater which was used in the model to obtain a volumetric heat flux. A curve-fit of the temperature of the heater, measured by thermistor T3 and shown in Figure 9, was also created with respect to time. This curve fit is shown in Appendix B. In the model, either the heater temperature was applied as a boundary condition, or the heater power was applied as a volumetric source term. The tank wall, nozzle, and liquid acquisition device (LAD) were neglected in the model.

The tank as modeled is shown in Figure 14. The fluid region was filled with both liquid and vapor; the initial amount of liquid was set as 83% of the tank's inner volume, while the location of the ullage was approximated from the photos shown in Figure 12. The fluid properties are shown in Appendix A; the properties of the fluid were set to constant values calculated at 23.1 °C, which was the value obtained by averaging the initial temperatures measured by the thermistors. These properties are shown in Table 4. The initial saturation pressure in the tank was calculated from the initial tank temperature. The noncondensable gases were neglected in the model.

Table 4: Fluid properties used in the cases

Property	Vapor	Liquid
Density (kg/m^3)	Ideal gas	1567.618
c_p ($\text{J}/(\text{kg}\cdot\text{K})$)	656.621	916.037
k ($\text{W}/(\text{m}\cdot\text{K})$)	0.00840601	0.06864409
μ ($\text{kg}/(\text{m}\cdot\text{s})$)	9.52158E-6	0.000670957
h (J/kg)	.3728436	.2209084
β ($1/\text{K}$)		0.001516847
σ (N/m)		0.01742025

Thermistor Locations

In the paper describing the original experiment and its apparatus, Bentz (1993) provided a schematic showing the locations of the thermistors, shown in Figure 3. The locations of the thermistors inside the tank were given as follows:

Thermistors T2, T4, and T5 reach 2.54 ± 0.15 cm (1.0 ± 0.06 in) from the inside wall of the tank, and thermistor T1 extends 1.27 ± 0.15 cm (0.5 ± 0.06 in). Thermistors T3 and T6 are attached to heaters A and B.

Since the description given by Bentz did not provide the distance of each thermistor from the bottom of the tank, these distances were estimated using the schematic. Each thermistor was represented as a monitor point in the model; their locations are shown in Figure 15.

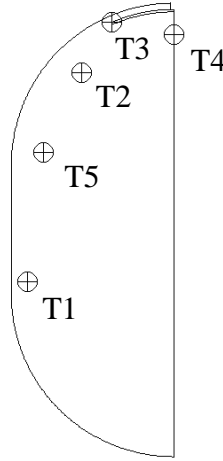


Figure 15: Thermistor locations in the axisymmetric case setup

Fluent Setup

Fluent version 15.0 was used to implement the model. The 2D axisymmetric computational domain for the validation case used an unstructured mesh of 28244 cells. In order to capture the moving interfaces between liquid and vapor, the transient explicit VOF scheme and transient implicit VOF scheme were compared. The explicit VOF scheme was used with first order time discretization, since second order time discretization is not available for the explicit scheme. It was also used with the geometric reconstruction scheme for the volume fraction. When the implicit VOF scheme was used, bounded second order time discretization was used. For these cases, the compressive scheme was used for the volume fraction, since geometric reconstruction is not available for the implicit VOF scheme. Using the VOF model allows the interface to deform, but the interface is diffused over several cells, rather than being sharp.

Both the PISO scheme and the coupled algorithm were used for the pressure-velocity coupling. The spatial discretization used least squares cell based for the gradient, body force weighted for the pressure, and second order upwind for density, momentum, and energy. The convergence criteria were set to 10^{-4} for continuity, 10^{-5} for the x- and y-

velocities, and 10^{-7} for energy during the self-pressurization period. During the boiling period, all of the variables converged to about 10^{-3} or better. The wall adhesion effects were included in Fluent; a contact angle of 0° was specified at each wall. The surface tension forces were included using the Continuum Surface Force model.

Self-pressurization and boiling were treated as separate periods. At the beginning of the self-pressurization period, the temperature field and the location of the ullage inside the tank were initialized according to estimates from the experimental data. The experimental tank was estimated to be about 83% full (Hasan, Lin, Knoll, & Bentz, 1996); this was used to calculate the size of the ullage. Either a heat flux or a temperature profile was applied to the heater; values for either condition were obtained from the experimental data.

A User Defined Function (UDF) imposed the mass transfer between phases. This mass transfer calculated by the UDF was applied by Fluent as a source term in “all relevant momentum and scalar equations (ANSYS, 2013a).” Fluent’s Theory Guide goes on to say that “this contribution is based on the assumption that the mass ‘created’ or ‘destroyed’ will have the same momentum and energy of the phase from which it was created or destroyed.” During self-pressurization, mass transfer was restricted to the interface. During boiling, mass transfer was restricted to the interface or to regions in the bulk liquid with a superheat above a threshold value, as shown in Equation 16; as the bubbles grew and developed an interface, the mass transfer to the bubbles was again restricted to the interface.

The time at which self-pressurization stopped and boiling began was a user-defined parameter. This time was estimated from Figure 7 and Figure 9. Figure 7 shows a sharp rise in pressure at about the time when boiling began, while Figure 9 shows a sharp drop

in the temperature of the heater at about the same time—the latter is an example of delayed boiling which can occur with a highly-wetting fluid such as Freon 113 (Muduwar, 2014).

Initial Location of the Ullage

In the model, the initial size of the ullage was based on the 83% fill level specified in the experiment description (Hasan, Lin, Knoll, & Bentz, 1996). The initial location of the ullage was based on the position of the ullage at the start of test 6, as shown in Figure 12. The distance from the bottom of heater A to the top of the ullage was somewhat difficult to determine from the photos, so two positions were tried in the model, as shown in Figure 16. In position a, the top of the ullage is located 5mm from the bottom of the heater, while in position b, it's 30 mm from the bottom of the heater.

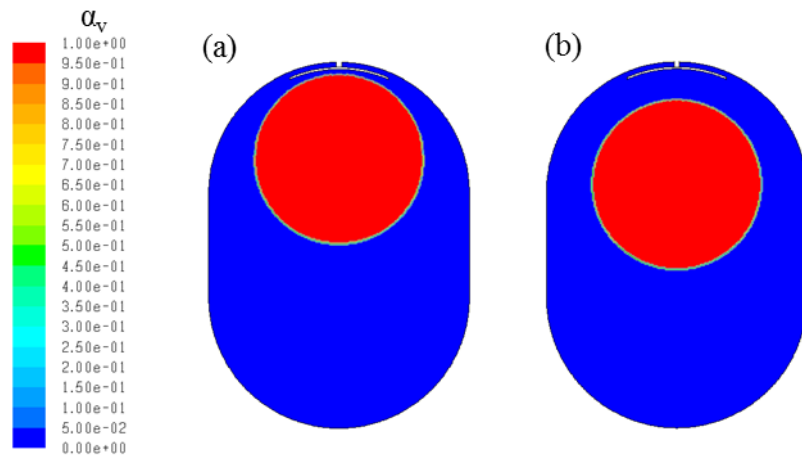


Figure 16: Initial locations of the ullage in the model (a) top of ullage 5mm from heater, (b) top of ullage 30mm from heater

CHAPTER VI

RESULTS

CFD Model of the TPCE—Preliminary Numerical Verification

Mesh Independence

A mesh independence test was conducted using transient, axisymmetric Volume of Fluid (VOF) cases in 0g, with no heat or mass transfer. Gambit was used to mesh the tank. The meshes varied in size from 1208 to 38141 elements, using different layouts. The time step size used for all of these cases was 1×10^{-3} s. (Time step size independence studies were run for the self-pressurization and boiling periods, as described later.) Each case was run for a total simulation time of 10s. The initial conditions for these cases were estimated from the conditions at the beginning of test 6 of the TPCE/TP experiment. The initial temperatures in the tank during the experiment, shown in Figure 8 and Figure 9, were averaged to obtain an initial uniform temperature that could be used for mesh independence cases; the value obtained was 23.1°C. The initial saturation pressure was calculated from this temperature. The ullage was initialized at the position shown in Figure 16a.

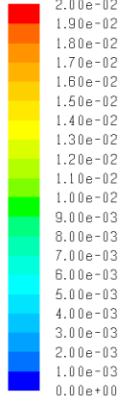
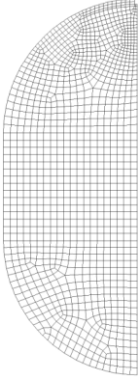
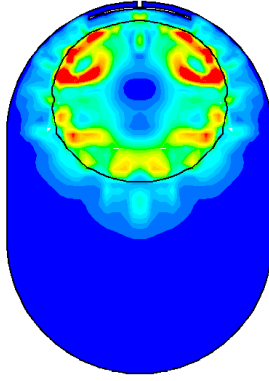
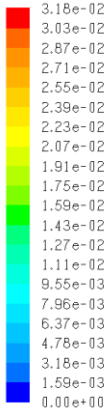
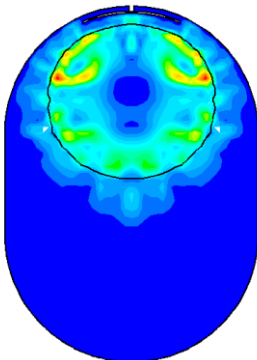
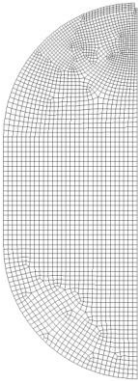
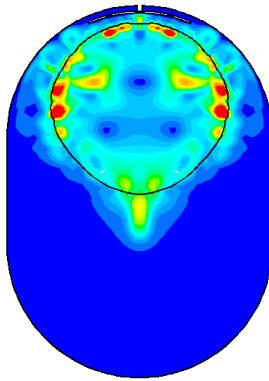
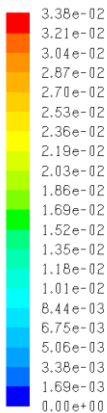
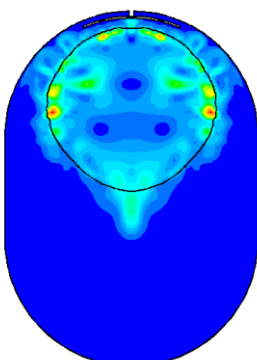
Since no forces were present to move the fluid, any fluid motion was due to the inaccuracy of the VOF scheme with regards to capturing the correct position of the

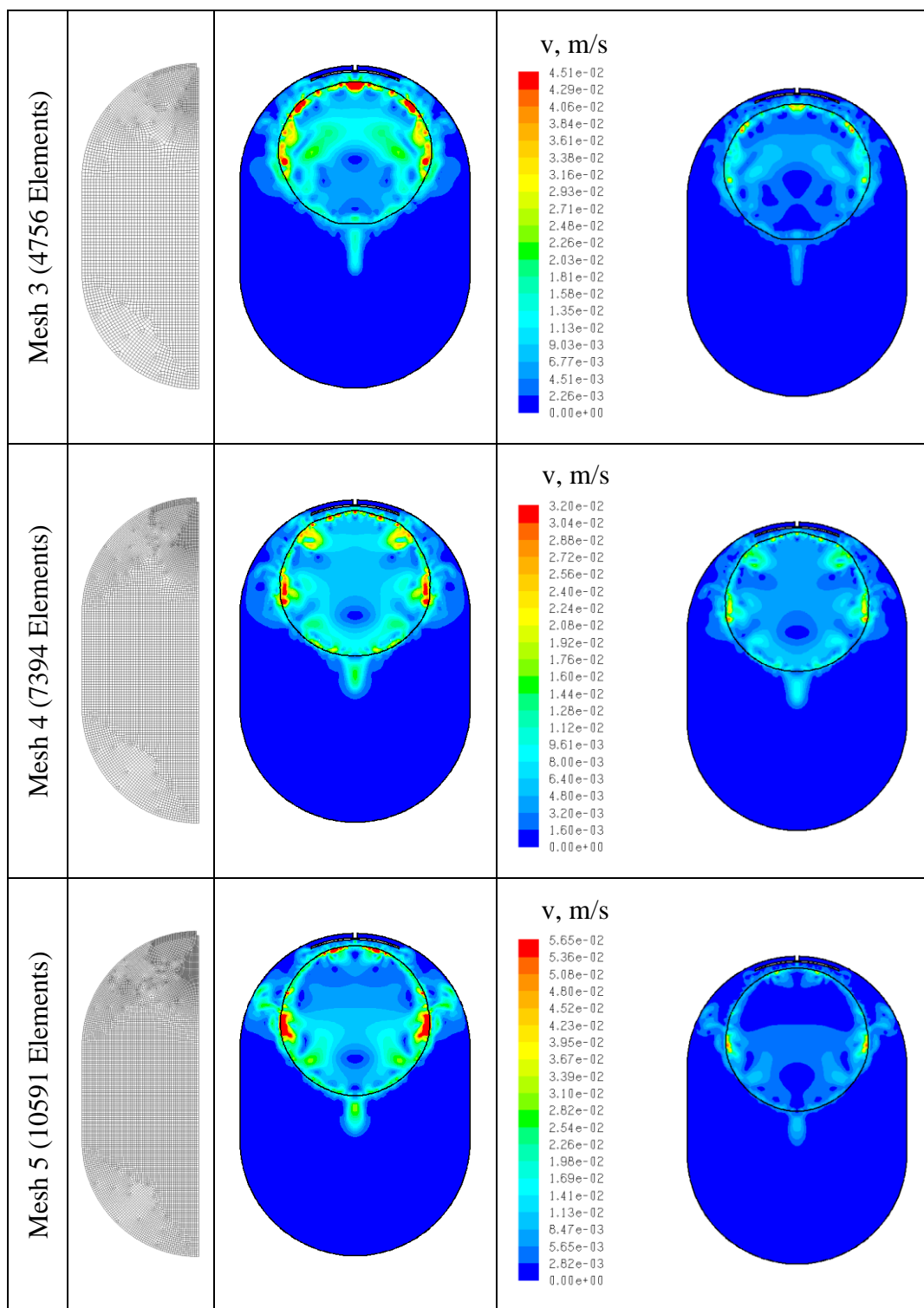
interface. This inaccuracy is greatest for a coarse or unresolved mesh. The meshes that were examined are shown in Table 5 below. Both the number of elements, and the alignment and distribution of the mesh, were varied between different meshes.

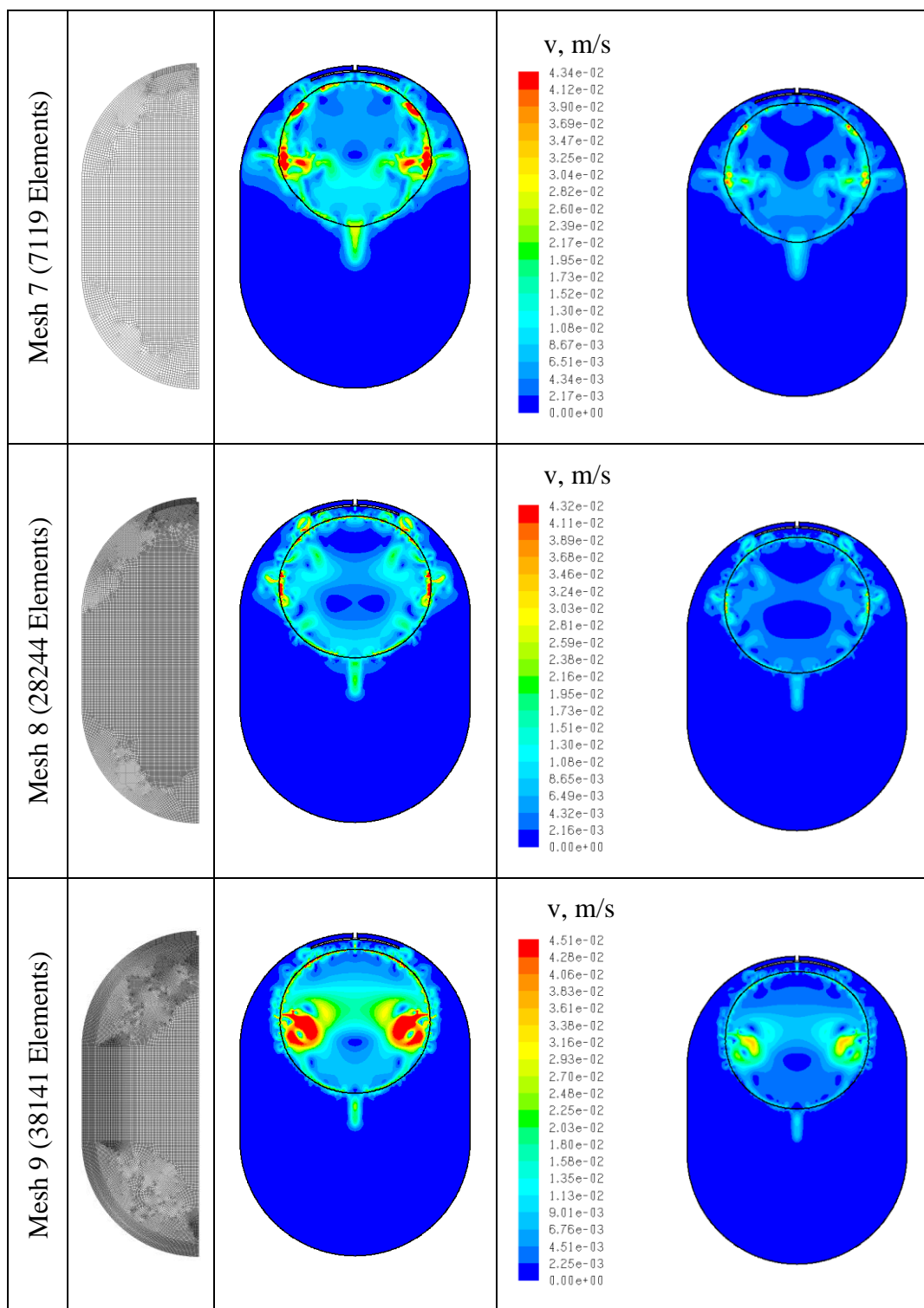
The velocity magnitude contours that resulted after 10s are also shown in Table 5. The interface is shown using black lines at isocontours of the volume fraction of vapor of 0.5. Almost all of the meshes that were tested resulted in maximum velocities on the order of $1 \times 10^{-2} \text{m/s}$. The velocity distribution did differ between meshes, as did the amount of deformation of the ullage. Most of the meshes had a region of higher velocity along the axis, as well as around the interface between the liquid and the vapor in the ullage.

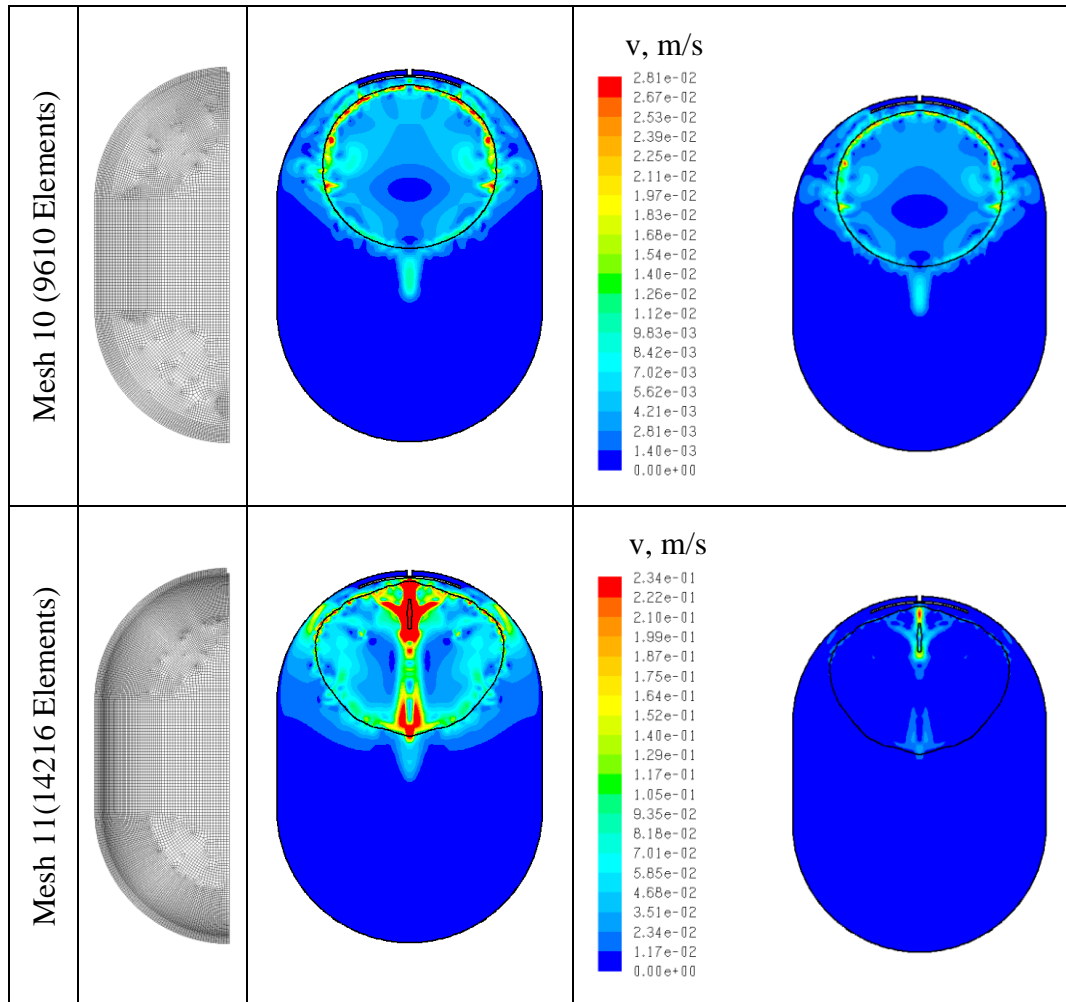
Since the results for mesh 8 seemed to restrict the higher velocities to a very small region, and had relatively large regions with lower velocities inside the ullage, this mesh was chosen for further runs.

Table 5: Mesh Independence Study

	Mesh	<p>Velocity at 10s</p> <p>$v, \text{m/s}$</p>  <p>2.00e-02 1.90e-02 1.80e-02 1.70e-02 1.60e-02 1.50e-02 1.40e-02 1.30e-02 1.20e-02 1.10e-02 1.00e-02 9.00e-03 8.00e-03 7.00e-03 6.00e-03 5.00e-03 4.00e-03 3.00e-03 2.00e-03 1.00e-03 0.00e+00</p>	<p>Velocity at 10s (m/s)</p> <p>(Individual scales are shown for each mesh)</p>
Mesh 1 (1208 Elements)			<p>$v, \text{m/s}$</p>  <p>3.18e-02 3.03e-02 2.87e-02 2.71e-02 2.55e-02 2.39e-02 2.23e-02 2.07e-02 1.91e-02 1.75e-02 1.59e-02 1.43e-02 1.27e-02 1.11e-02 9.55e-03 7.96e-03 6.37e-03 4.78e-03 3.18e-03 1.59e-03 0.00e+00</p> 
Mesh 2 (2658 Elements)			<p>$v, \text{m/s}$</p>  <p>3.38e-02 3.21e-02 3.04e-02 2.87e-02 2.70e-02 2.53e-02 2.36e-02 2.19e-02 2.03e-02 1.86e-02 1.69e-02 1.52e-02 1.35e-02 1.18e-02 1.01e-02 8.44e-03 6.75e-03 5.06e-03 3.38e-03 1.69e-03 0.00e+00</p> 







Gravity Study

Although the TPCE and TPCE/TP experiments did include accelerometers, these accelerometers were not meant to measure the background acceleration—instead, they were included to measure any sudden accelerations experienced by the tank (Bentz, 1993), (Hasan, Lin, Knoll, & Bentz, 1996). This was because the gravity level was assumed to be low enough that natural convection could be neglected (Bentz, 1993). As such, the readings when sudden accelerations did not occur show instrument bias rather than the actual gravity level (Hasan, Lin, Knoll, & Bentz, 1996). However, during the first flight of the experiment, the average acceleration due to drag was estimated at around $7 \cdot 10^{-7} g$

(Bentz, 1993), which calculates to approximately $6.9 \times 10^{-6} \text{ m/s}^2$. Since the experiment was flown on Space Shuttles both times, it may be reasonable to assume the same acceleration levels for both flights.

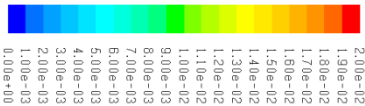
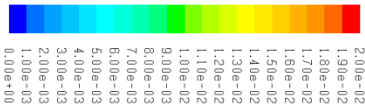
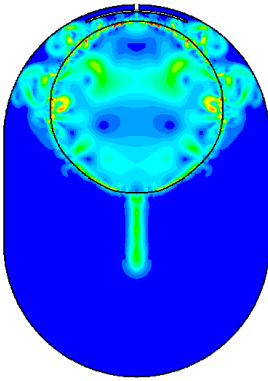
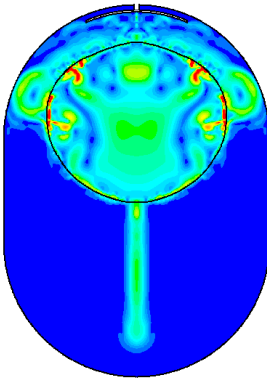
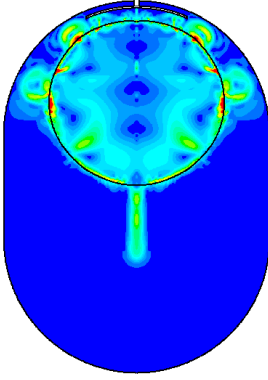
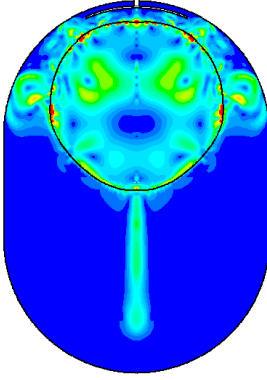
In order to see the effects of different gravity levels on the location of the ullage, mesh 8 from Table 5 was used to run some cases with varying accelerations due to gravity. The initial conditions for these cases were estimated from the conditions at the beginning of test 6 of the TPCE/TP experiment. The initial temperatures in the tank during the experiment, shown in Figure 8 and Figure 9, were averaged to obtain an initial temperature that could be used for the gravity study cases; the value obtained was 23.1°C . The ullage was initialized at the position shown in Figure 16a.

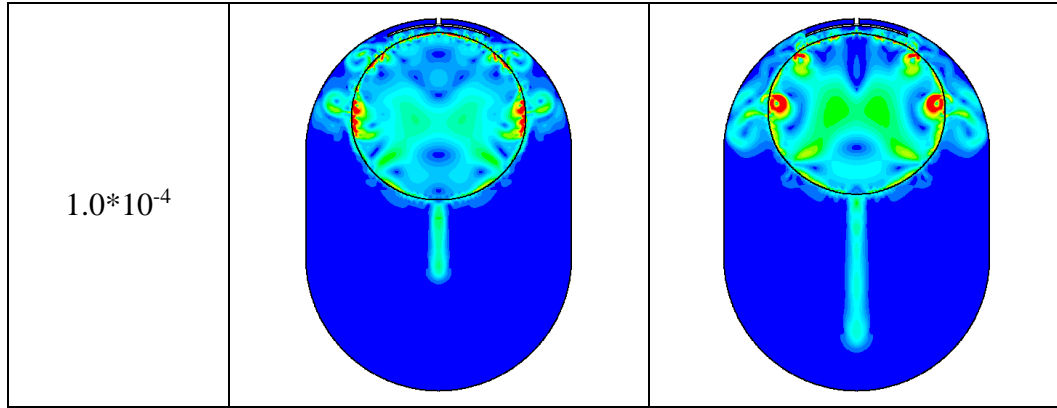
Since the accelerometers in the experiment measured occasional larger accelerations on the order of $1 \times 10^{-3} \text{ m/s}^2$, while they measured background accelerations on the order of $1 \times 10^{-4} \text{ m/s}^2$, the largest acceleration due to gravity that was used in the gravity study cases was $1.0 \times 10^{-4} \text{ m/s}^2$. The acceleration due to gravity was oriented as shown in Figure 14, so that the ullage would rise to the top of the tank, where the heater is. The results of these cases are shown in Table 6, at simulation times of 20s and 40s. All of these cases were run using a time step size of $1.0 \times 10^{-3} \text{ s}$. The interface is shown using black lines at isocontours of the volume fraction of vapor of 0.5.

Interestingly, the results of the case with an acceleration due to gravity of $1.0 \times 10^{-6} \text{ m/s}^2$ show that the ullage moved downward in the tank, in the opposite direction to that which should have been induced by gravity. The ullage in the case with an acceleration due to gravity of $1.0 \times 10^{-5} \text{ m/s}^2$ also appears to have moved down somewhat. Only the case with an acceleration due to gravity of $1.0 \times 10^{-4} \text{ m/s}^2$ kept the ullage near the heater, where it was

located at the beginning of the case. In order to have the ullage stay in approximately the same location during the self-pressurization period, $1.0 \cdot 10^{-4} \text{ m/s}^2$ was chosen as the acceleration due to gravity for all of the validation cases, even though this does not match the experiment conditions.

Table 6: Effect of Gravity

Acceleration due to gravity (m/s^2)	Velocity after 20s (m/s) 	Velocity after 40s (m/s) 
$1.0 \cdot 10^{-6}$		
$1.0 \cdot 10^{-5}$		



CFD Simulation of the Self-Pressurization Period during Test 6

In the experiment, the tank self-pressurized for a while before boiling began. During self-pressurization, the temperature of the heater rose, as shown in Figure 9. Boiling was assumed to have begun at the time the heater temperature dropped; from this, the duration of the self-pressurization period was estimated as being about 164.7s. For the CFD model, the self-pressurization and boiling periods were treated as separate periods. Before the boiling period could be modeled, the self-pressurization period had to be simulated.

In modeling the self-pressurization period, either a heat flux or a temperature profile can be applied to the heater, heating up the liquid. Evaporation and condensation occurred at the interface, but boiling was not allowed to occur in the bulk liquid. The self-pressurization period was assumed to be in a near-equilibrium condition, as described in the Mathematical Model section. Therefore, all mass transfer was calculated using Equation 25, with the accommodation coefficient set to $\sigma = 0.001$. Several different cases were run using either the heat flux or heater temperature as inputs, in an attempt to match the experimental results.

Time Step Size Independence Study for Self-Pressurization Period

A time step size independence study was conducted for the self-pressurization period. The initial conditions for these cases were estimated from the conditions at the beginning of test 6 of the TPCE/TP experiment. The initial temperatures in the tank during the experiment, shown in Figure 8 and Figure 9, were averaged to obtain an initial temperature that could be used for the time step independence study cases; the value obtained was 23.1°C. The ullage was initialized at the position shown in Figure 16a. The heater used a constant heat flux of 16.6 W, to match the experiment (Hasan, Lin, Knoll, & Bentz, 1996).

These cases used mesh 8 from Table 5, and a gravity level of $1 \times 10^{-4} \text{ m/s}^2$, which had the best results of the gravity levels that were tried, as shown in Table 6. Three time step sizes were used: $1.0 \times 10^{-3} \text{ s}$, $5.0 \times 10^{-4} \text{ s}$, and $1.0 \times 10^{-4} \text{ s}$. The results are shown in Figure 17, for the pressure, and Figure 18, for the temperature along the bottom surface of the heater. The results for the cases with a time step size of $5.0 \times 10^{-4} \text{ s}$ and $1.0 \times 10^{-4} \text{ s}$ were very similar, so further self-pressurization cases prior to boiling were run using a time step size of $5.0 \times 10^{-4} \text{ s}$.

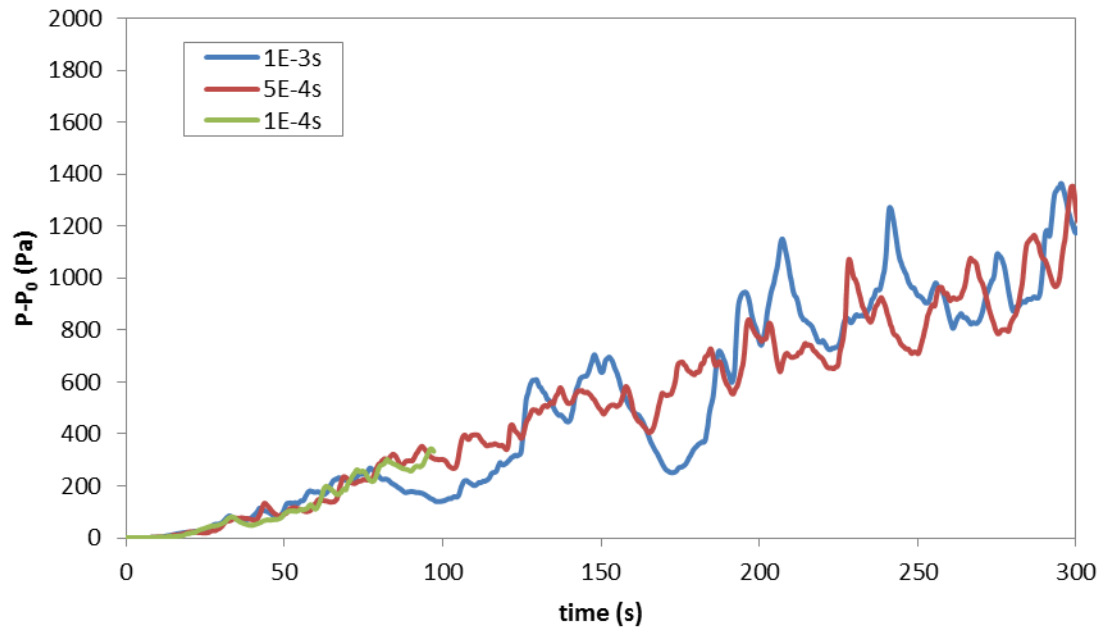


Figure 17: Time step size independence study for self-pressurization: Pressure

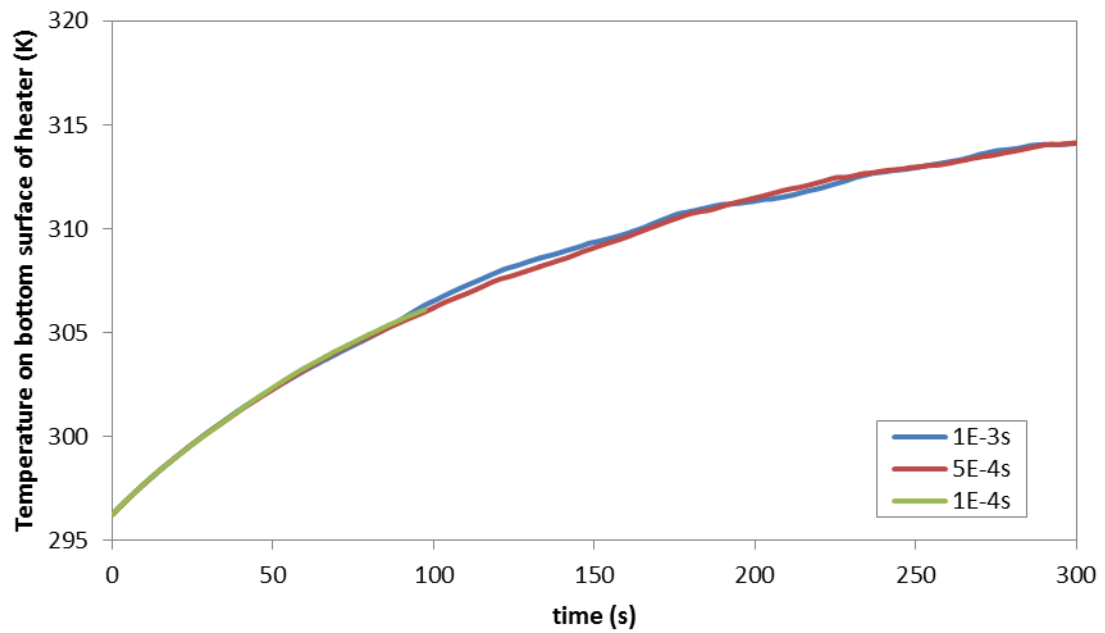


Figure 18: Time step independence study for self-pressurization: Temperature on bottom surface of heater

Initial Conditions

An initial self-pressurization case was run with the ullage located as shown in Figure 16a. The experimental heat flux at heater A was applied at the heater. The tank was initialized to a uniform temperature of 23.1 °C, which was the temperature obtained by averaging the initial temperatures in the tank during the experiment, shown in Figure 8 and Figure 9. The pressure in the tank, as well as the temperatures at monitor points located approximately where the thermistors were located in the experiment, were monitored for comparison with the experimental data. Since the locations of the thermistors were not provided with enough detail to determine the exact locations of the thermistors inside the tank, the temperatures at each of the thermistors in the case can only be compared qualitatively with the experimental data. The results are shown in Figure 19 through Figure 24.

A small amount of noncondensable gas was included in the tank during the TPCE/TP experiment; the mass fraction of this gas was estimated as varying from 0.5 to 2.0% (Hasan, Lin, Knoll, & Bentz, 1996). Since this noncondensable gas was not included in the model, the tank pressure in the model was set to the saturation pressure of the fluid, rather than the value measured by the experiment. Therefore, comparisons between the pressure predicted by the model and the pressure measured in the experiment were made using the change from the respective initial pressures.

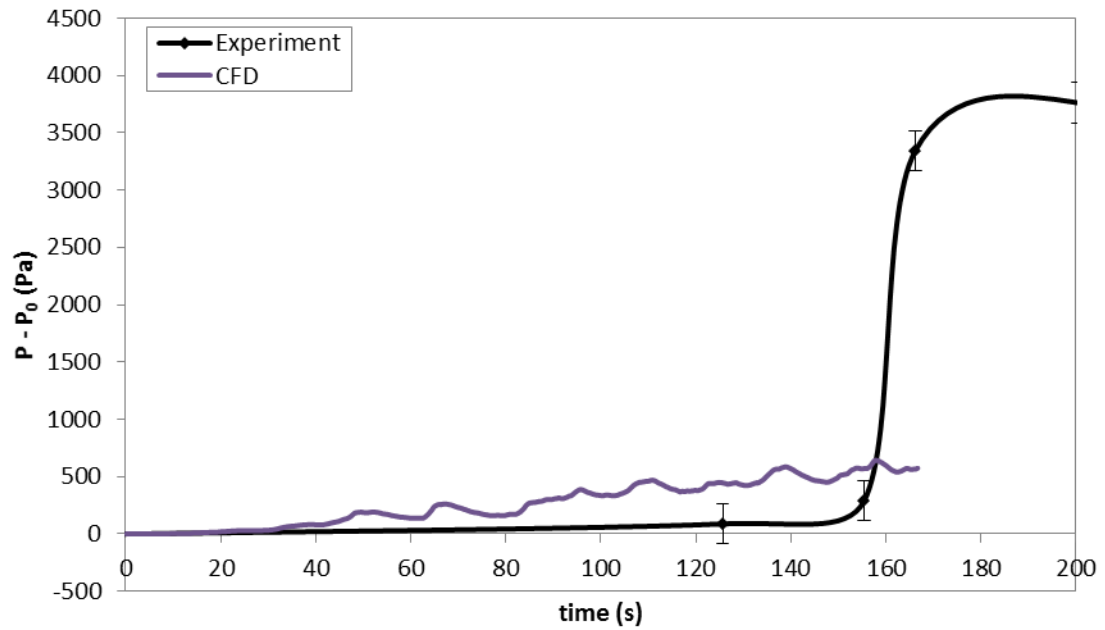


Figure 19: Pressure rise during initial self-pressurization case

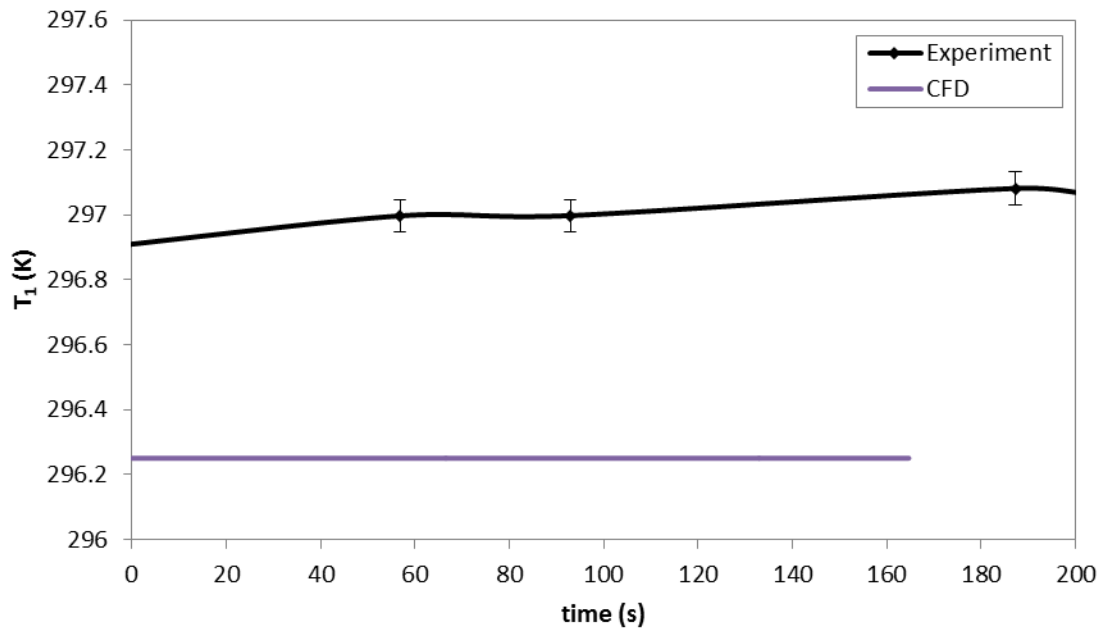


Figure 20: Temperature at T1 during initial self-pressurization case

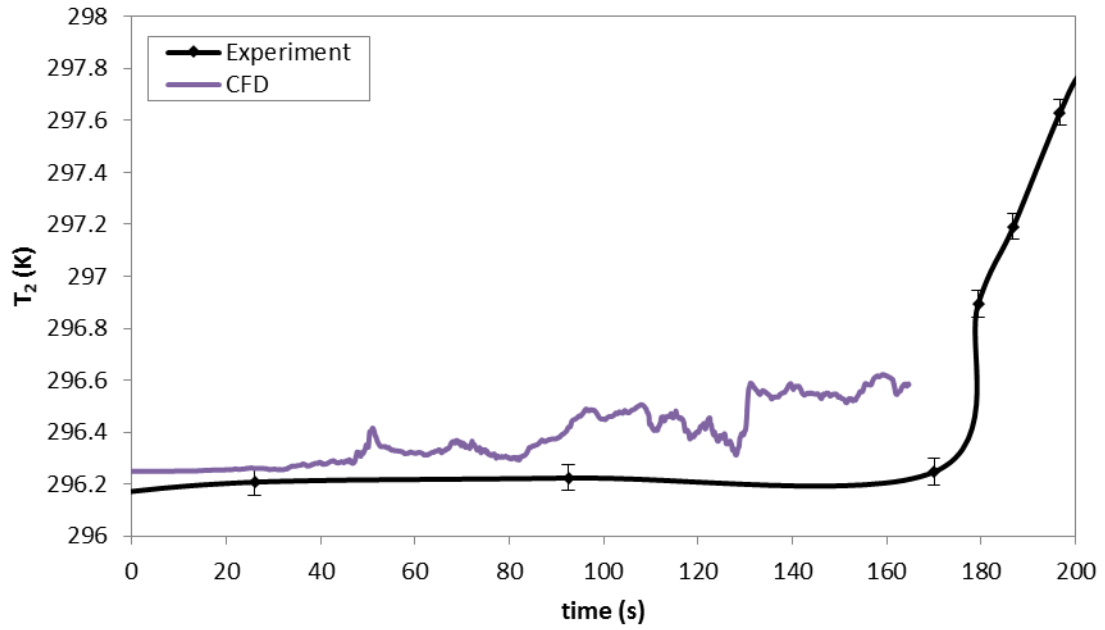


Figure 21: Temperature at T₂ during initial self-pressurization case

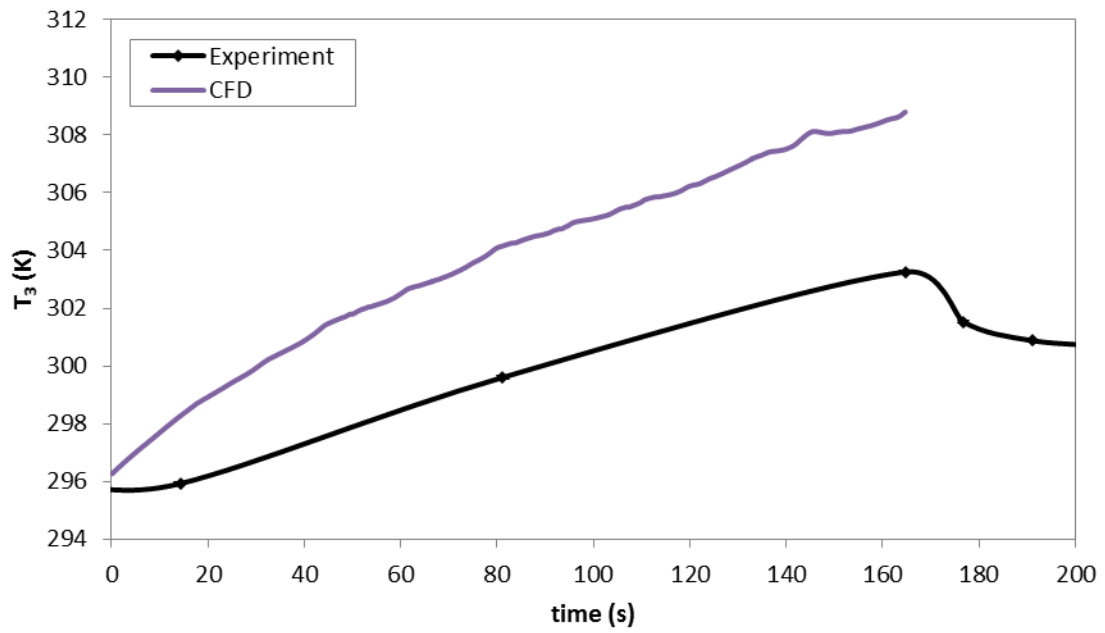


Figure 22: Temperature at T₃ during initial self-pressurization case

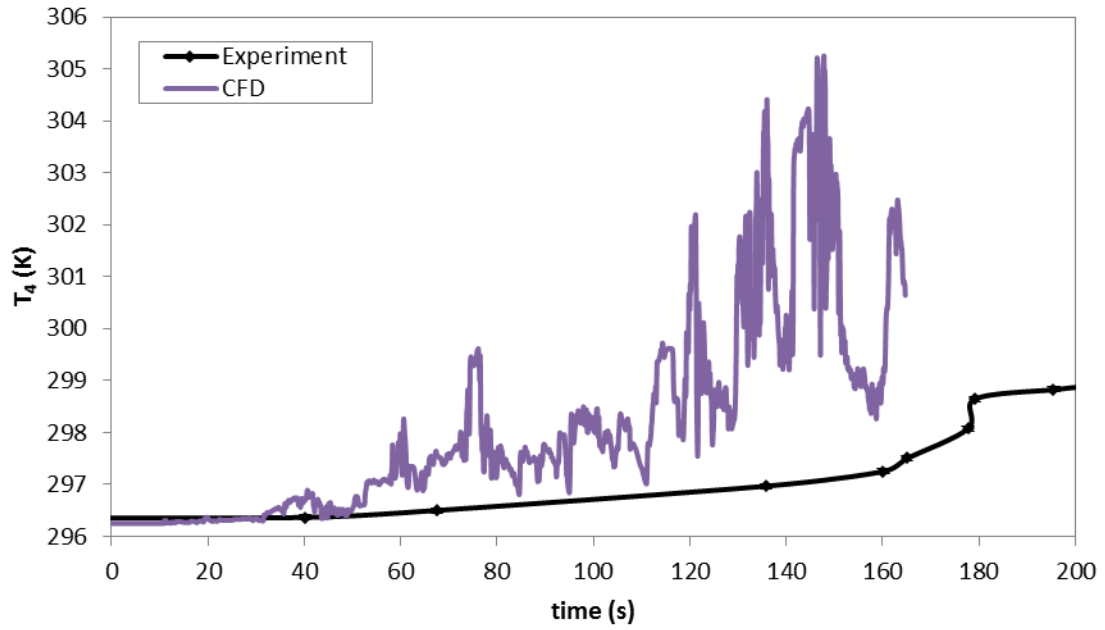


Figure 23: Temperature at T4 during initial self-pressurization case

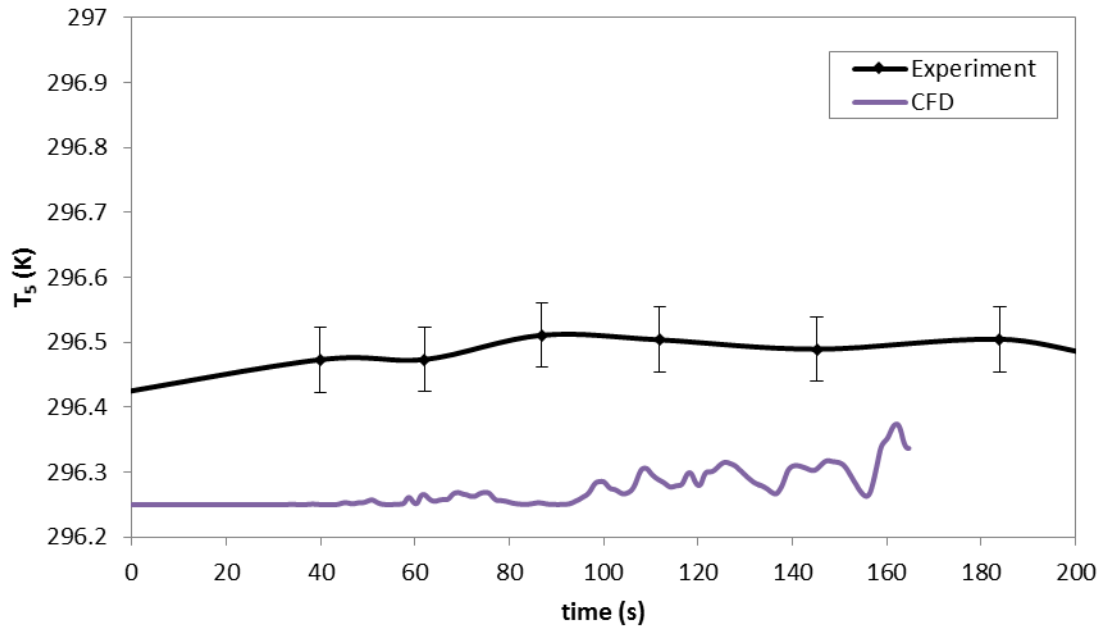


Figure 24: Temperature at T5 during initial self-pressurization case

As shown in Figure 19 through Figure 24, the temperatures in this initial case did not correspond well to the temperatures seen during the experiment. In order to get a better

agreement with the temperatures measured by the thermistors, a linear curve fit of the temperature along the central axis of the tank was desired. Since the exact location of each of the thermistors was not available, it was not possible to obtain an entirely accurate temperature profile inside the tank. However, two estimates of the temperature profile were created.

The first estimate of the initial temperatures measured in the tank was created by plotting the initial temperatures measured by thermistors 1-6 and creating a linear curve-fit along the axis of the tank, as shown in Figure 25. However, this did not produce a very good linear fit.

A second linear curve-fit of the temperature along the tank axis was made using only thermistors 1, 2, 3, and 5, as shown in Figure 26. Thermistors T4 and T6 were left out because T4 was assumed to have been inside the ullage, while T6 was attached to heater B, which had been used in the previous tests (Hasan, Lin, Knoll, & Bentz, 1996); it was therefore assumed that neither of these thermistors were measuring the temperature of the bulk liquid in the tank at their respective locations. This curve fit was used for the initial temperature in the tank for each subsequent self-pressurization case.

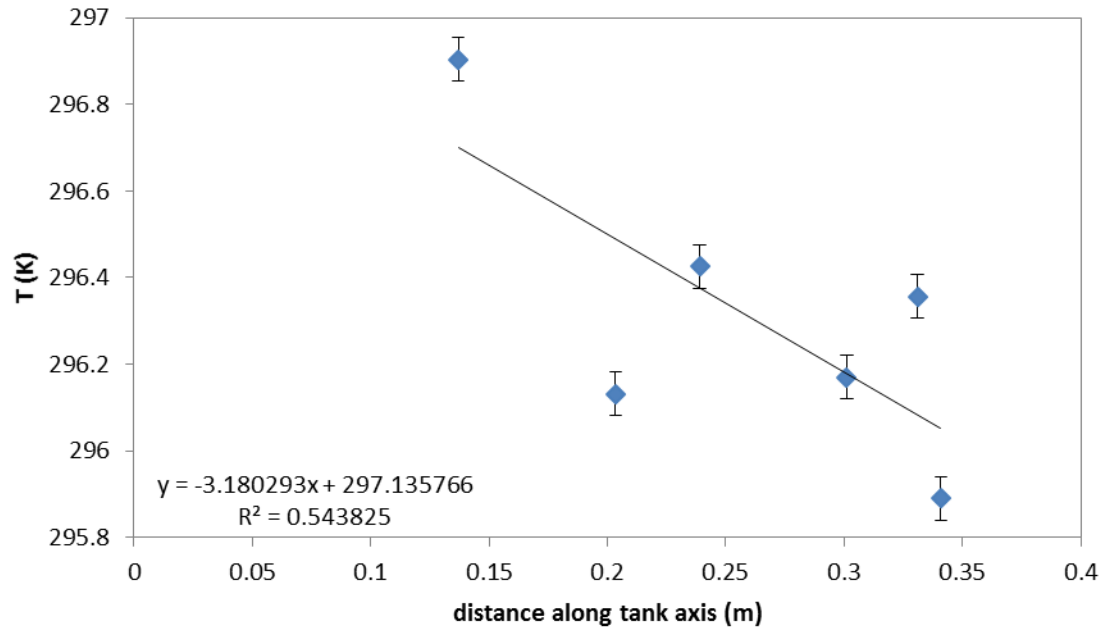


Figure 25: Curve fit of the initial temperatures in the tank as measured by all six thermistors inside the tank

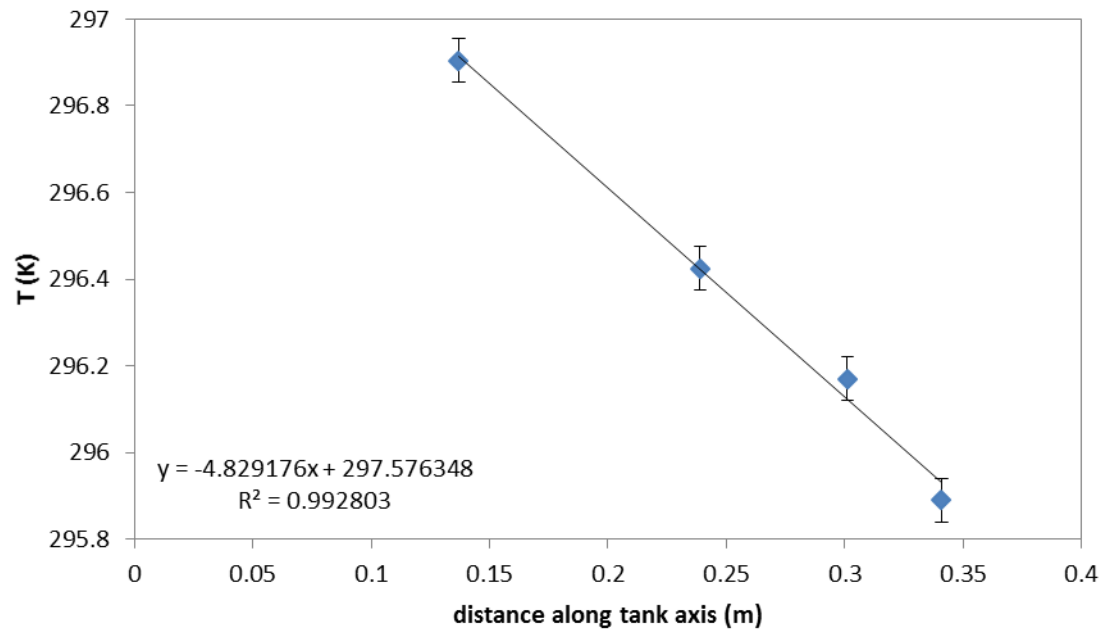


Figure 26: Curve fit of the initial temperatures in the tank as measured by thermistors T1, T2, T3, and T5

Results of the Self-Pressurization Study

Several cases were run to model the self-pressurization period. Two locations for the ullage were used, as shown in Figure 16 a and b. For each of these cases, the tank was initialized with the linear temperature profile from Figure 26; the initial temperature contours in the tank are shown in Figure 27. The interface is shown using black lines at isocontours of the volume fraction of vapor of 0.5. Two different conditions were applied to Heater A: the first was to apply a constant heat flux of 16.6 W at the heater, which matched the value used in the experiment; the second was to apply a temperature profile as a boundary condition on the heater surfaces. This temperature profile was a result of multiple curve fits to the digitized version of the temperature measured by thermistor T3 in the TPCE/TP experiment (Hasan, Lin, Knoll, & Bentz, 1996); these curve fits are shown in Appendix B.

The pressure in the tank, as well as the temperatures at monitor points located approximately where the thermistors were located in the experiment, were monitored and compared with the experimental data. The locations of each of these thermistors in the axisymmetric case are shown in Figure 15. As stated before, the fact that the locations of the thermistors are approximate means that the behavior of the temperature curves at each of the thermistor locations can only be compared qualitatively with the experimental data. The results are shown in Figure 28 through Figure 33.

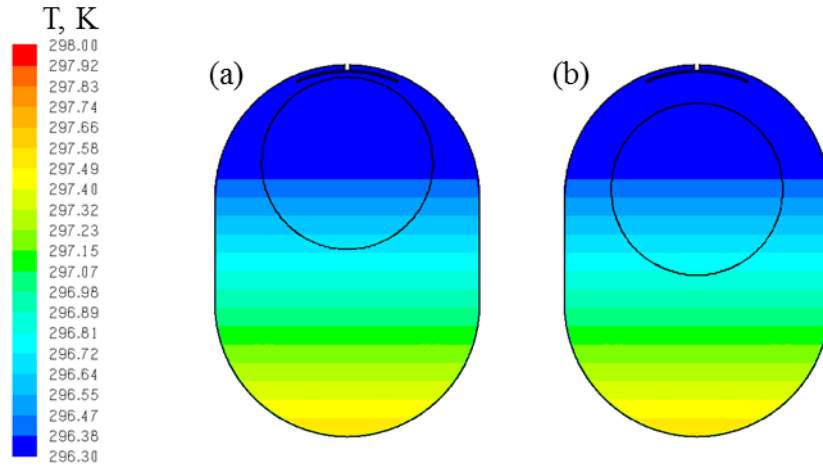


Figure 27: Initial temperature gradient imposed on the tank (a) top of ullage 5mm from heater, (b) top of ullage 30mm from heater

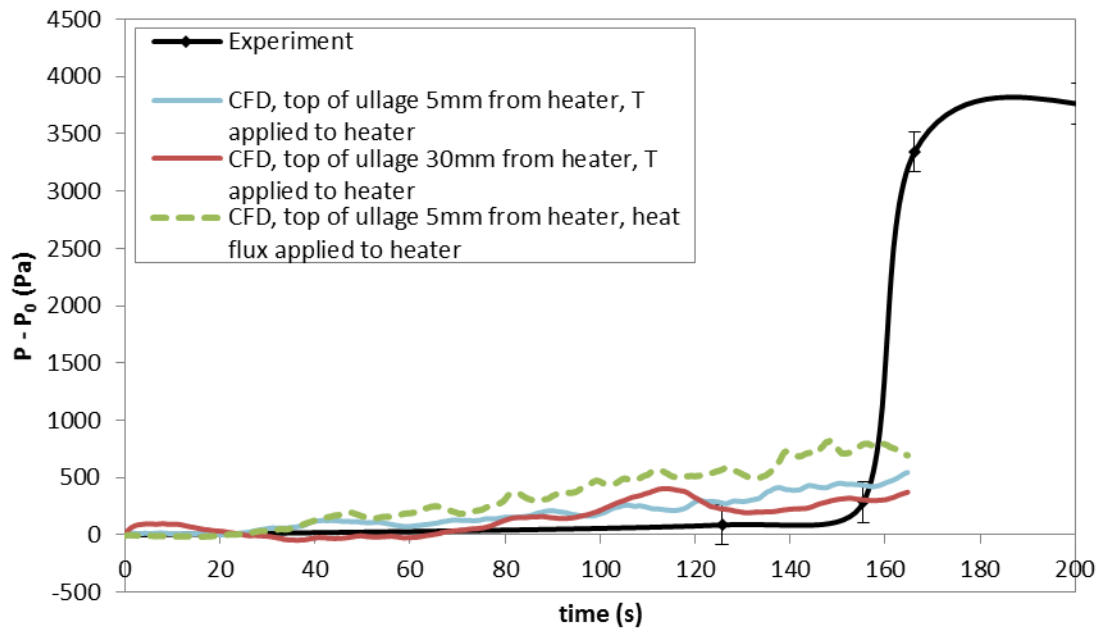


Figure 28: Pressure rise during self-pressurization

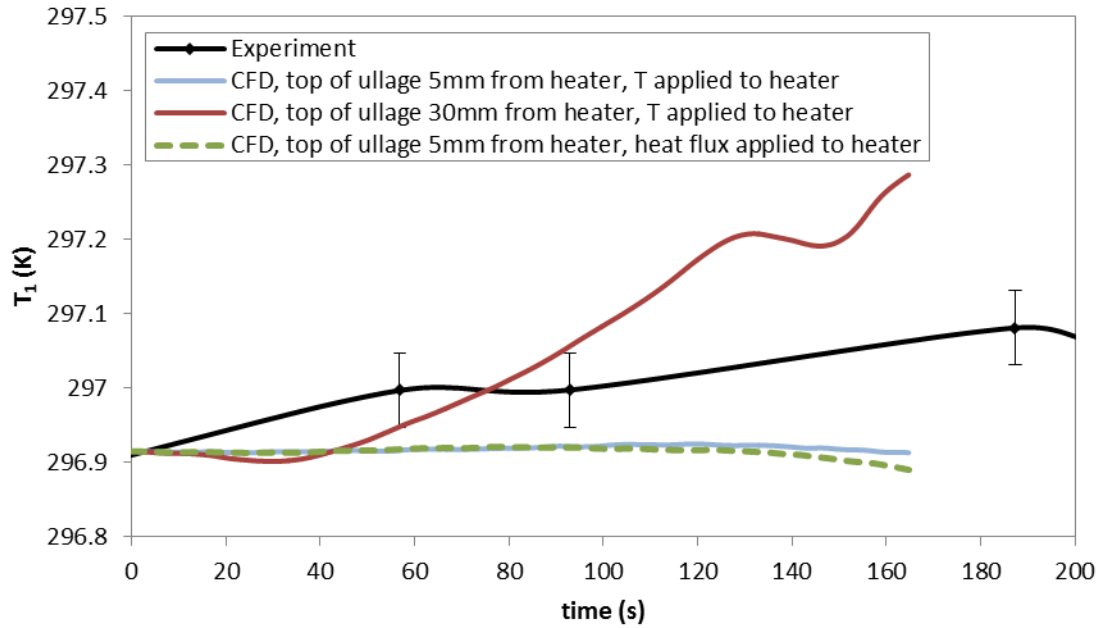


Figure 29: Temperature at T1 during self-pressurization

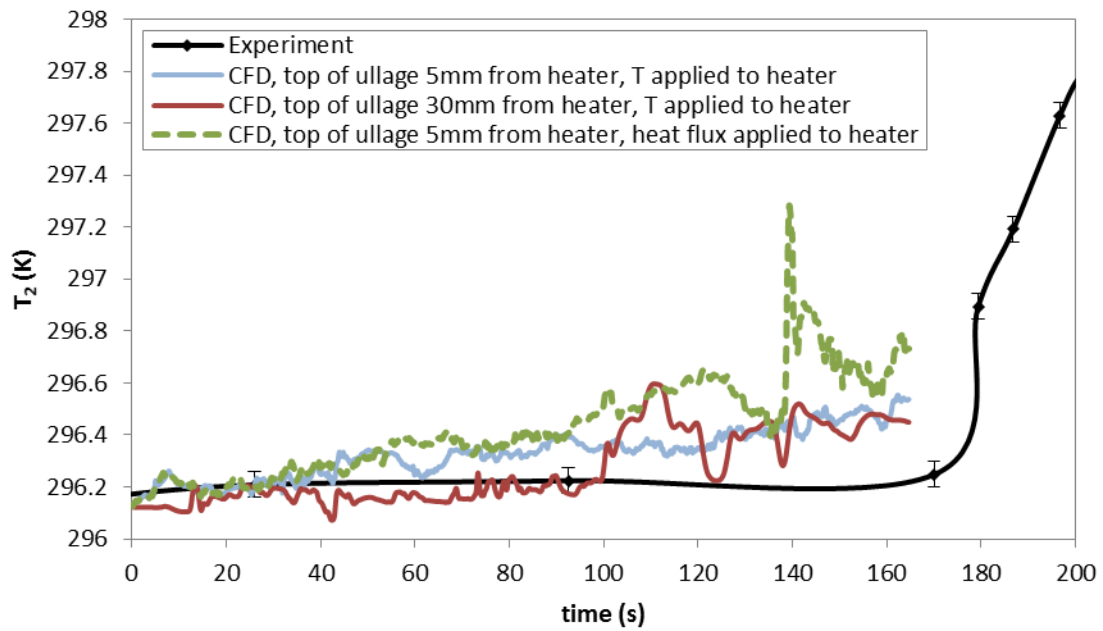


Figure 30: Temperature at T2 during self-pressurization

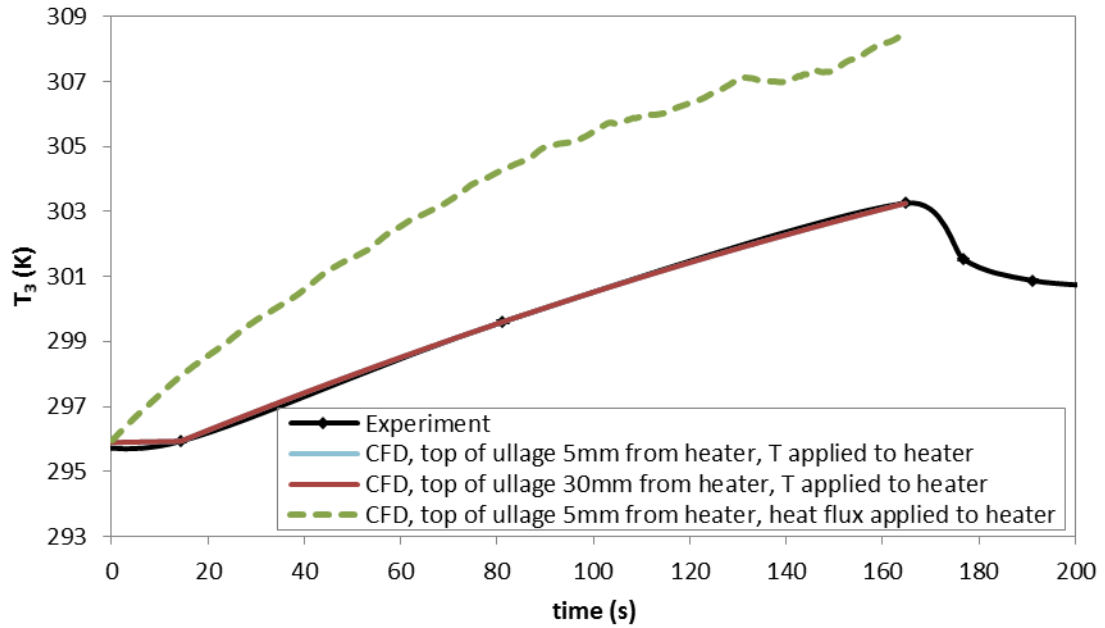


Figure 31: Temperature at T3 during self-pressurization

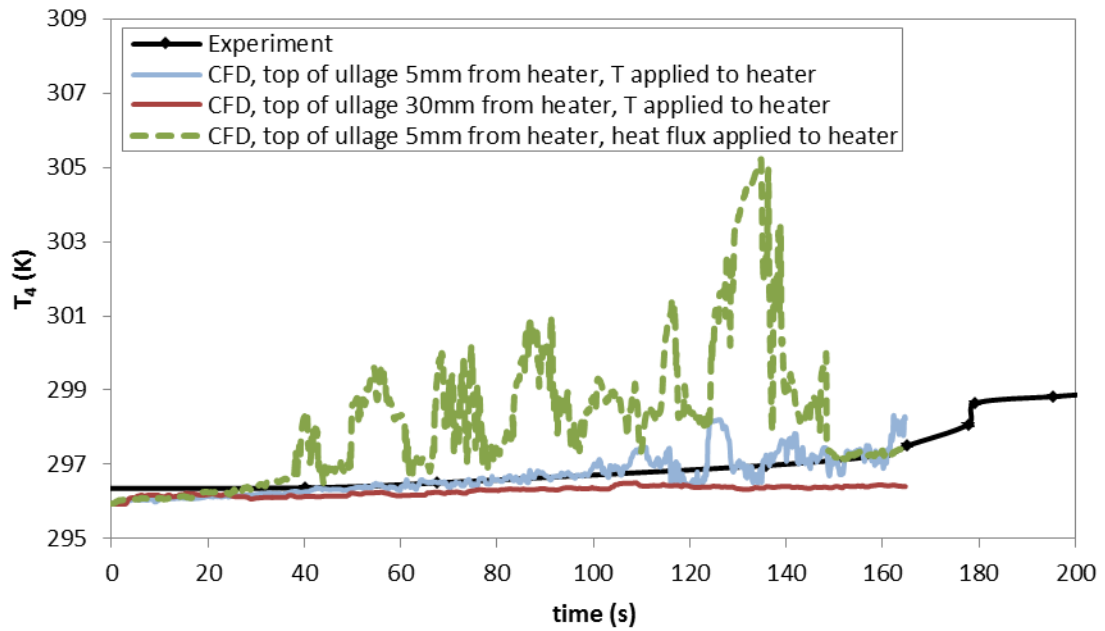


Figure 32: Temperature at T4 during self-pressurization

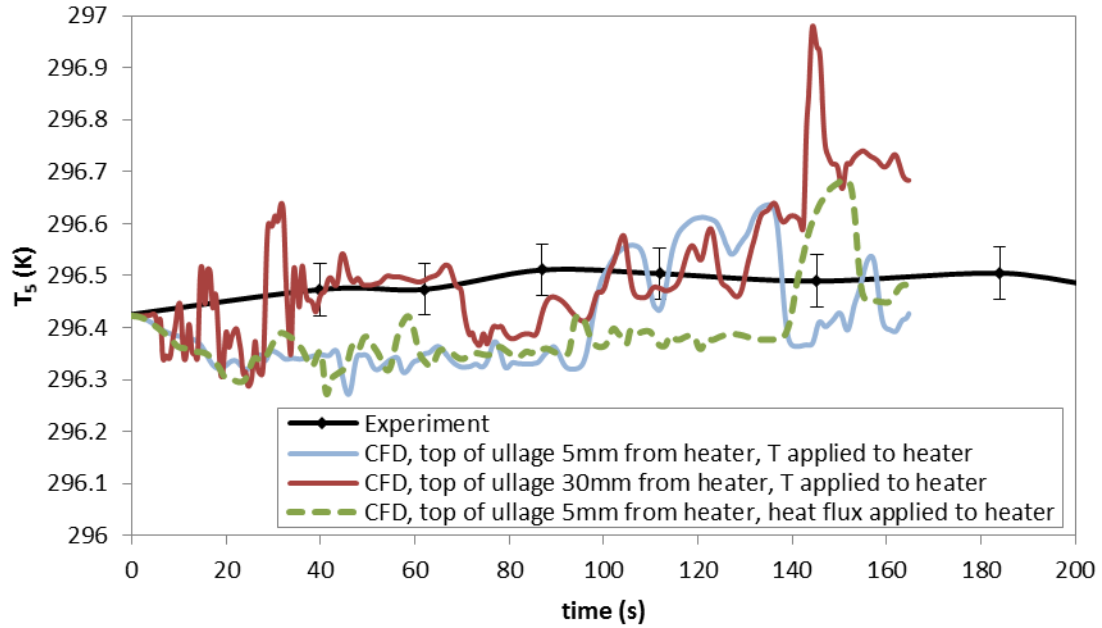
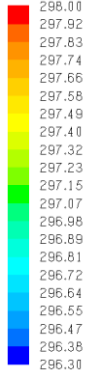
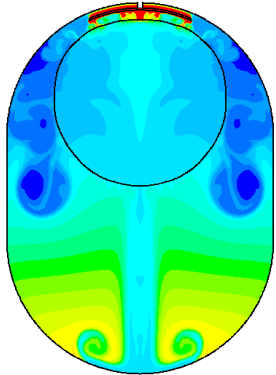
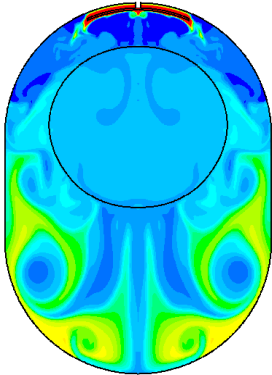


Figure 33: Temperature at T5 during self-pressurization

As shown in Figure 29 through Figure 33, the predicted temperatures at each monitor point did not always correspond well with the temperatures seen in the experiment. The most important temperature was the heater temperature, which drove the boiling. The case where the heat flux was applied at the heater did not match the experimental heater temperature well. It was therefore decided to proceed to modeling the boiling period using the results of one of the cases where the heater temperature was applied as a profile. The temperature contours inside the tank as calculated by the model at the end of the self-pressurization period, for the cases where the heater temperature was applied as a boundary condition, are shown in Table 7. The interface is shown using black lines at isocontours of the volume fraction of vapor of 0.5. Since varying the location of the ullage didn't seem to have much effect on the pressure, and since the initial location of the ullage in the experiment, shown in Figure 12, seemed to match the case with the top of the ullage

initially located 5mm from the heater best, it was decided to use the results of this case for the start of the boiling cases.

Table 7: Temperature contours in the tank at the end of the self-pressurization period, as calculated by the model

	Ullage 5mm below heater, T profile applied to heater	Ullage 30mm below heater, T profile applied to heater
<p>T, K</p> 		

CFD Simulation of the Boiling Period during Test 6

From Figure 7 and Figure 12, the tank self-pressurized for some time before boiling began. For the CFD model, the self-pressurization and boiling periods were treated as separate periods. The time at which boiling started was a user-defined parameter. The initial conditions for the boiling period were taken from the end of the self-pressurization period.

During the boiling period, in addition to evaporation and condensation at the interface between the liquid and vapor phases, boiling was also allowed to occur in the bulk liquid. A temperature profile was applied at the heater. This temperature profile was a result of multiple curve fits to the digitized version of the temperature measured by thermistor T3 in the TPCE/TP experiment (Hasan, Lin, Knoll, & Bentz, 1996); these curve fits are shown

in Appendix B. Two different methods of calculating the mass transfer due to boiling were used.

Under-Relaxation Factor for Mass Transfer Calculations in the UDF

In order to aid convergence in the boiling cases, an under-relaxation factor was applied to the mass transfer calculations performed in the UDF. The mass transfer was calculated using Equation 25, with an accommodation coefficient of 0.001. The pressures predicted by the model, both with and without the under-relaxation factor, are shown in Figure 34; as expected, the under-relaxation factor had no effect on the pressure rise due to boiling, but did aid the convergence in the case. Therefore, all further boiling cases used this under-relaxation factor.

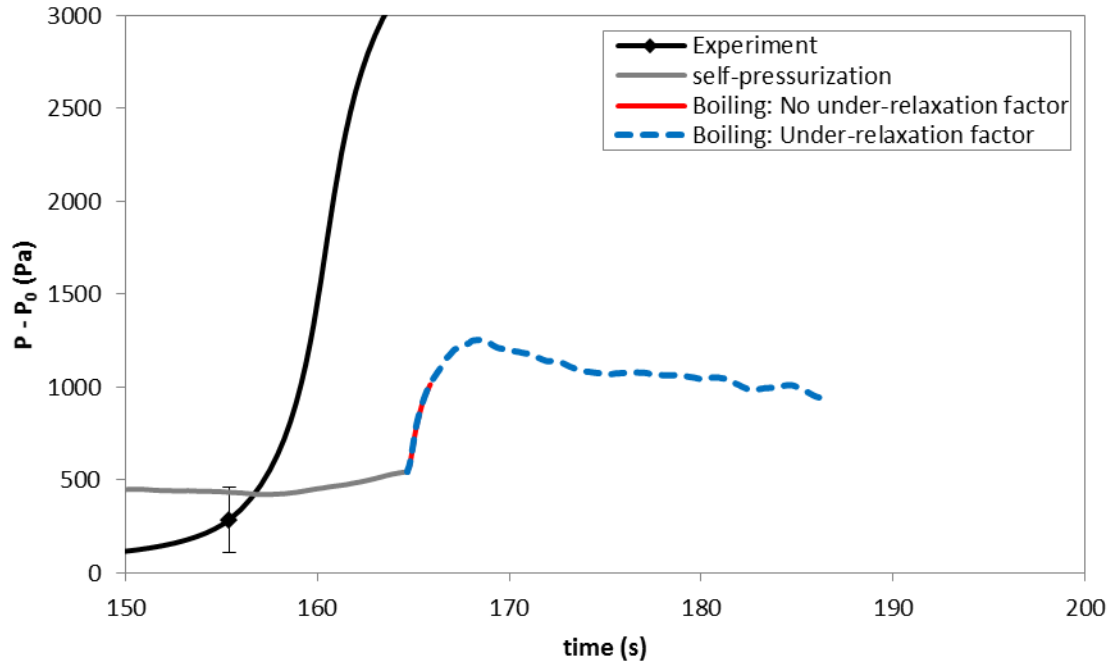


Figure 34: Effect of the under-relaxation factor applied to mass transfer on the pressure rise during boiling

Time Step Independence Study for Boiling

Time step size independence studies were conducted for the boiling period. The initial conditions for these cases were taken from the results of the self-pressurization case where the top of the ullage was initialized to 5 mm from the heater, and where a temperature profile was applied to the heater (results from this case were shown in Figure 28 through Figure 33). As stated before, these cases used mesh 8 from Table 5, and a gravity level of $1.0 \times 10^{-4} \text{ m/s}^2$.

First, a time step size independence study was run for the explicit VOF model with first order time discretization. These cases used the Schrage equation, with one accommodation coefficient, to calculate the mass transfer. Equation 25 was used to calculate the mass transfer, with the accommodation coefficient set to $\sigma = 0.01$. Three time step sizes were used: $5.0 \times 10^{-4} \text{ s}$, $1.0 \times 10^{-4} \text{ s}$, and $5.0 \times 10^{-5} \text{ s}$. A fourth time step size, $1.0 \times 10^{-5} \text{ s}$, was attempted, but the case diverged. The results are shown in Figure 35. The results for all three cases were very similar.

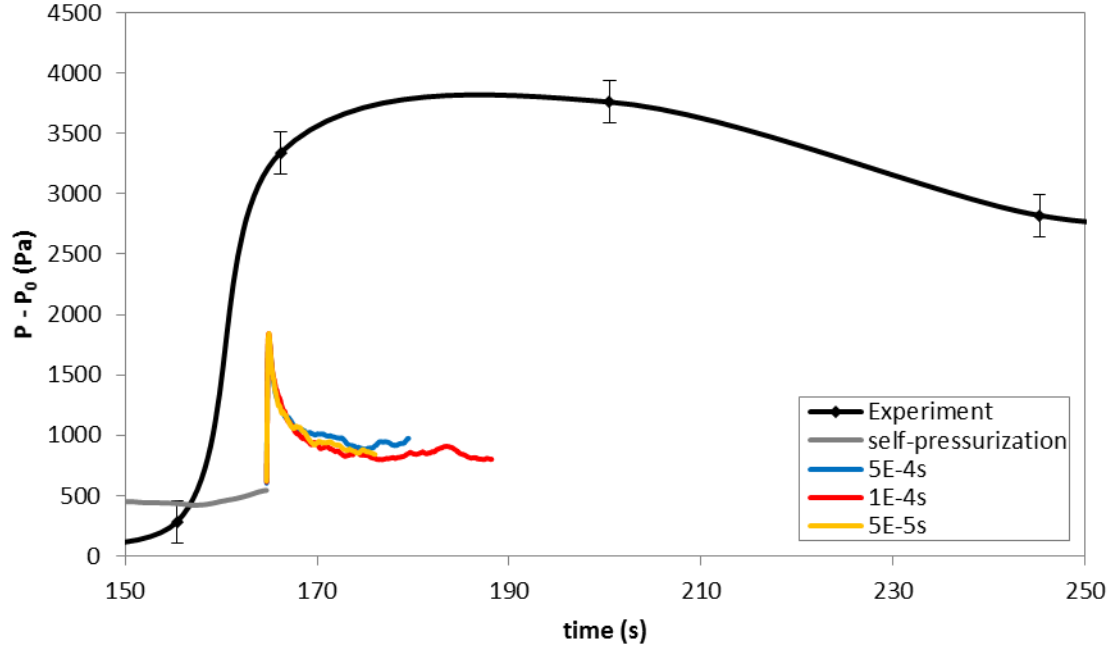


Figure 35: Time step size independence study for boiling using the explicit VOF scheme

A second time step size independence study was run for the implicit VOF model with bounded second order time discretization; the results are shown in Figure 36. These cases used the Schrage equation to calculate the mass transfer, with different accommodation coefficients for evaporation, condensation, and boiling. The mass transfer was calculated using Equation 22, with accommodation coefficients of $\sigma_b = 0.1$, $\sigma_e = 0.005$, and $\sigma_c = 0.00001$. Two time step sizes were used: 5.0×10^{-4} s and 1.0×10^{-4} s. The threshold superheat was set to 3K for these cases. The initial pressure rises were very similar for both cases.

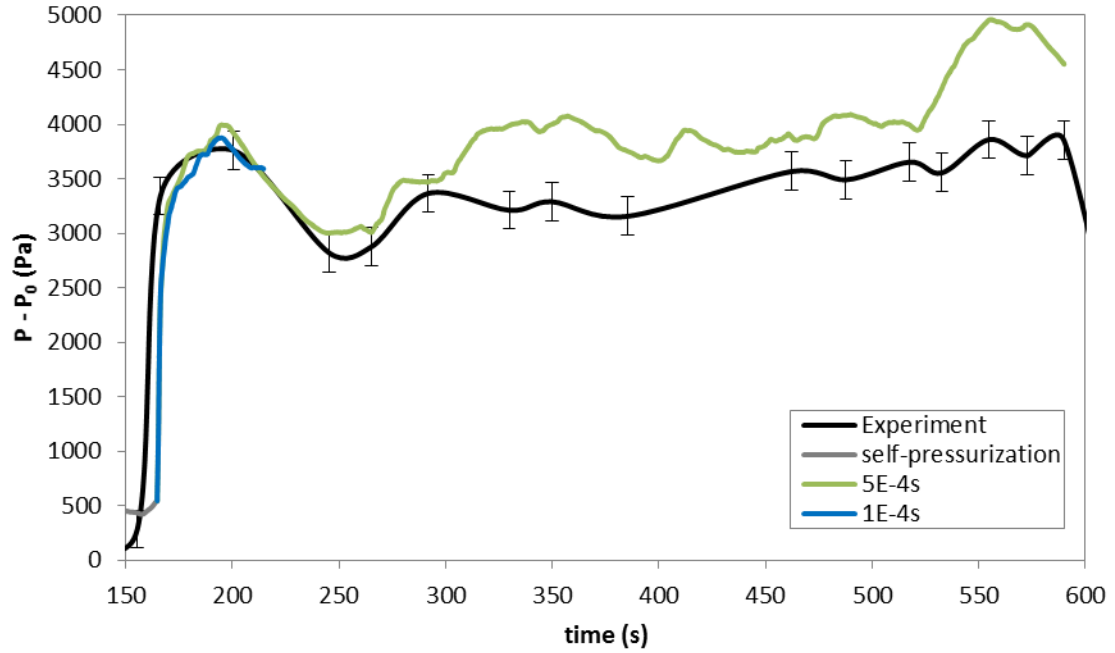


Figure 36: Time step size independence study for boiling using the implicit VOF scheme

From this point, all explicit VOF boiling cases with first order time discretization used a time step size of 1.0×10^{-4} s. All of the implicit VOF boiling cases with bounded second order time discretization used a time step size of 5.0×10^{-4} s.

Boiling Threshold Superheat Temperature Study

In the model, mass transfer due to boiling was restricted to regions in the bulk liquid with superheat temperatures that were greater than a user-defined threshold, as shown in Equation 16. A study was conducted to see the effects of varying the value of the threshold superheat. The initial conditions for these cases were taken from the results of the self-pressurization case where the top of the ullage was initialized to 5 mm from the heater, and where a temperature profile was applied to the heater (results from this case were shown in Figure 28 through Figure 33). These cases used mesh 8 from Table 5, and a gravity level of 1.0×10^{-4} m/s².

Equation 25 was used to calculate the mass transfer; the accommodation coefficient was set to 0.01. The explicit VOF scheme with first order time discretization was used. The threshold superheat was set to 1K, 2K, and 3K; the results are shown in Figure 37. The pressure rise was very similar for all three cases.

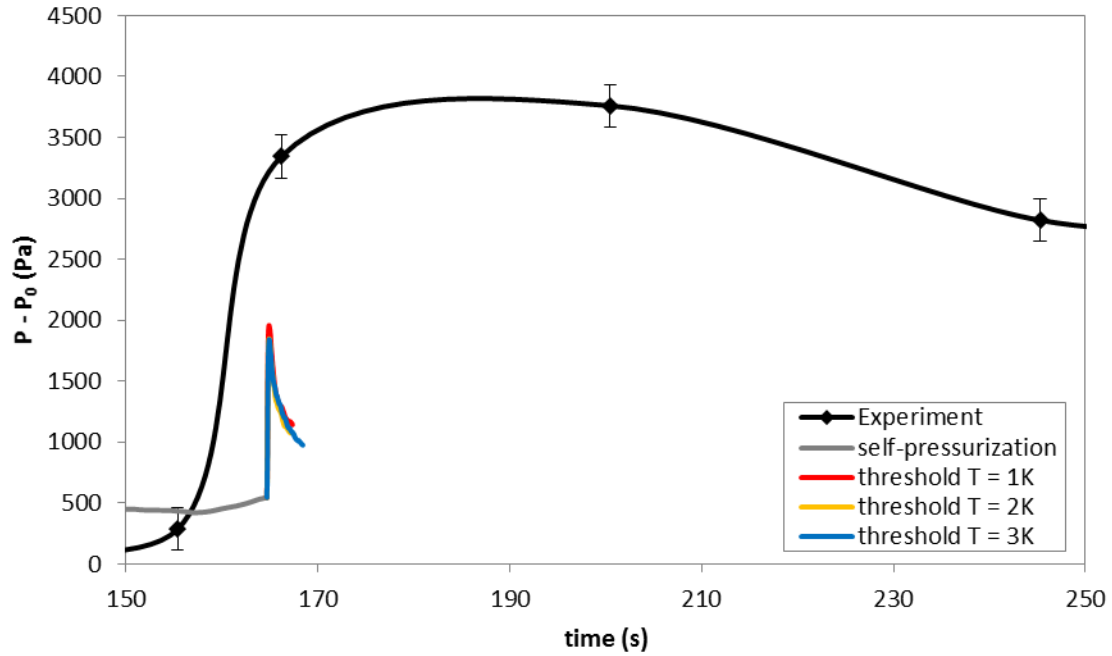


Figure 37: Effect of different threshold superheats required for boiling to occur

Mass Transfer Model 1: Lee Model

During boiling, evaporation and condensation still occur at the interface between the liquid and vapor phases, but evaporation also takes place in the bulk liquid. A temperature profile was applied at the heater. The time at which boiling started was a user-defined parameter. As in the self-pressurization period, the modified Hertz-Knudsen-Schrage equation (Equation 25) was used to calculate the mass transfer at the interface. The Lee model, shown in Equation 26, was used to calculate the mass transfer due to boiling. Boiling was restricted to regions in the bulk liquid with a threshold superheat greater than a user-set value, as shown in Equation 16.

Several cases were run to see the effect of varying the coefficient for the Lee model. The threshold temperature for boiling was set to 1K. The accommodation coefficient used for the Hertz-Knudsen-Schrage equation, which calculated mass transfer at the interface, was set to a value of 0.01. The coefficient for the Lee model was set to various values between 1 and 10; the pressure rises which were calculated using these different coefficients are shown in Figure 38.

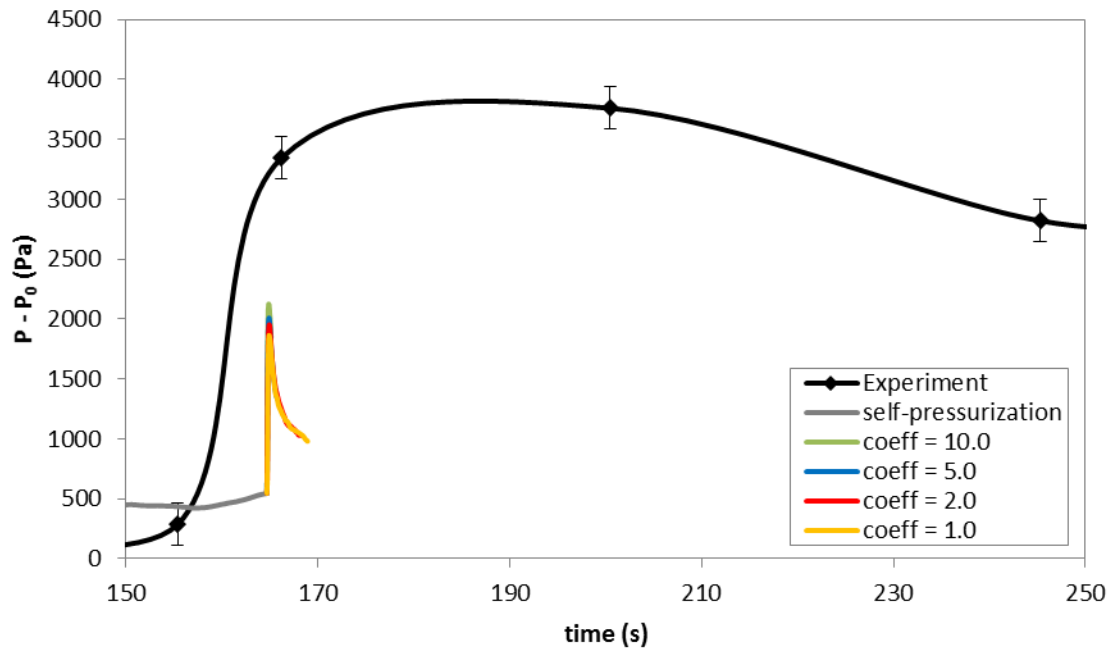


Figure 38: Pressure rise: effect of different values for the Lee model coefficient

Since the pressure rises shown in Figure 38 were not sufficient to match the experiment, a value of 50 was tried for the Lee model coefficient, but the case diverged. A further case was run to see the effect of varying the accommodation coefficient for the Hertz-Knudsen-Schrage equation, which as stated above was used to calculate the mass transfer at the interface. The threshold temperature for boiling was set to 1K. The results are shown in Figure 39; the lower accommodation coefficient for the Schrage equation resulted in a lower overall pressure rise, though the pressure took longer to decay.

The pressure rises seen from these cases were not sufficient to warrant using the Lee model.

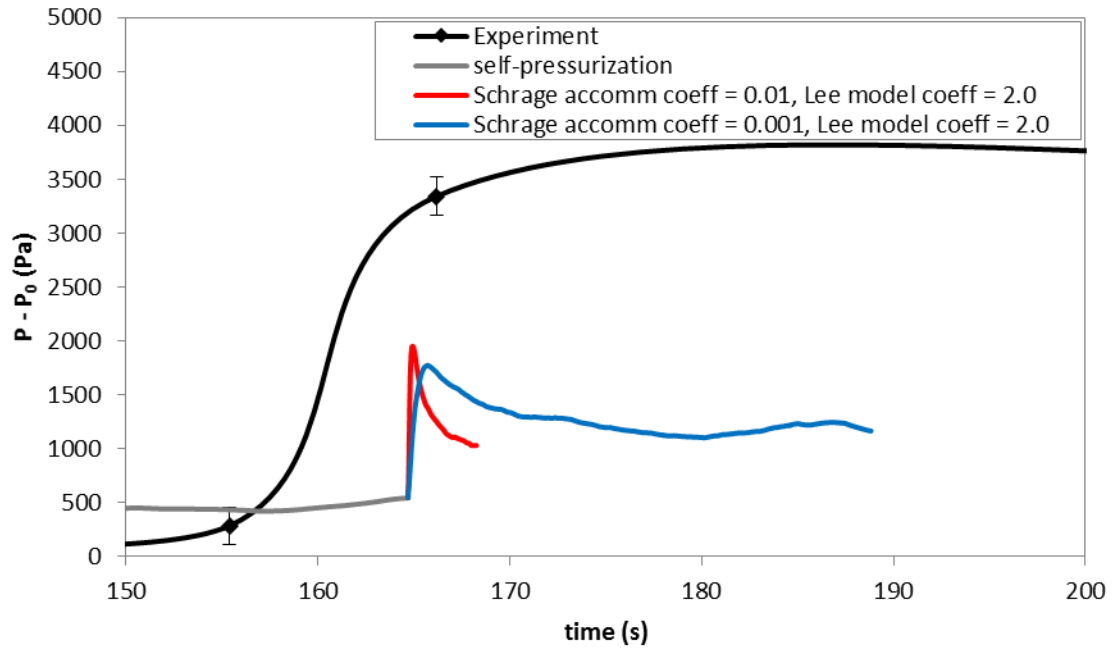


Figure 39: Pressure rise: effect of different Schrage equation accommodation coefficients

Mass Transfer Model 2: Schrage Equation

During boiling, evaporation and condensation still occur at the interface between the liquid and vapor phases, but evaporation also takes place in the bulk liquid. A temperature profile was applied at the heater. The time at which boiling started was a user-defined parameter. Various forms of the Schrage equation were used to calculate the mass transfer due to evaporation, condensation, and boiling.

Several explicit VOF cases were run to see the effect of varying the accommodation coefficient for Equation 25 from $\sigma = 0.00001$ to $\sigma = 0.1$ on the pressure rise; the results are shown in Figure 40. The threshold superheat was set to 3K for these cases.

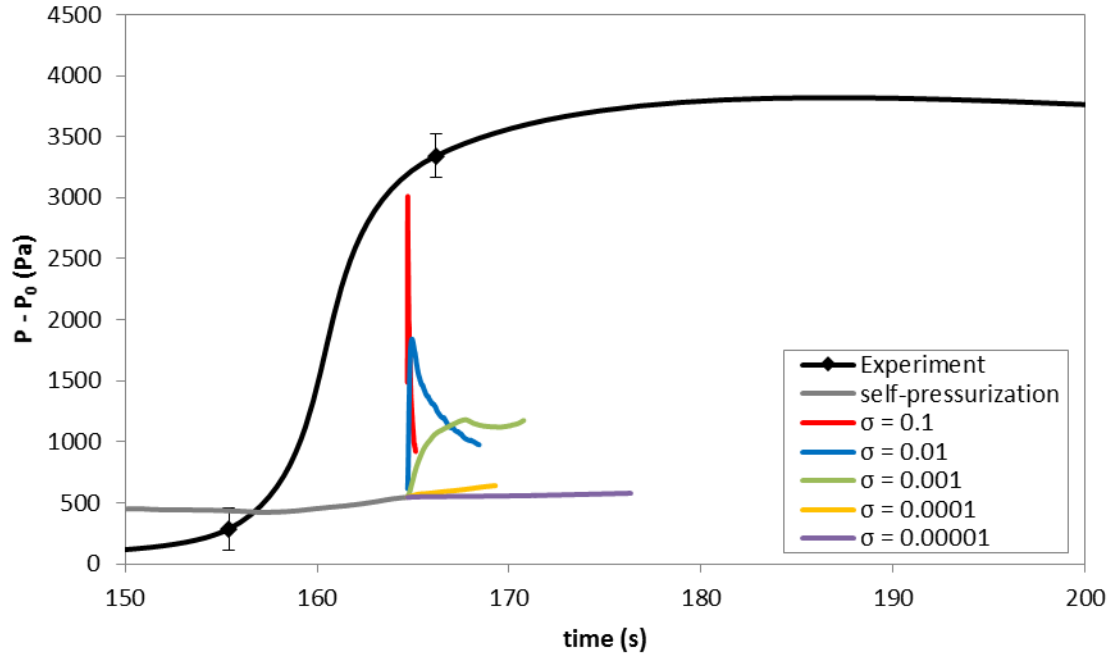


Figure 40: Pressure rise: effect of varying a single accommodation coefficient

The pressure rise with the accommodation coefficient set to $\sigma = 0.1$ seemed close to matching the pressure rise seen in the experiment. However, the decay of this pressure was much faster than that seen in the experiment.

Equation 25 assumes that the evaporation and condensation coefficients are equal to each other (Marek & Straub, 2001), (Sharma, 2006). This assumption is valid under equilibrium or near-equilibrium conditions (Cipolla Jr. , Lang, & Loyalka, 1974). However, since noncondensable gases were present in the experiment, the interface was not in an equilibrium condition. Hasan et al. (1996) assumed that, since the mass fraction of the noncondensable gases was 0.5 to 2%, they would not affect the rate of vapor condensation, but according to Barrett and Clement (1992), this is not necessarily true. Noncondensable gases reduce the condensation coefficient, but have no effect on the evaporation coefficient. This is due to the fact that, as condensation occurs, a layer of noncondensable gas builds up by the interface, impeding further condensation.

In order to capture this effect, several further explicit VOF cases were run using Equation 22 to calculate the mass transfer; these cases used two different values for the accommodation coefficient, one for condensation at the interface (σ_c), and a second for evaporation at the interface (σ_e) and boiling in the bulk liquid (σ_b). The magnitude of the accommodation coefficient used for evaporation and boiling was based on the results shown in Figure 40, while the condensation coefficient was varied in an attempt to slow the decay of the pressure in the tank. The threshold superheat was set to 3K for these cases. The results are shown in Figure 41; the case with a single accommodation coefficient of $\sigma = 0.1$ is shown using a dashed line for comparison.

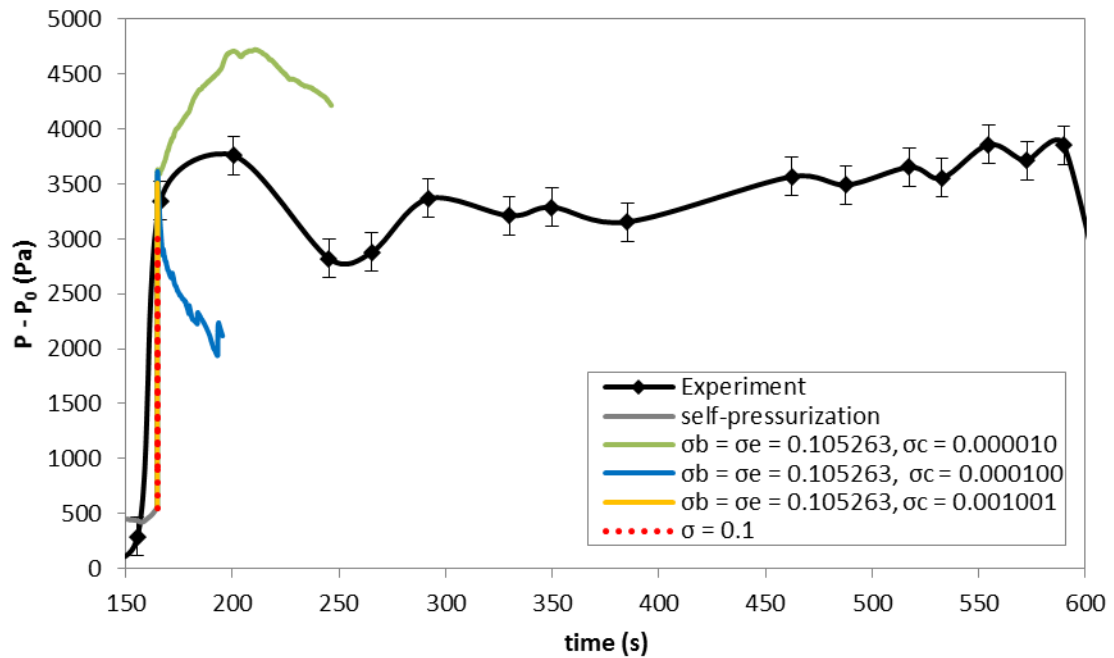


Figure 41: Pressure rise: different accommodation coefficients used for evaporation and condensation

The pressure rise in the cases shown in Figure 41 was much closer to that of the experiment. However, only the case with the accommodation coefficients set to $\sigma_b = \sigma_e =$

0.1 and $\sigma_c = 0.00001$ came close to matching the rate of the pressure decay; unfortunately, it overshoot the amount of pressure rise seen in the experiment.

Since boiling is not an equilibrium condition, the accommodation coefficients used for evaporation at the interface and boiling in the bulk liquid do not need to be equal to each other. Therefore, further explicit VOF cases were run using Equation 22 to calculate the mass transfer due to evaporation, boiling, and condensation separately. Based on the previous results, the accommodation coefficient for boiling was set to $\sigma_b = 0.1$, and the accommodation coefficient for condensation was set to $\sigma_c = 0.00001$. The accommodation coefficient for evaporation at the interface, σ_e , was varied. The threshold superheat was set to 3K. The results of these cases are shown in Figure 42; the results of the case with the accommodation coefficients set to $\sigma_e = \sigma_b = 0.1$ and $\sigma_c = 0.00001$ are shown using a dashed line for comparison.

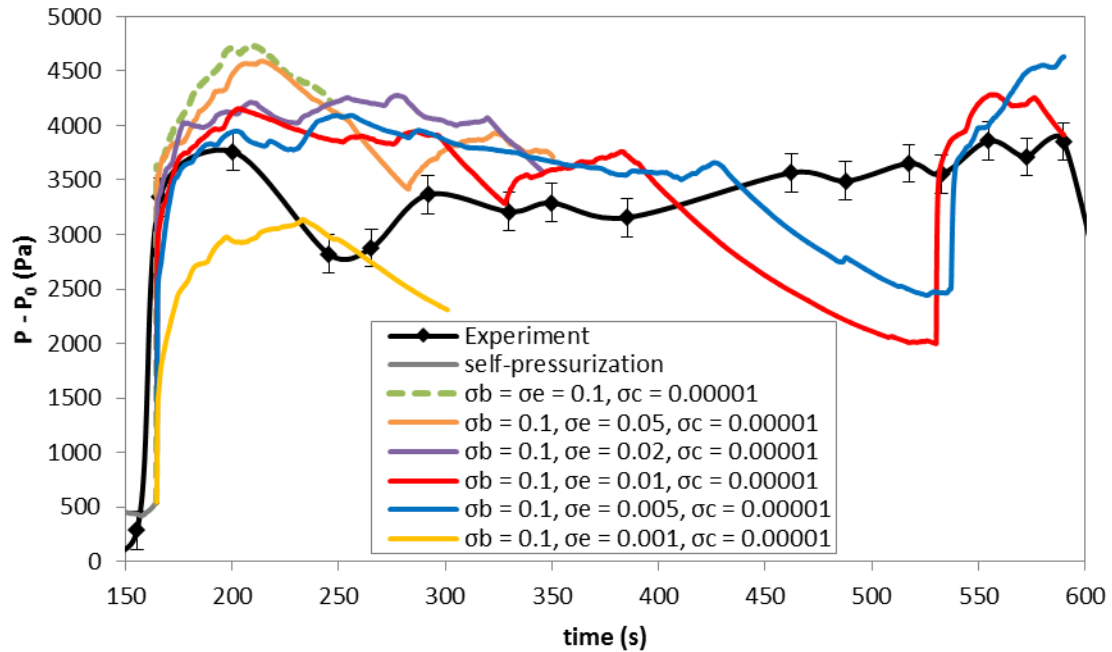


Figure 42: Pressure rise: different accommodation coefficients used for boiling, evaporation, and condensation

Several more explicit VOF cases were run to see the effect of varying σ_c on the pressure. The accommodation coefficients for these cases were set to $\sigma_b = 0.1$ and $\sigma_e = 0.01$. The threshold superheat was set to 3K for all of these cases. The results are shown in Figure 43.

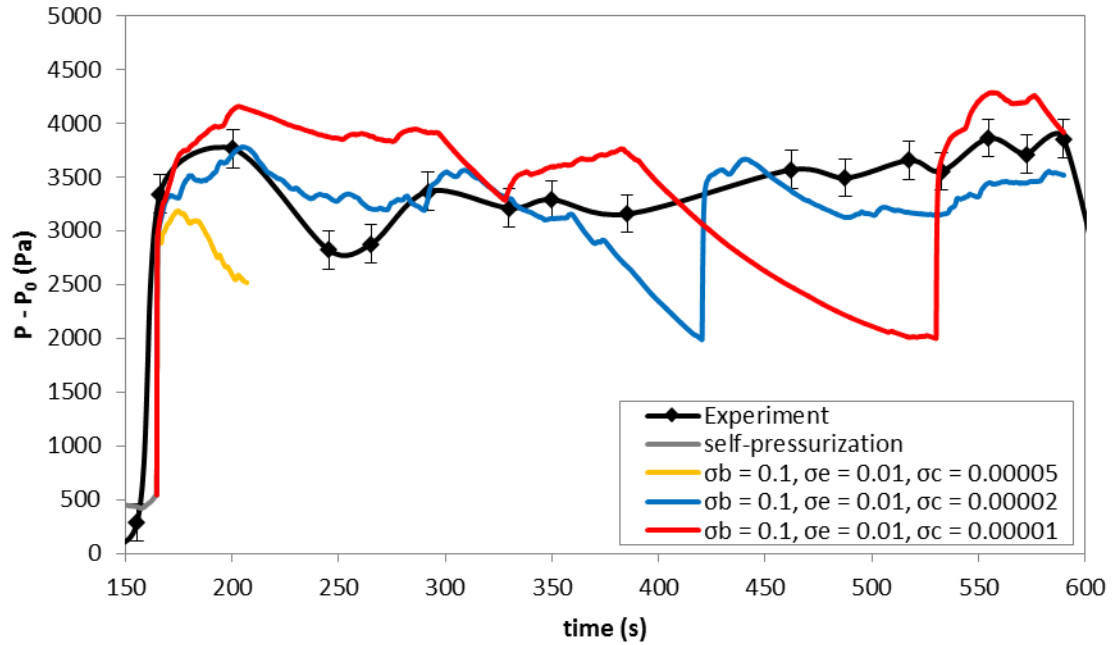


Figure 43: Pressure rise: three different accommodation coefficients: effect of varying condensation accommodation coefficient

All of the previous cases used the explicit VOF model, with first-order time discretization. These cases followed the pressure curve of the experiment only roughly; they displayed a tendency to drop in pressure below the level of the experiment, and then return to a higher pressure value. In an attempt to correct this, a few further cases were run using the implicit VOF model, with bounded second-order time discretization. All of these cases used the accommodation coefficients from the best explicit VOF case: $\sigma_b = 0.1$, $\sigma_e = 0.005$, and $\sigma_c = 0.000001$. The threshold superheat was set to 3K for these cases. The results are shown in Figure 44.

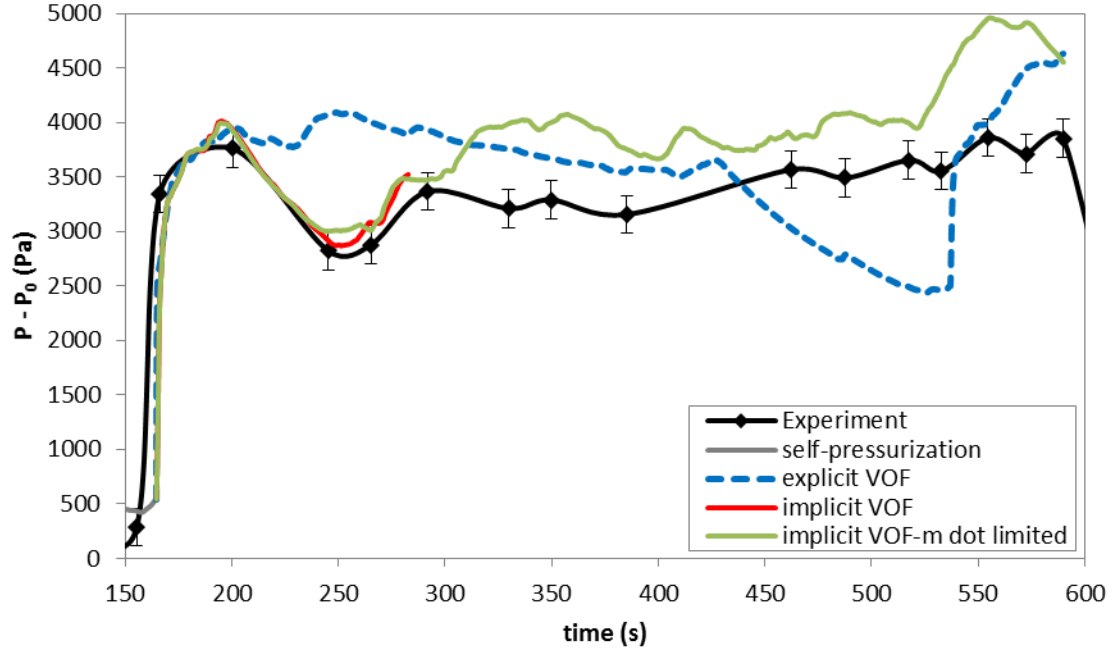


Figure 44: Boiling using the implicit VOF scheme, with bounded second order time discretization

For one of the implicit VOF cases in Figure 44, the maximum mass transfer in each cell was limited to the mass in that cell in each time step; this limit was calculated using Equation 17. Although limiting the maximum mass transfer did not have much effect in this case, it might in other cases, so all further cases were run with this limit. The effect of the pressure-velocity coupling scheme was examined in a further case, which used the coupling scheme; all of the preceding cases had been run using the PISO pressure-velocity coupling scheme. The threshold superheat was set to 3K. The results are shown in Figure 45.

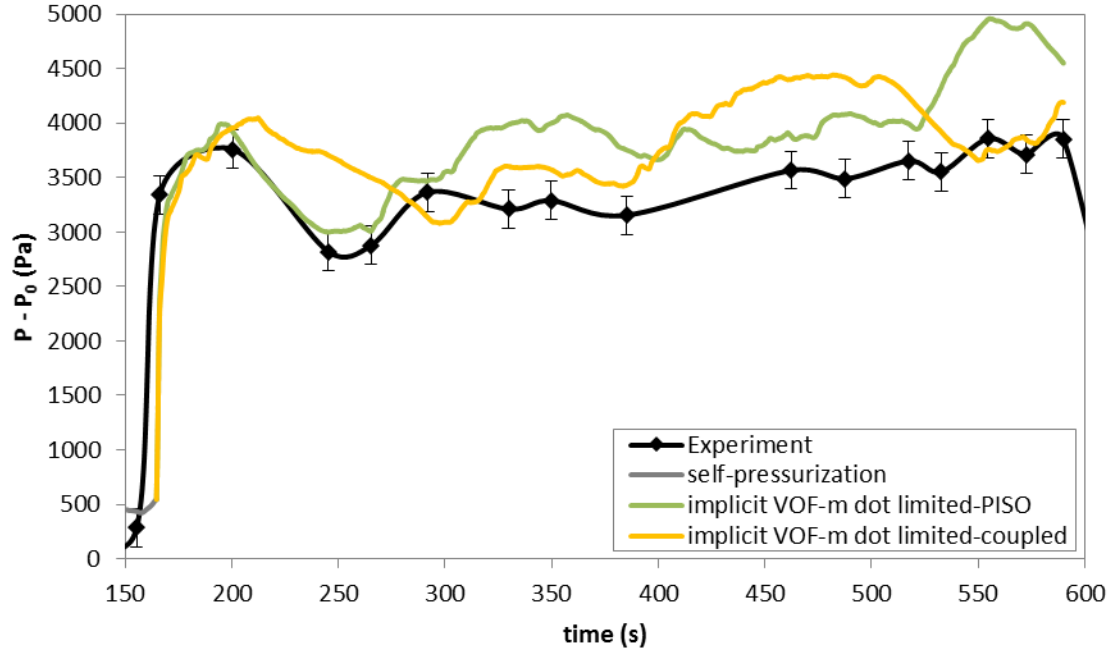


Figure 45: Comparison between the PISO and coupled schemes for pressure-velocity coupling

Based on the results of several preliminary boiling cases where the threshold temperature was varied from 1K to 3K, as shown in Figure 37, the threshold temperature was not considered to have much impact on the results. Therefore, all of the preceding boiling cases have used a threshold temperature of 3K. A further case was run to see the effect of changing the threshold temperature from 3K to 1K with the implicit VOF model; the results are shown in Figure 46. The PISO pressure-velocity coupling scheme was used for these cases.

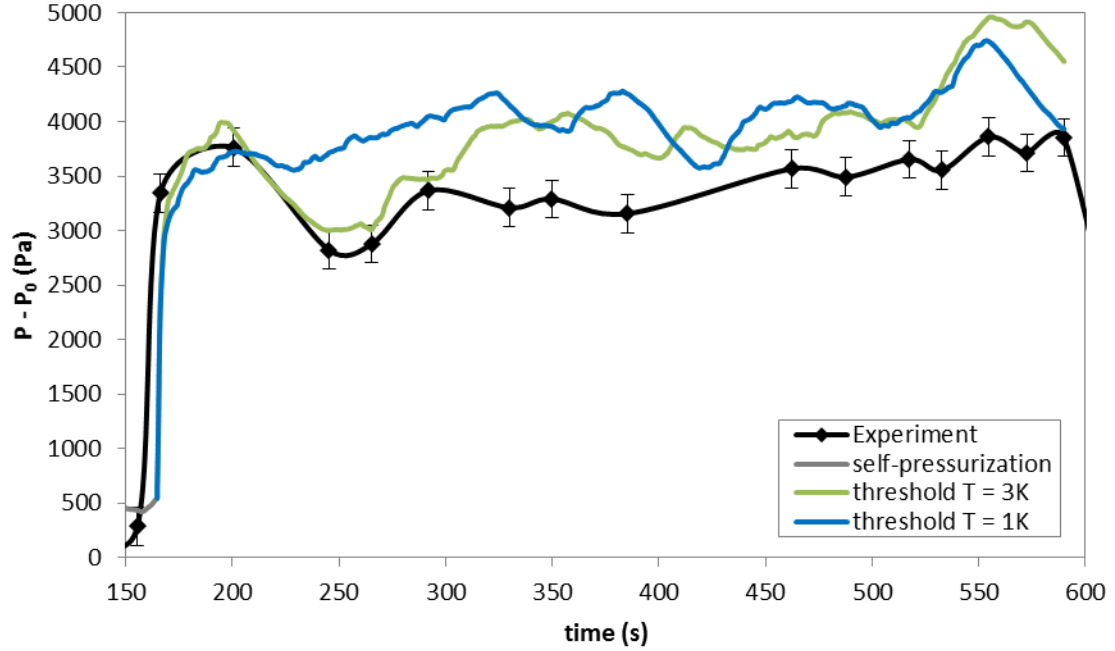


Figure 46: Effect of varying the threshold temperature for boiling

A comparison of the pressure curves from the four best boiling cases is shown in Figure 47. These cases all used accommodation coefficients of $\sigma_b = 0.1$, $\sigma_e = 0.005$, and $\sigma_c = 0.00001$. One case used the explicit VOF model, while the other three used the implicit VOF model. The implicit VOF cases used the PISO pressure-velocity coupling scheme, with threshold temperatures of 3K and 1K, and the coupled scheme with a threshold temperature of 3K. The temperatures predicted by the model at each of the thermistors are also shown, in Figure 48 through Figure 52. Since the exact locations of the thermistors in the experiment are unknown, the behaviors of the temperature curves can only be compared qualitatively against the experimental data. (The locations of each of these thermistors in the axisymmetric case are shown in Figure 15.) The vertical dashed lines in Figure 47 show the times at which temperature contour plots were taken from each case; these contour plots are shown in Figure 53 through Figure 56. The interface is shown using black lines at isocontours of the volume fraction of vapor of 0.5.

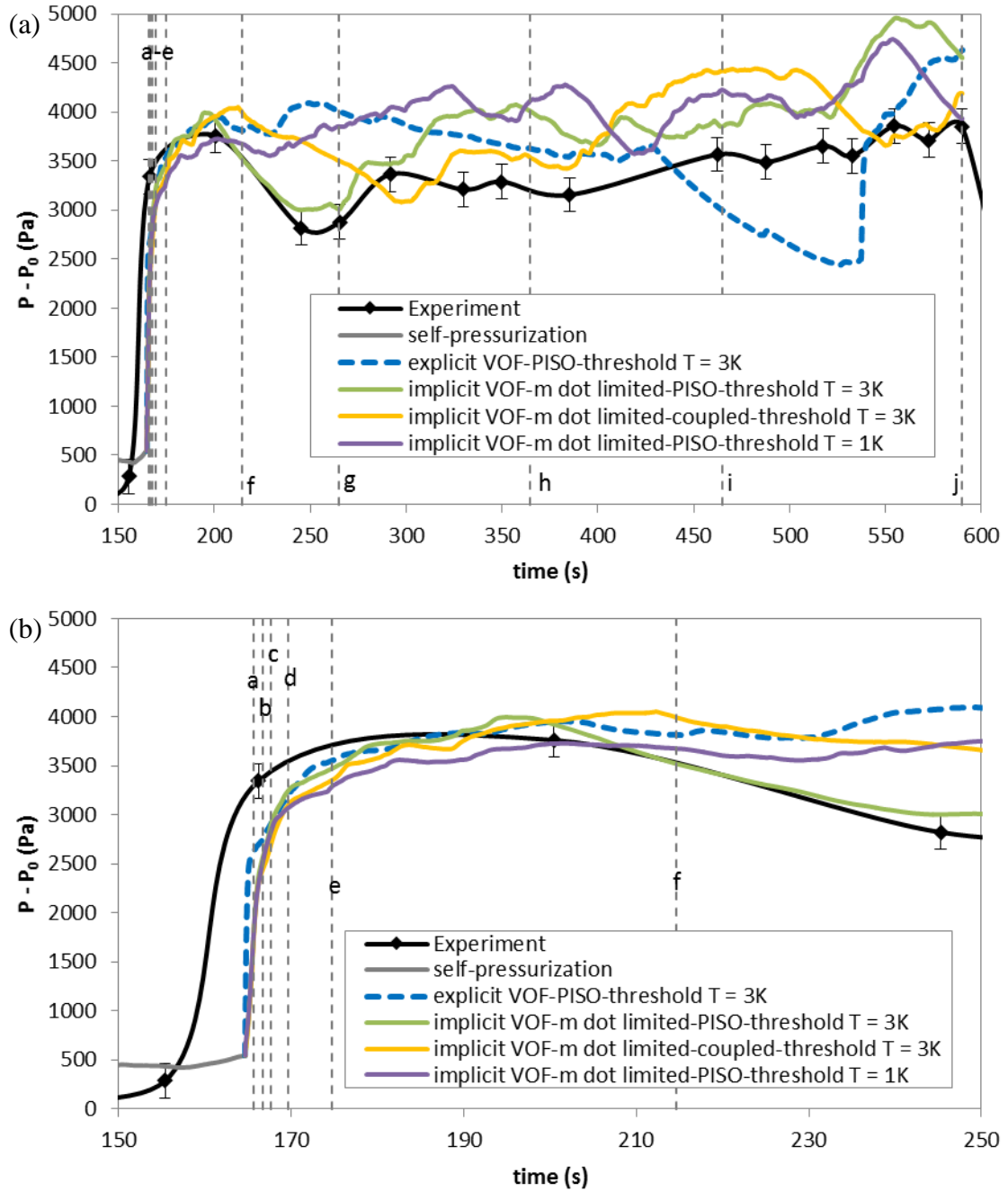


Figure 47: Pressure curves from the four best boiling cases (dashed vertical lines are to show the times at which temperature contour plots were taken from the simulations), (a) entire boiling period, (b) beginning of the boiling period

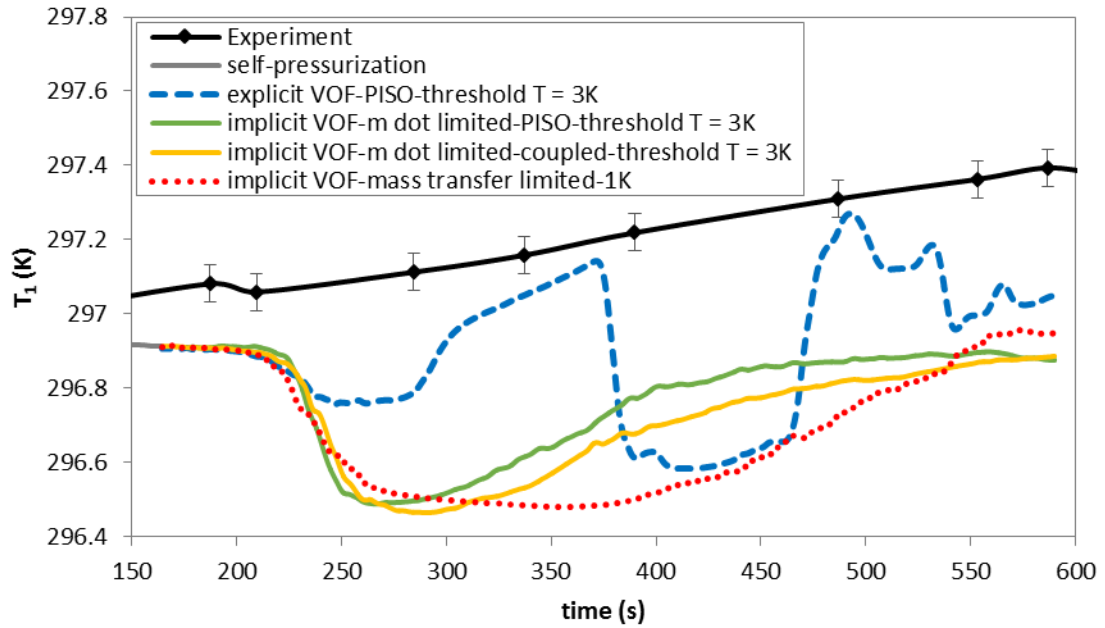


Figure 48: Temperature at T1 during the four best boiling cases

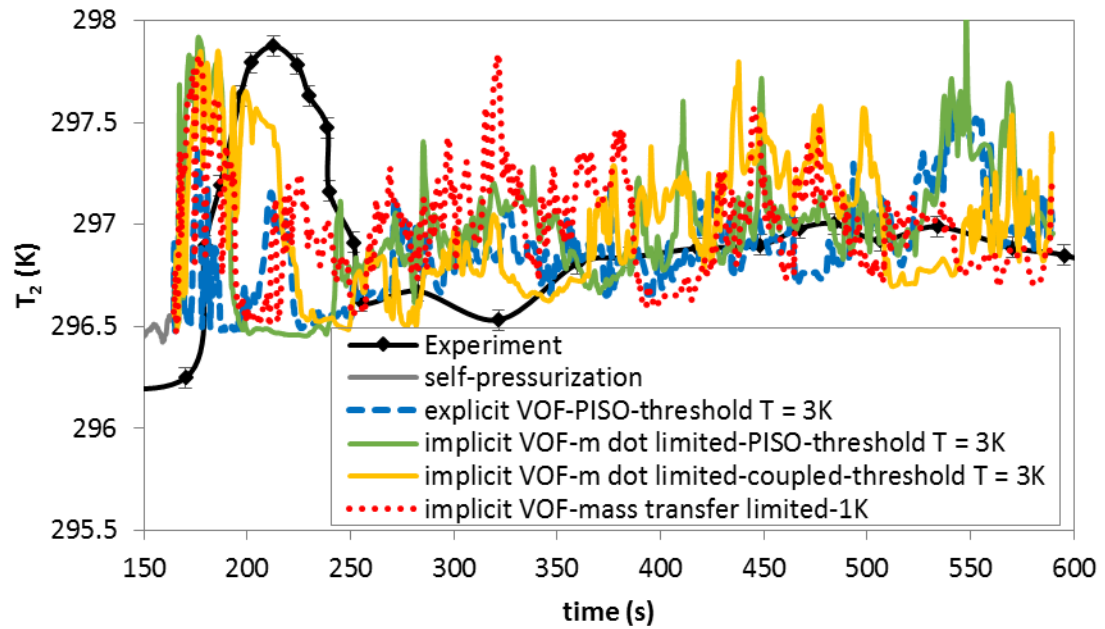


Figure 49: Temperature at T2 during the four best boiling cases

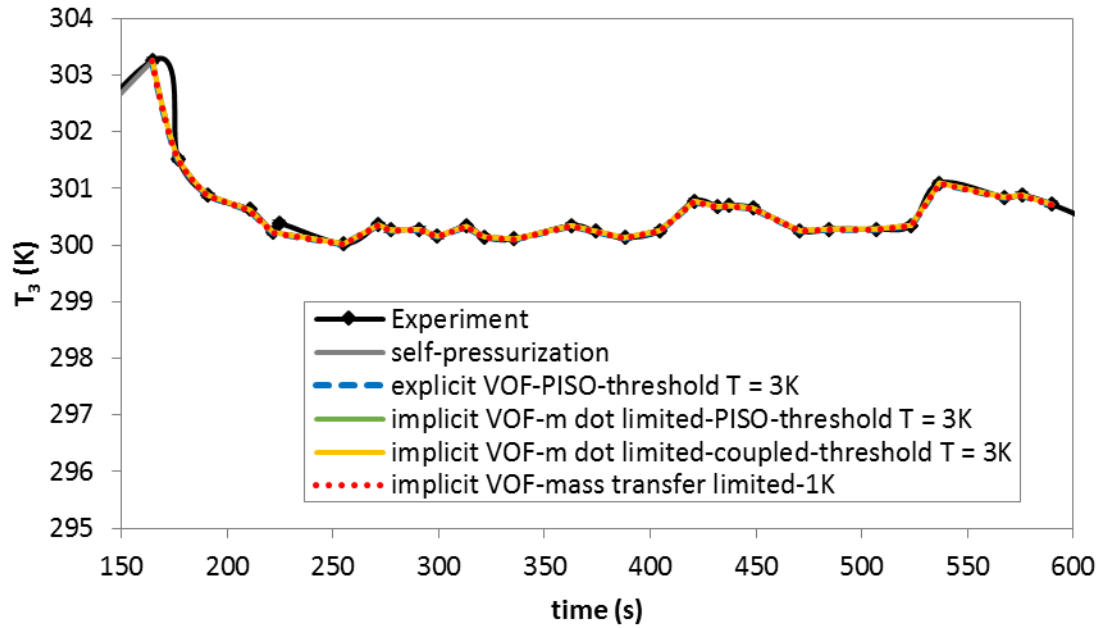


Figure 50: Temperature at T3 during the four best boiling cases

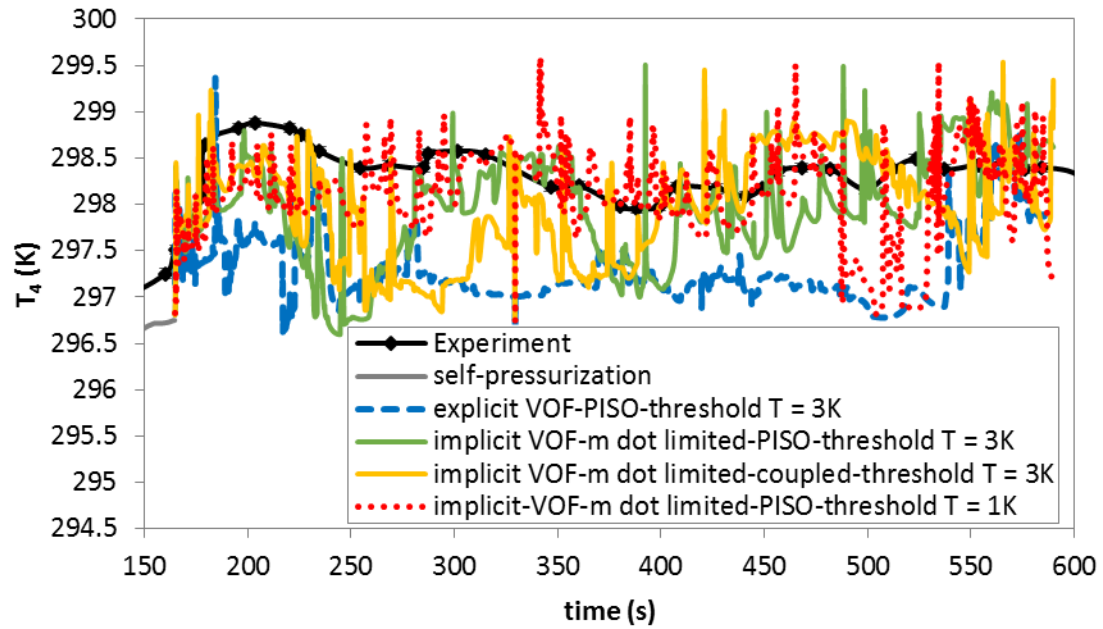


Figure 51: Temperature at T4 during the four best boiling cases

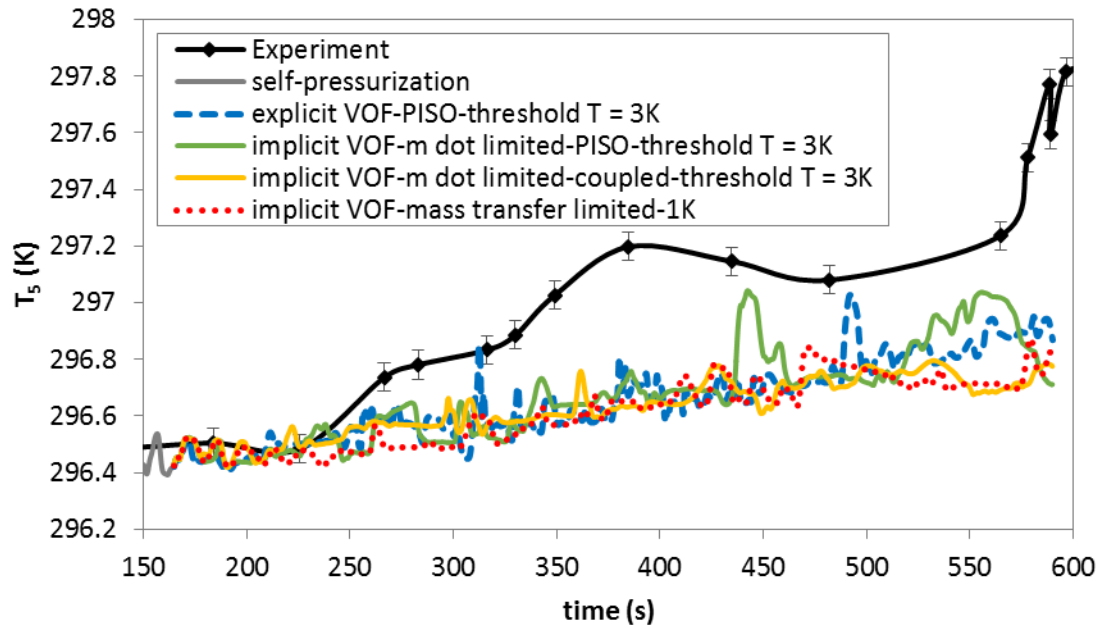
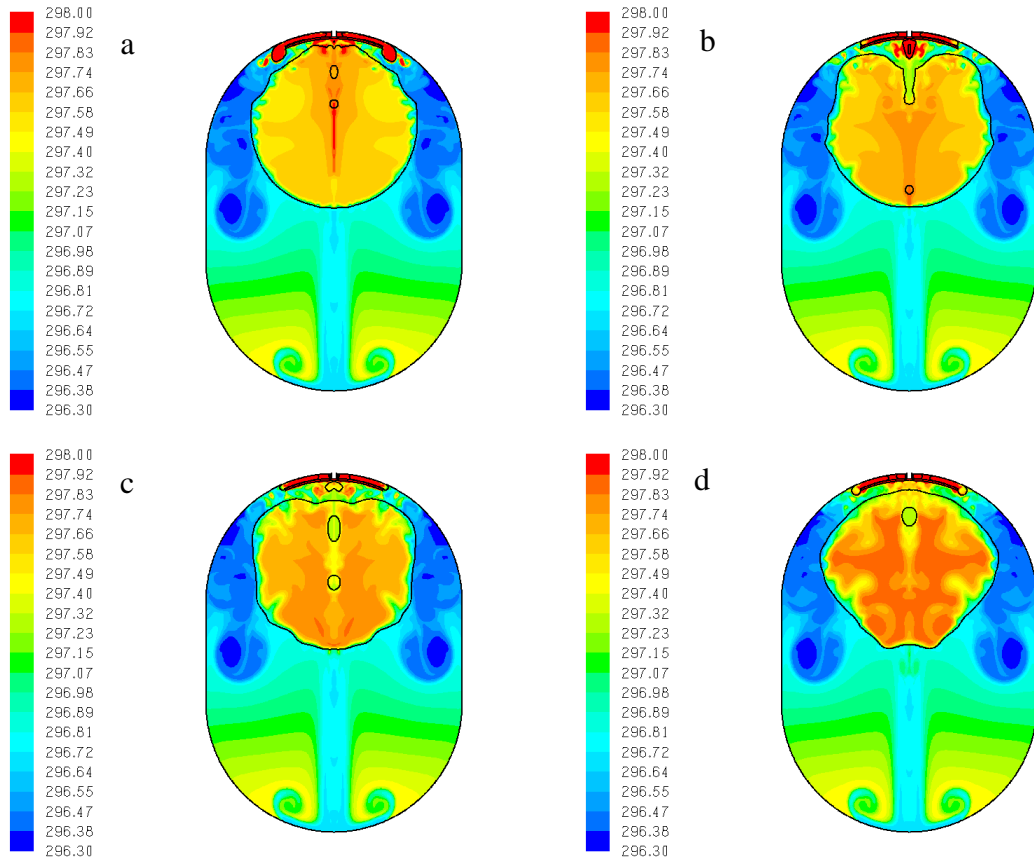


Figure 52: Temperature at T5 during the four best boiling cases



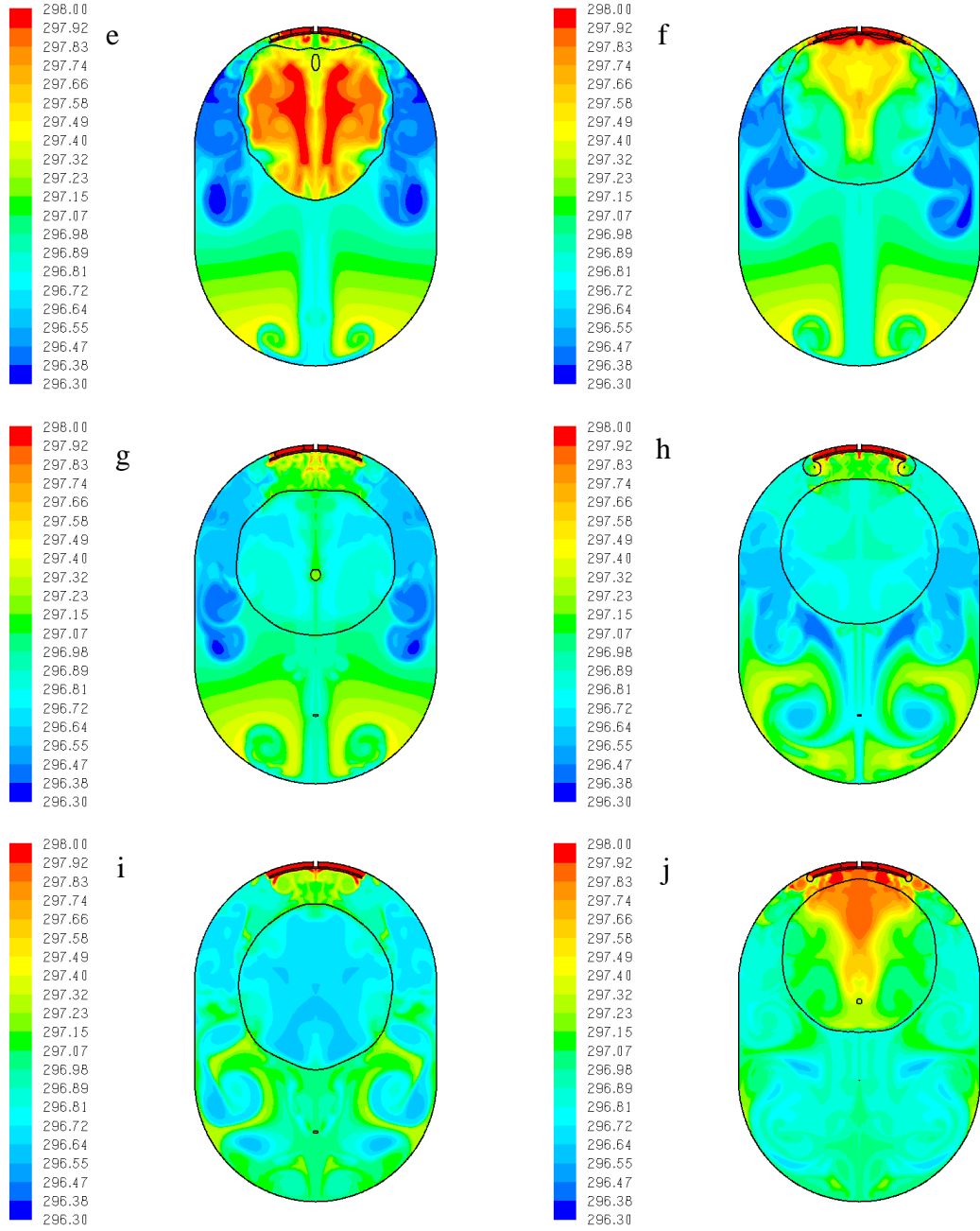
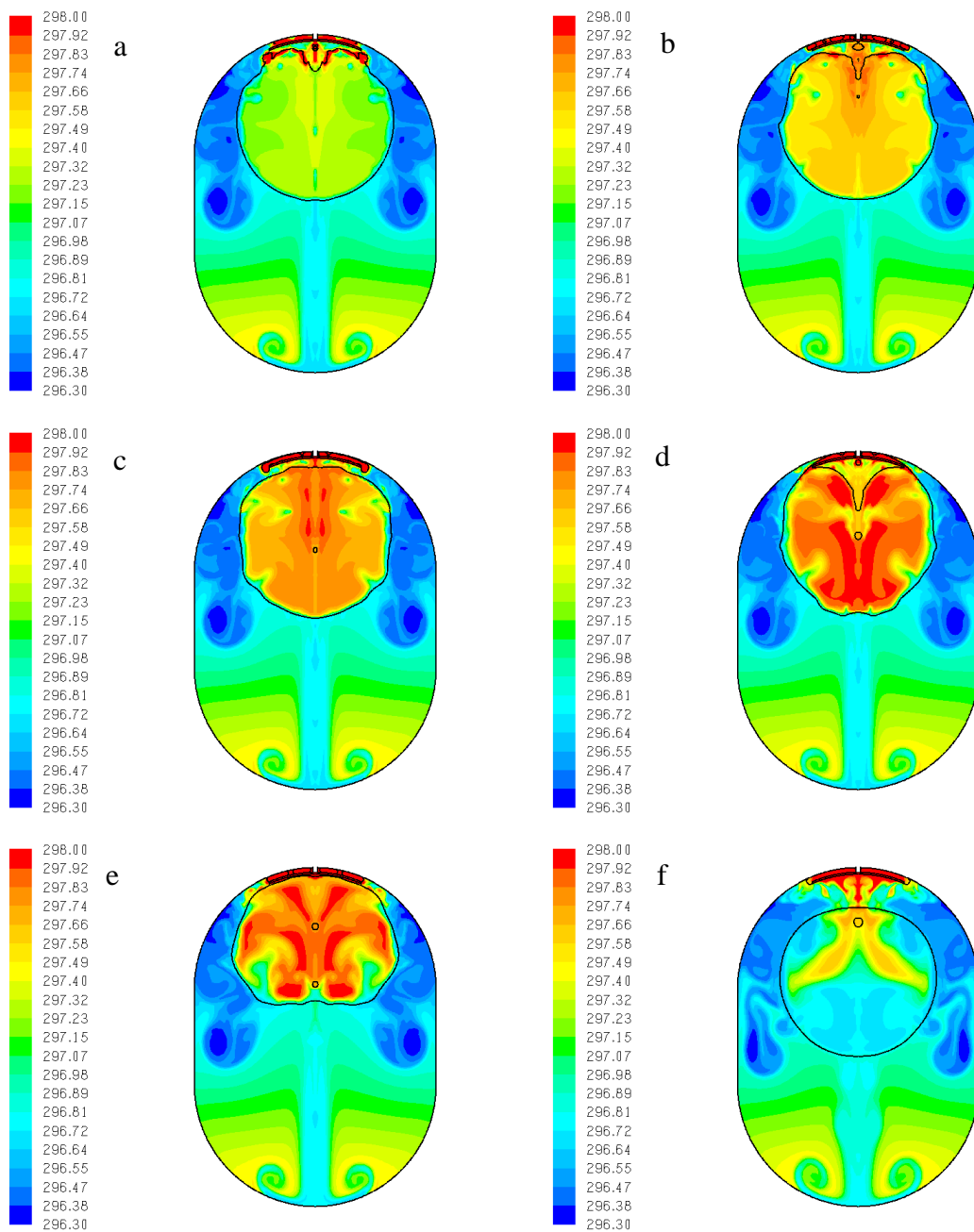


Figure 53: Temperature contour plots for the explicit VOF case using PISO and a threshold temperature of 3K



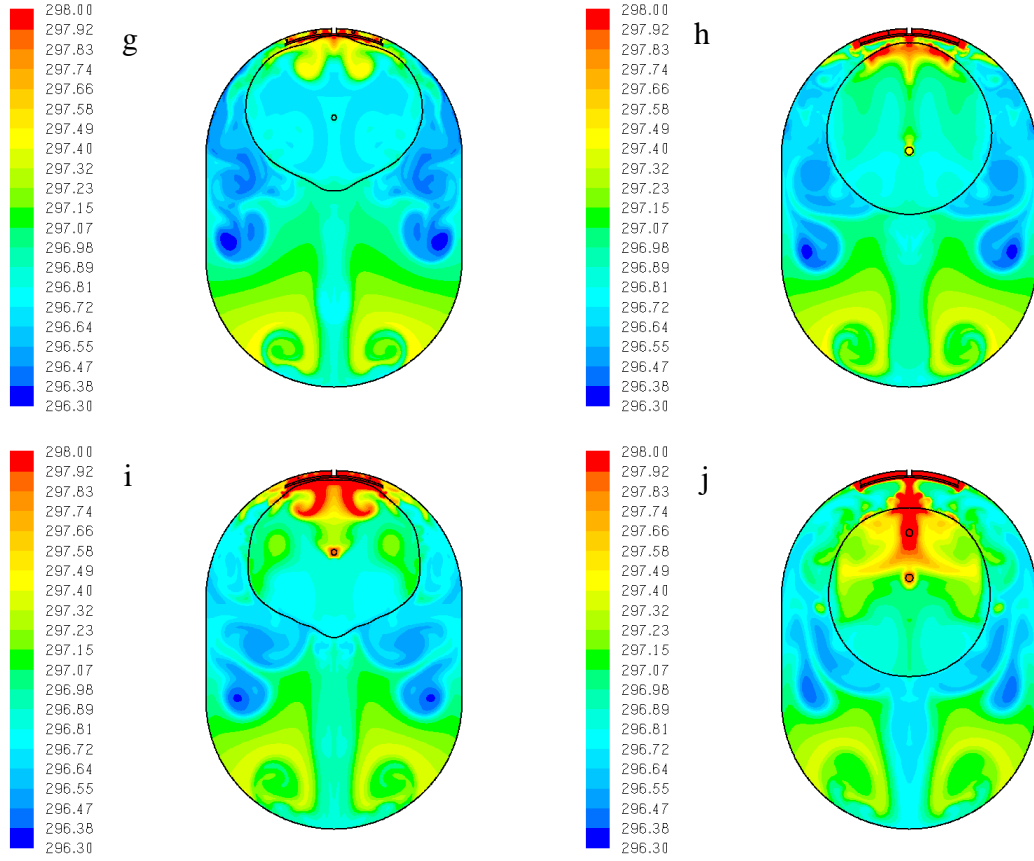
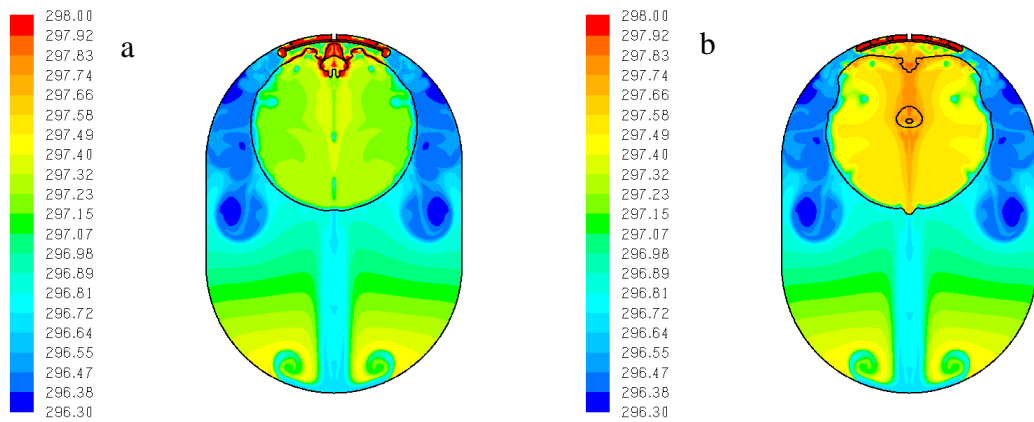
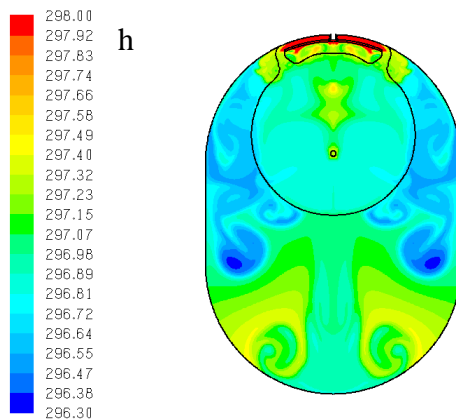
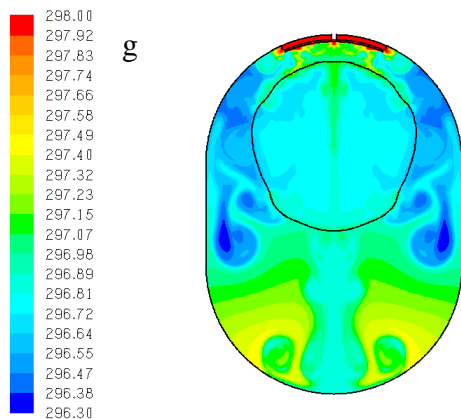
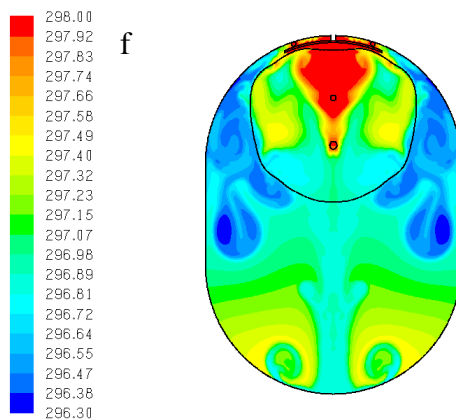
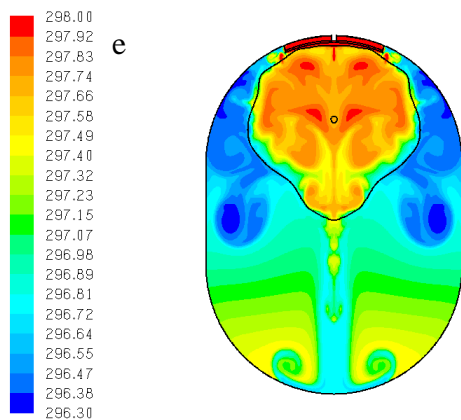
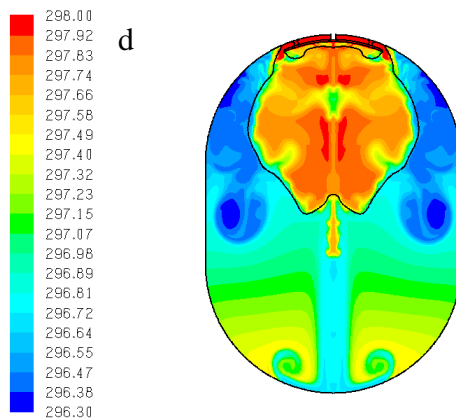
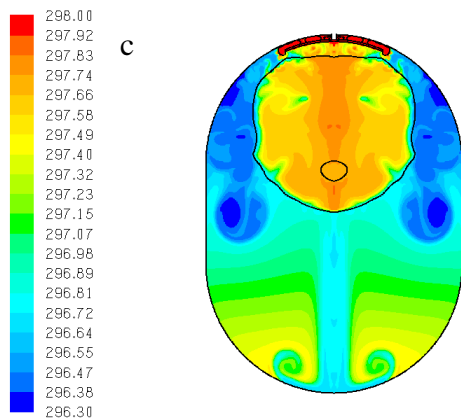


Figure 54: Temperature contour plots for the implicit VOF case using PISO and a threshold temperature of 3K





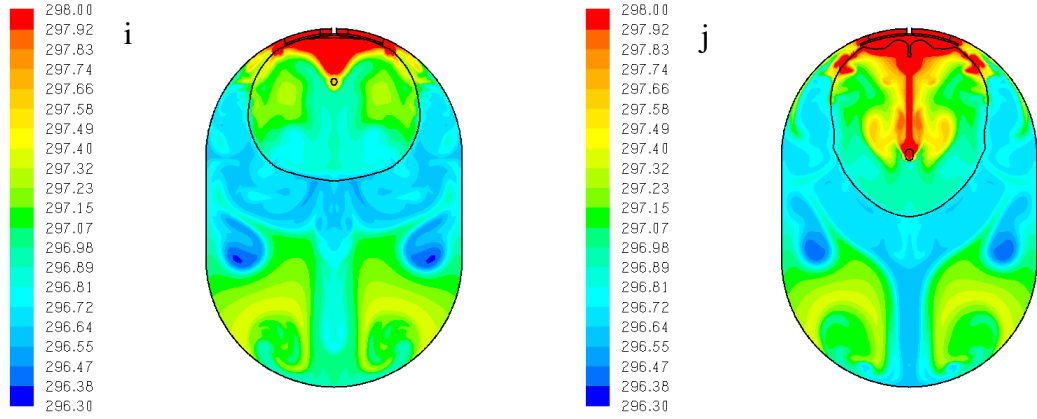
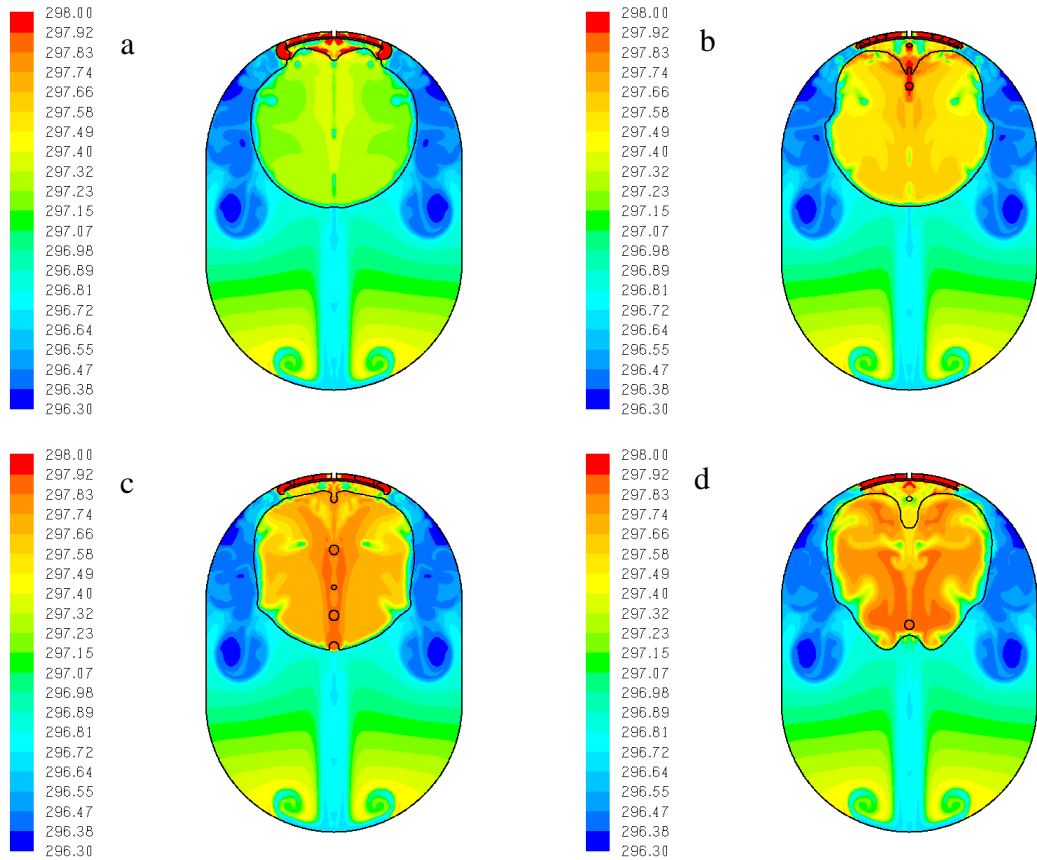


Figure 55: Temperature contour plots for the implicit VOF case using the coupled pressure-velocity coupling scheme and a threshold temperature of 3K



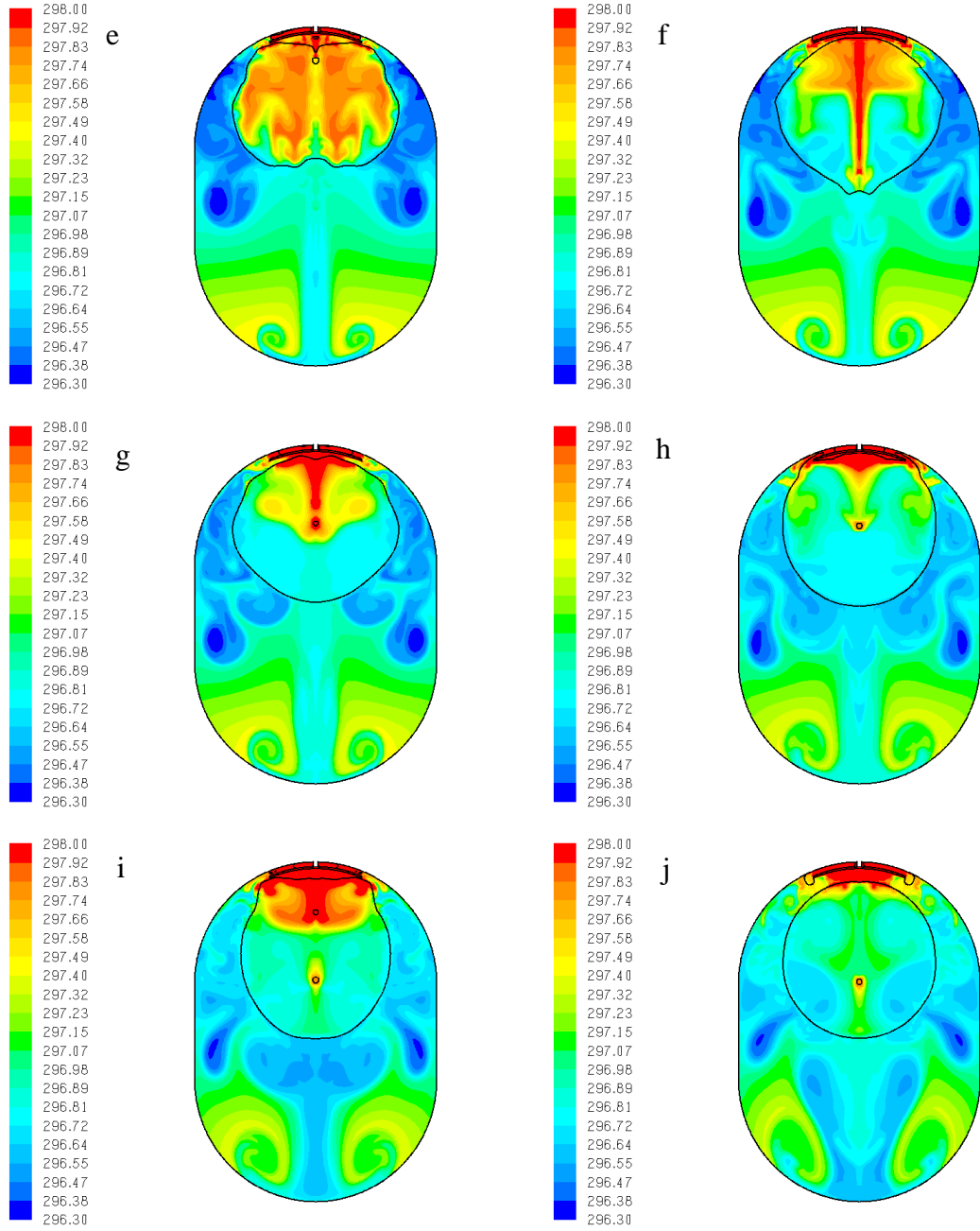


Figure 56: Temperature contour plots for the implicit VOF case using PISO and a threshold temperature of 1K

Figure 47 shows that the pressure predicted by the models agrees well with the experiment; the implicit VOF model is better than the explicit VOF model. The temperatures at the thermistor locations mostly agree with the temperatures measured during the experiment, as shown by Figure 48 through Figure 52.

In Figure 53 through Figure 56, it can be seen that liquid droplets are contained within the ullage. Some of these droplets are spurious, a result of the VOF model not correctly resolving the velocities and volume fractions at the axis. However, some of these liquid droplets are not spurious. As the bubbles forming around the heater joined the ullage, the ullage deformed, and liquid droplets moved through the ullage. This behavior is similar to the behavior of the experiment during boiling, as shown by the images in Figure 12.

Final Boiling Model

The best model used the implicit VOF model with bounded second order time discretization. The compressive scheme was used for the volume fraction. The Schrage equation was used to calculate the mass transfer due to evaporation and condensation at the interface, as well as boiling. The accommodation coefficients for the Schrage equation were set to $\sigma_b = 0.1$, $\sigma_e = 0.005$, and $\sigma_c = 0.00001$. Although the PISO and coupled pressure-velocity coupling schemes produced pressure curves that were similar to each other, the PISO scheme was slightly more stable. The pressure curve calculated using this model is shown in Figure 57. Figure 54 shows temperature and volume fraction contours in the tank at various times for this case.

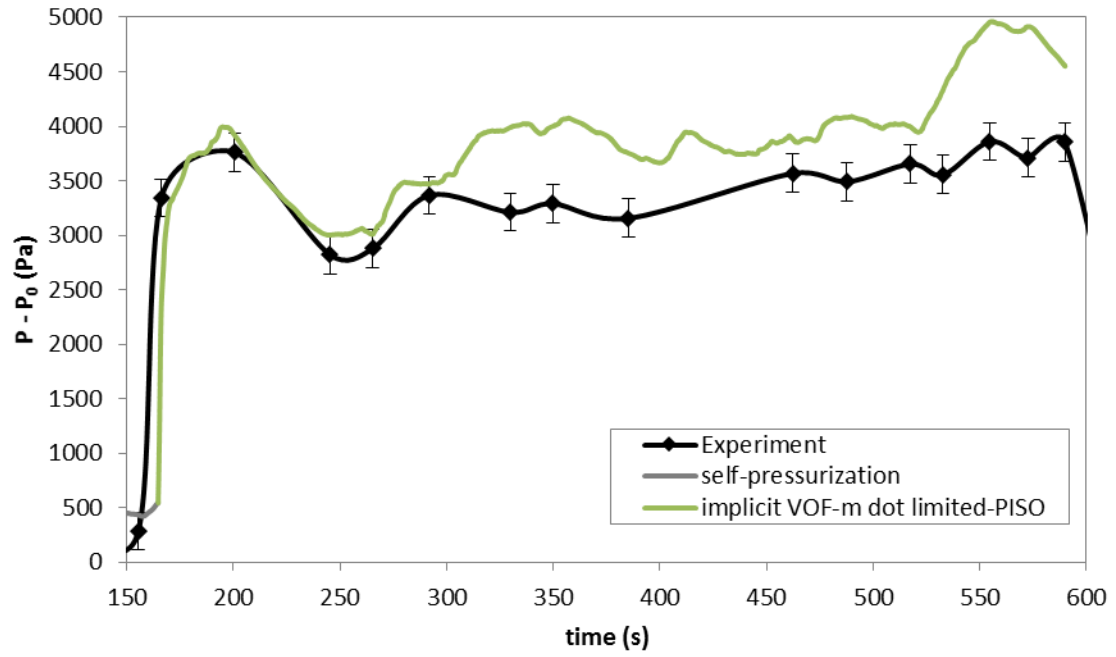


Figure 57: Pressure curve calculated using the best boiling model

CHAPTER VII

SUMMARY AND CONCLUSION

Summary of Work Performed

The goal of this study was to create an engineering model of the pressure rise in a tank due to boiling. A two-phase compressible VOF CFD model was used to model boiling in a tank. (The VOF model (ANSYS, 2013a) captures the interface and its motion in a diffuse manner by tracking the volume fraction of each fluid (Kartuzova & Kassemi, 2011).) The heater temperature was applied as a boundary condition. The time at which boiling started was a user-defined parameter. The mass transfer at the interface was calculated using the Schrage equation, while the mass transfer due to boiling was calculated using either the Schrage equation or the Lee model. This model was validated against microgravity data provided by the Tank Pressure Control Experiment: Thermal Phenomena in Microgravity, which was flown on the space shuttle mission STS-52 (Hasan, Lin, Knoll, & Bentz, 1996).

It was decided to model the tank as being axisymmetric. Although boiling is a 3D phenomenon, it has been modeled using axisymmetric models with acceptable success (Son, Dhir, & Ramanujapu, 1999), (Son, Ramanujapu, & Dhir, 2002), (Son & Dhir, 2008). Additionally, the computational efficiency of axisymmetric models allowed many

parameters to be studied. Some of the physical characteristics of the tank (Bentz, 1993), (Hasan, Lin, Knoll, & Bentz, 1996) were not very axisymmetric, most notably the heater and the tank walls. Therefore, the tank was simplified to make it more axisymmetric by altering the shape of the heater to a circular disk with the same area and curvature as in the experiment, and by neglecting the tank walls and heater B.

Several important boundary and initial conditions were not recorded for the experiment, including the temperature outside the tank. Because of this, the predictions made by the model could only be compared to the general trends of the experimental data.

The acceleration due to gravity which was experienced by the experiment was estimated as being on the order of 10^{-6} m/s^2 (Bentz, 1993); however, spurious velocities created in the VOF model overwhelmed the effects of gravity at this level, so the acceleration due to gravity was increased in the model to 10^{-4} m/s^2 . The Grashof number indicated that the tank was laminar.

The locations of the thermistors were not provided with enough detail to locate them accurately inside the tank. Instead, their positions were estimated based on the dimensions that were provided, and on the schematic provided by Bentz (1993). Because of this, the temperatures predicted by the model were only compared qualitatively to the temperatures measured during the experiment, to see if they were behaving in a similar manner. The pressure curve was used as the criterion for determining whether the model matched the experimental results.

For the model, the time the heater was on was divided into two periods, the self-pressurization period and the boiling period. During the self-pressurization period, the explicit VOF scheme with first order time discretization was used. Since the self-

pressurization period was assumed to be in a near-equilibrium condition, the Hertz-Knudsen-Schrage equation (Marek & Straub, 2001), which assumes that the evaporation and condensation coefficients are equal to each other, was used to model the mass transfer. The boiling cases were started from the end of the self-pressurization case.

During the boiling period, both the explicit VOF scheme with first order time discretization, and the implicit VOF scheme with bounded second order time discretization, were used. The Schrage equation was used to calculate the mass transfer at the interface. Two different models were used to simulate mass transfer due to boiling, the Schrage equation (Schrage, 1953), (Marek & Straub, 2001) and the Lee model (ANSYS, 2013a).

The Lee model, run using the explicit VOF scheme, did not produce results which matched the experiment well. The initial explicit VOF boiling cases that were run using the Schrage equation used the same accommodation coefficient for evaporation and condensation at the interface, as well as for boiling in the bulk liquid. The evaporation and condensation coefficients are equal to each other in equilibrium conditions (Cipolla Jr. , Lang, & Loyalka, 1974); however, boiling is not an equilibrium condition. Additionally, noncondensable gases were present in the experiment, causing the interface to not be at an equilibrium condition, either. Therefore, there is no reason to assume the accommodation coefficients are equal to each other. The explicit VOF cases which used the same accommodation coefficient for evaporation and boiling, and a separate one for condensation, did not match the experiment well. However, the explicit VOF cases which used a different accommodation coefficient each for evaporation, boiling, and condensation did match the experiment fairly well. The values of the accommodation coefficient were tuned to try to better match the results; the result was that the pressure rose

quickly to about the level shown by the experiment at the start of boiling, and remained roughly at that level during the boiling period. However, the pressure later dropped farther than was shown in the experiment during several cases.

These cases all used the explicit VOF scheme with first order time discretization. Further cases were run using the implicit VOF scheme with bounded second order time discretization, using the accommodation coefficients that gave the best results for the previous cases.

When the implicit VOF scheme was used with bounded second order time discretization, the pressure followed the experimental trend more accurately. The two pressure-velocity coupling schemes that were tried showed similar results, although the case that used PISO was somewhat more stable than the case that used the coupled scheme. Changing the threshold temperature at which boiling was allowed to occur also did not have much effect on the pressure.

The final model used the implicit VOF scheme with bounded second order time discretization. The Schrage equation was used to calculate the mass transfer, with separate accommodation coefficients for each of the three different mass transfer mechanisms: evaporation and condensation at the interface, and boiling in the bulk liquid.

A brief summary of the work that was performed is shown in Table 8.

Table 8: Summary of Work Performed

Mesh independence study	1208 elements to 38141 elements, in different configurations
Time step independence study	Without phase change: $1 \cdot 10^{-4}$ s to $1 \cdot 10^{-2}$ s With phase change at the interface: $1 \cdot 10^{-3}$ s, $5 \cdot 10^{-4}$ s, $1 \cdot 10^{-4}$ s

	With phase change at the interface and boiling: 5×10^{-4} s, 1×10^{-4} s, 5×10^{-5} s
Gravity study	1×10^{-6} m/s ² , 1×10^{-5} m/s ² , 1×10^{-4} m/s ²
Initial conditions	Temperature profile: Uniform, Linear profile Ullage location at the start of self-pressurization: 5mm from the heater, 30mm from the heater
Heater heating mode	Volumetric heat flux, temperature boundary condition
Boiling mass transfer model	Lee, Schrage
Under-relaxation factor for mass transfer during boiling	Without, with
Threshold temperature for boiling	1K, 2K, 3K
Mass transfer coefficients during boiling	Lee: 1, 2, 5, 10, with accommodation coefficients for the Schrage equation at the interface of 0.01 and 0.001 Schrage: Single accommodation coefficients of 0.1 to .00001; accommodation coefficients for boiling and evaporation of 0.1 and condensation of 0.00001 to 0.001; accommodation coefficients for boiling of 0.1, accommodation coefficients for evaporation at the interface of 0.001 to 0.05, and accommodation coefficients for condensation of 0.00001 to 0.00005
Algorithm	Explicit VOF with first order time discretization and geometric reconstruction, Implicit VOF with bounded second order time discretization and compressive
Pressure-velocity coupling	PISO, coupled

Conclusion

The success of NASA's missions depends on the safe storage of cryogenic fluids in tanks. Temperature stratification due to heat leaks in microgravity can lead to boiling. Computational models are needed to assess the rate and extent of the pressure rise caused by boiling in microgravity.

In this work, an axisymmetric CFD model of the pressure rise in a tank due to boiling has been developed and validated against experimental data. The validation data was provided by the Tank Pressure Control Experiment, which studied tank pressurization and pressure control aboard space shuttle mission STS-52.

In the model, the mass transfer during boiling was calculated using the Schrage equation. In order to match the experimental trends, and in particular the extent of the pressure rise and the rate of the pressure decay, different accommodation coefficients had to be used for each of the three mass transfer mechanisms: evaporation and condensation at the interface, and boiling in the bulk liquid. When three different accommodation coefficient were used, the agreement between the numerical predictions and the experimental results was excellent. However, the fact that three different accommodation coefficients were needed seems to suggest that the Schrage equation is not well-suited for representing all of the three different mechanisms for mass transfer, especially those under nonequilibrium conditions.

Suggestions for Future Work

The present study analyzes the pressure rise in a tank due to boiling, when the tank is modeled as 2D axisymmetric. However, the flow due to boiling is really a 3D phenomenon; it may be best to model further cases in 3D. Although the Schrage equation was able to produce the desired pressure rise, other mass transfer models may be more appropriate for boiling. Spurious velocities in the VOF model may have affected the results; further investigations might focus on reducing or eliminating these. The microlayer was neglected during boiling; further models may need to include this, especially if heat transfer is important. Boiling may need to be restricted to fluid regions next to solid

surfaces. It may be best to make the start of boiling not be a user-defined parameter. The effect of noncondensable gases was neglected in this study; these may have a significant effect, for instance, on bubble size. The fluid properties were held constant; a case might be run to see if varying the fluid properties with regards to temperature has an effect on the results. Further validation against other boiling data might be attempted, for instance against one of the tests during the TPCE/TP experiment which experienced explosive boiling.

BIBLIOGRAPHY

- AK Steel Corporation. (2007). *Product Data Sheet: 304/304L Stainless Steel*. Retrieved 2013, from http://www.aksteel.com/pdf/markets_products/stainless/austenitic/304_304L_Data_Sheet.pdf
- ANSYS. (2013a). *ANSYS Fluent Theory Guide*. Canonsburg: ANSYS Inc.
- ANSYS. (2013b). *ANSYS Fluent User's Guide*. Canonsburg: ANSYS Inc.
- Aydelott, J. C. (1967). Effect of Gravity on Self-Pressurization of Spherical Liquid-Hydrogen Tankage. *NASA TN D-4286*.
- Barrett, J., & Clement, C. (1992). Kinetic Evaporation and Condensation Rates and Their Coefficients. *Journal of Colloid and Interface Science*, 150(2), 352-364.
- Barsi, S., Panzarella, C. M., & Kassemi, M. (2007). An Active Vapor Approach to Modeling Pressurization in Cryogenic Tanks, AIAA Paper 2007-5553. *the 43rd AIAA/ASME/SAE/ASEE Joint Propulsion Conference*. Cincinnati, OH.
- Bentz, M. D. (1993). Tank Pressure Control in Low Gravity by Jet Mixing. *NASA Contractor Report 191012*.
- Bentz, M. D. (5/15/2014). Email.
- Cengel, Y. A., & Boles, M. A. (2006). *Thermodynamics: An Engineering Approach* (5th ed.). New York, NY: McGraw-Hill.
- Cengel, Y. A., & Ghajar, A. J. (2007). *Heat and Mass Transfer: Fundamentals and Applications* (4th ed.). New York: McGraw-Hill.

- Cipolla Jr. , J. W., Lang, H., & Loyalka, S. K. (1974). Kinetic theory of condensation and evaporation. II. *The Journal of Chemical Physics*, 61(1), 69-77.
- Dhir, V. K., Warrier, G. R., & Aktinol, E. (2013). Numerical Simulation of Pool Boiling: A Review. *Journal of Heat Transfer*, 135, 1-17.
- Eds. Linstrom, P. J., & Mallard, W. G. (2011). *NIST Chemistry WebBook*. (National Institute of Standards and Technology) Retrieved October 21, 2013, from NIST Standard Reference Database Number 69: <http://webbook.nist.gov>
- Engineer's Handbook. (2006). *Reference Tables--Surface Roughness Table*. (Engineer's Handbook) Retrieved May 29, 2014, from <http://www.engineershandbook.com/Tables/surfaceroughness.htm>
- Hasan, M. M., & Balasubramaniam, R. (2012). Analysis of the Pressure Rise in a Partially Filled Liquid Tank in Microgravity with low Wall Heat Flux and Simultaneous Boiling and Condensation. *AIAA*.
- Hasan, M. M., Lin, C. S., Knoll, R. H., & Bentz, M. D. (1996). Tank Pressure Control Experiment: Thermal Phenomena in Microgravity. *NASA Technical Paper 3564*.
- Holman, J. P. (2002). *Heat Transfer* (9th ed.). New York, NY: McGraw-Hill.
- Kartuzova, O., & Kassemi, M. (2011). Modeling Interfacial Turbulent Heat Transfer during Ventless Pressurization of a Large Scale Cryogenic Storage Tank in Microgravity. *American Institute of Aeronautics and Astronautics*.
- Lee, H. S., & Merte, H. (1996). Spherical vapor bubble growth in uniformly superheated liquids. *International Journal of Heat and Mass Transfer*, 39, 2427-2447.

- Marek, R., & Straub, J. (2001). Analysis of the evaporation coefficient and the condensation coefficient of water. *International Journal of Heat and Mass Transfer*, 44(1), 39-53.
- Mei, R., Chen, W., & Klausner, J. F. (1995a). Vapor bubble growth in heterogeneous boiling--I. Formulation. *International Journal of Heat and Mass Transfer*, 38, 909-919.
- Mei, R., Chen, W., & Klausner, J. F. (1995b). Vapor bubble growth in heterogeneous boiling--II. Growth rate and thermal fields. *International Journal of Heat and Mass Transfer*, 38, 921-934.
- Merte, J. H., & Lee, H. S. (1997). Quasi-Homogeneous Nucleation in Microgravity at Low Heat Flux: Experiments and Theory. *Transactions of the ASME: Journal of Heat Transfer*, 119, 305-312.
- Meyer, M. L., Chato, D. J., Plachta, D. W., Zimmerli, G. A., Barsi, S. J., Van Dresar, N. T., & Moder, J. P. (2013). Mastering Cryogenic Propellants. *Journal of Aerospace Engineering*, 26, 343-351.
- Muduwar, I. (2014, February 10-14). Two-Phase Heat Transfer. Cleveland.
- Mukherjee, A., & Dhir, V. (2004). Study of Lateral Merger of Vapor Bubbles During Nucleate Pool Boiling. *Journal of Heat Transfer*, 126, 1023-1039.
- NASA STI Program. (2012, July 18). *YouTube*. Retrieved November 25, 2013, from <http://www.youtube.com/watch?v=c6bUCI6rOqU>

- Panzarella, C., & Kassemi, M. (2002). On the validity of purely thermodynamic descriptions of two-phase cryogenic fluid storage. *Journal of Fluid Mechanics*, 41-68.
- Schrage, R. W. (1953). *A Theoretical Study of Interphase Mass Transfer*. New York: Columbia University Press.
- Sharma, P. (2006, December). *Thermodynamics of liquid-vapor phase change processes*. Retrieved June 2014, from <http://www.leb.eei.uni-erlangen.de/winterakademie/2006/result/content/course01/pdf/0102.pdf>
- Son, G., & Dhir, V. (2008). Numerical simulation of nucleate boiling on a horizontal surface at high heat fluxes. *International Journal of Heat and Mass Transfer*, 51, 2566-2582.
- Son, G., Dhir, V., & Ramanujapu, N. (1999). Dynamics and Heat Transfer Associated with a Single bubble During nucleate Boiling on a Horizontal Surface. *Journal of Heat Transfer*, 121, 623-631.
- Son, G., Ramanujapu, N., & Dhir, V. (2002). Numerical Simulation of Bubble Merger Process on a Single Nucleation Site During Pool Nucleate Boiling. *Journal of Heat Transfer*, 124, 51-62.
- Sussman, M., Smereka, P., & Osher, S. (1994). A Level Set Approach for Computing Solutions to Incompressible Two-Phase Flow. *Journal of Computational Physics*, 114, 146-159.

- van Stralen, S., Cole, R., Sluyter, W., & Sohal, M. (1975). Bubble Growth at Rates in Nucleate Boiling of Water at Subatmospheric Pressures. *International Journal of Heat and Mass Transfer*, 18, 655-669.
- van Stralen, S., Sohal, M., Cole, R., & Sluyter, W. (1975). Bubble Growth Rates in Pure and Binary Systems: Combined Effect of Relaxation and Evaporation Microlayers. *International Journal of Heat and Mass Transfer*, 18, 453-467.
- Young, J. B. (1991). The condensation and evaporation of liquid droplets in a pure vapour at arbitrary Knudsen number. *International Journal of Heat and Mass Transfer*, 34(7), 1649-1661.

APPENDIX

APPENDIX A

FLUID PROPERTIES

Freon 113 was used as the fluid in the TPCE/TP experiment (Hasan, Lin, Knoll, & Bentz, 1996).

The chemical formula for Freon 113 is 1,1,2-trichloro-1,2,2-trifluoroethane, or $C_2Cl_3F_3$ (Eds. Linstrom & Mallard, 2011). The molecular weight is 187.376 g/mol.

The saturation properties of Freon 113 were obtained from the NIST Chemistry WebBook (Eds. Linstrom & Mallard, 2011) as point data. Curve fits were created over these data points for a temperature range slightly larger than the range the experiment was run in (Hasan, Lin, Knoll, & Bentz, 1996). These curve fits are shown in Figure 58 through Figure 70.

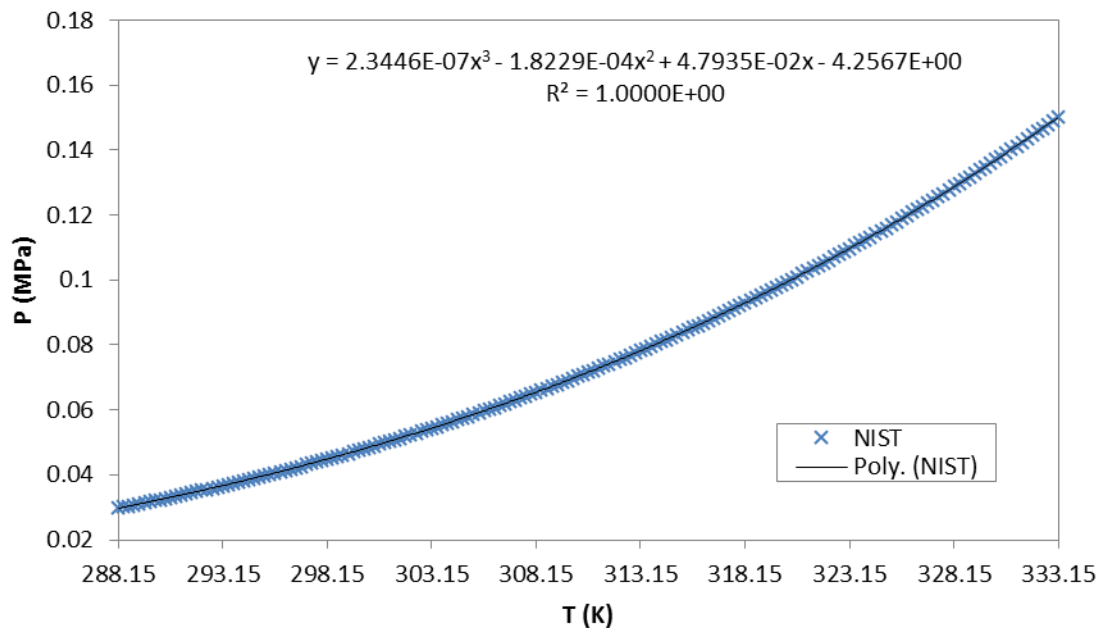


Figure 58: Saturation pressure of Freon 113

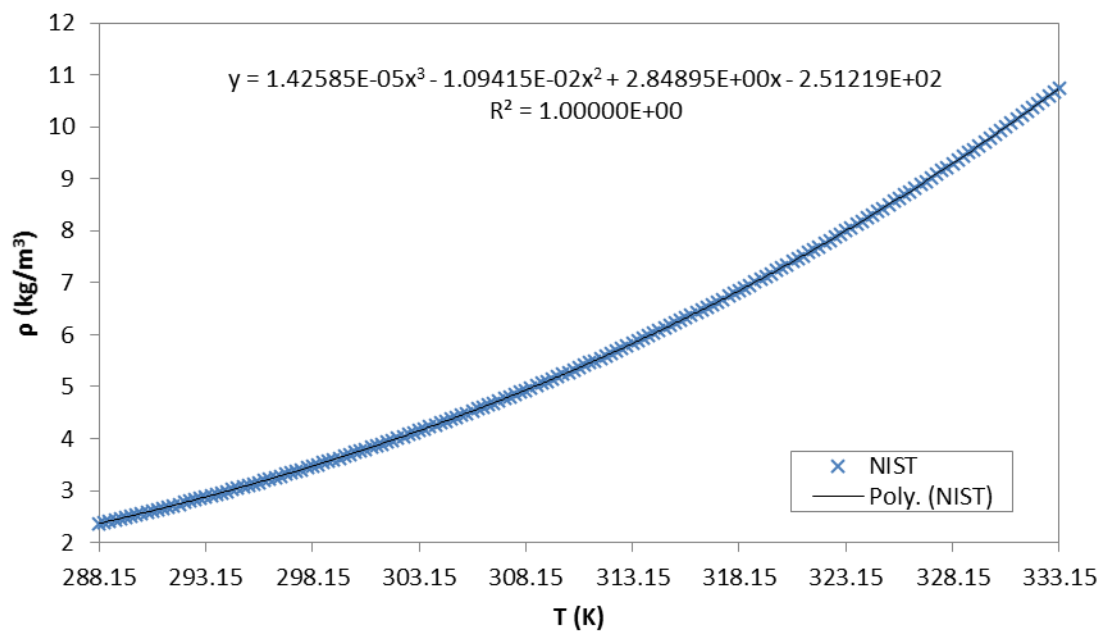


Figure 59: Vapor Density of Freon 113

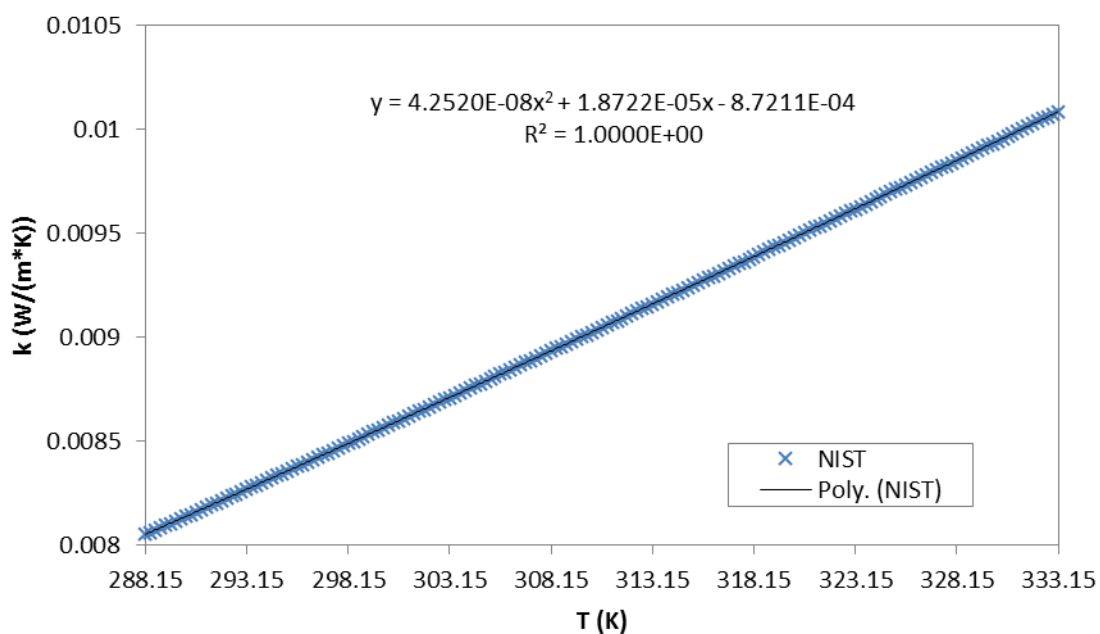


Figure 60: Vapor Thermal Conductivity of Freon 113

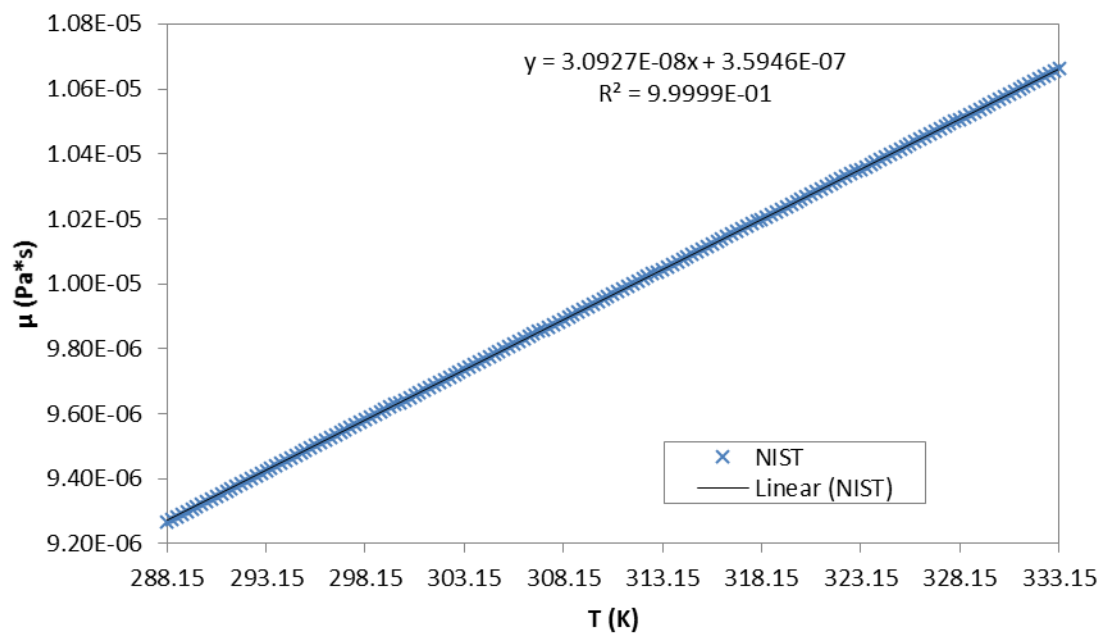


Figure 61: Vapor Viscosity of Freon 113

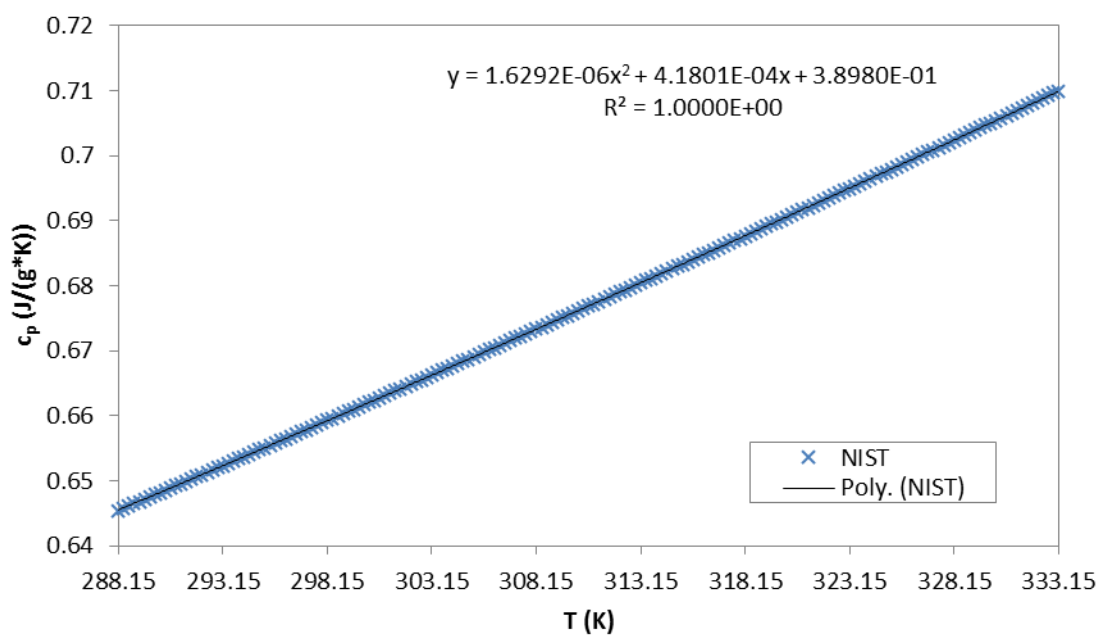


Figure 62: Vapor Specific Heat of Freon 113

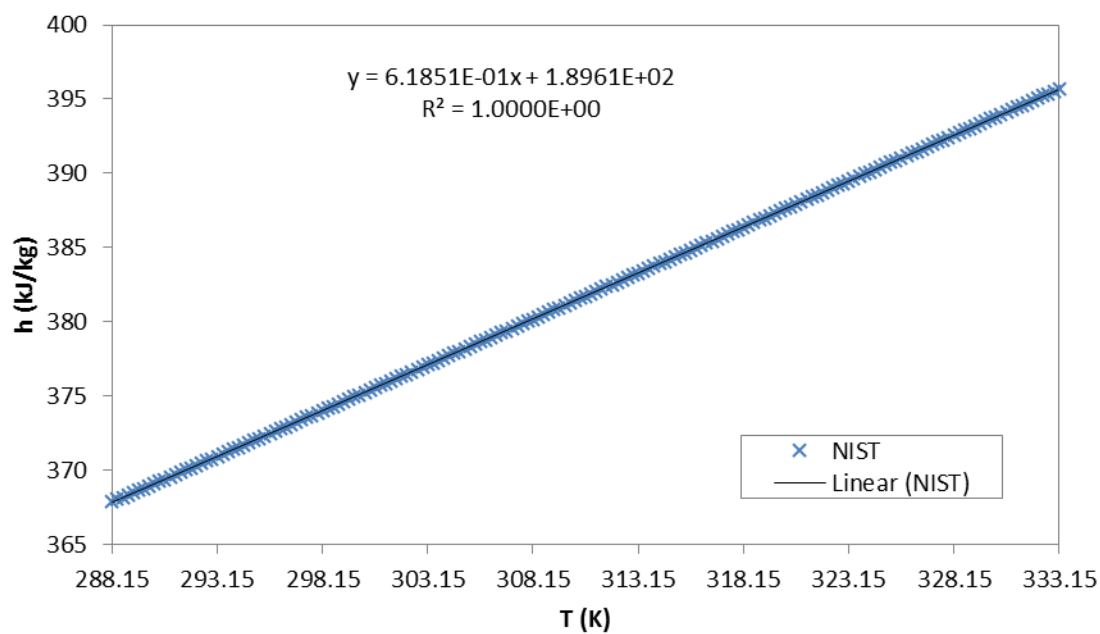


Figure 63: Vapor Enthalpy of Freon 113

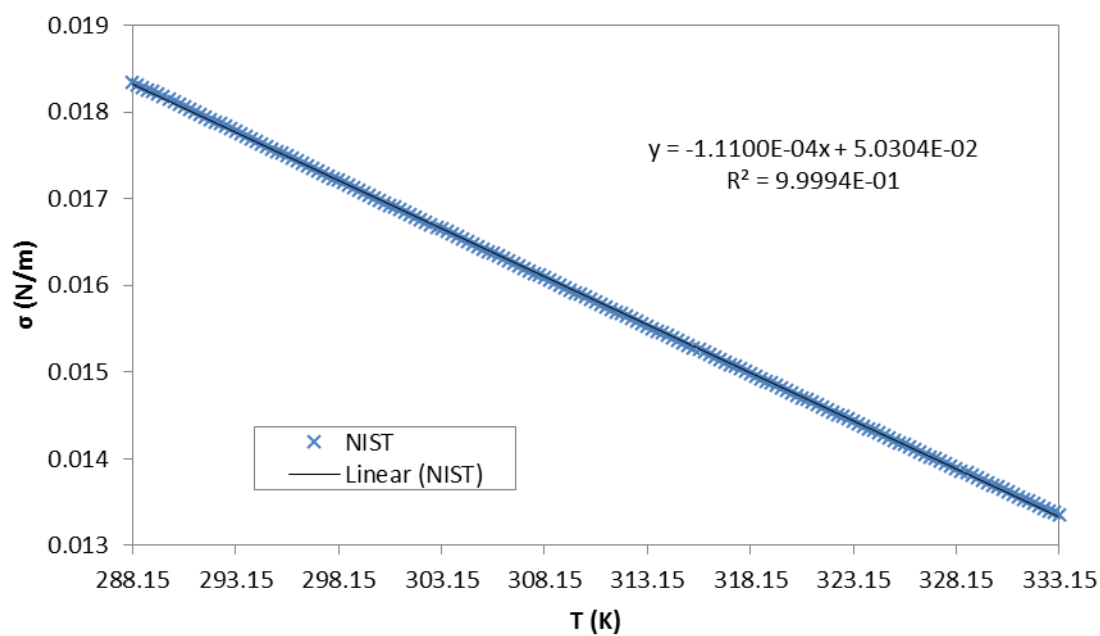


Figure 64: Surface Tension of Liquid Freon 113

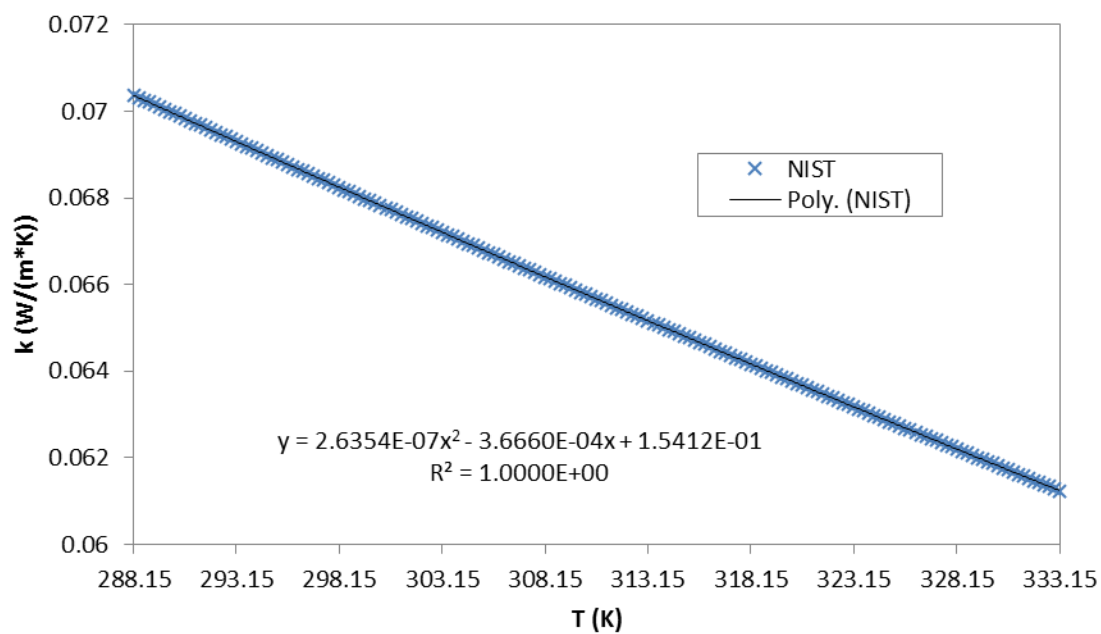


Figure 65: Liquid Thermal Conductivity of Freon 113

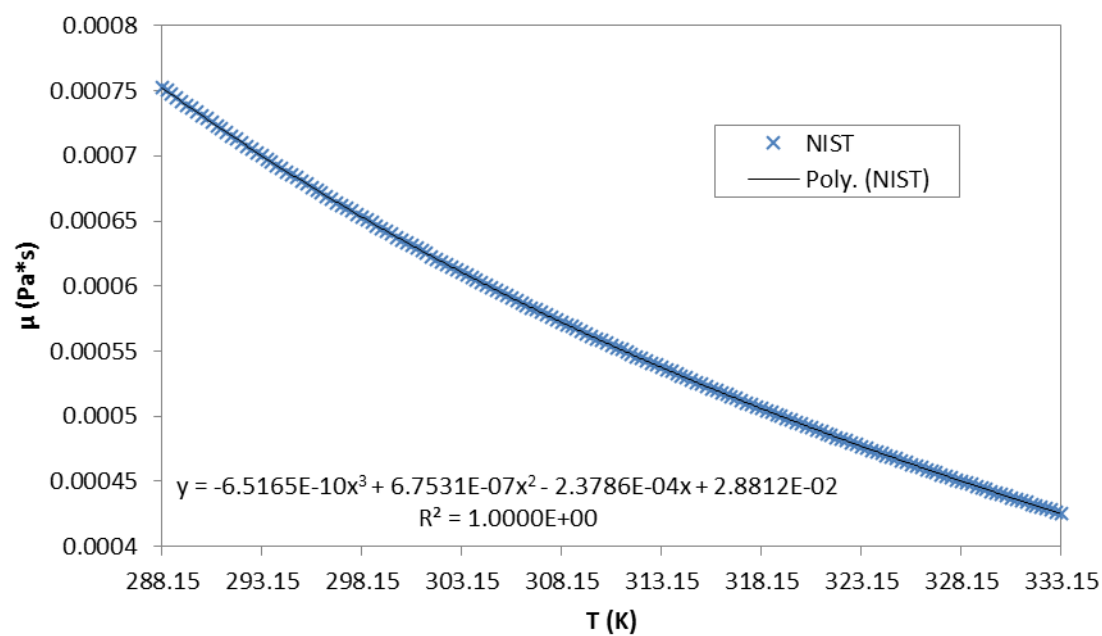


Figure 66: Liquid Viscosity

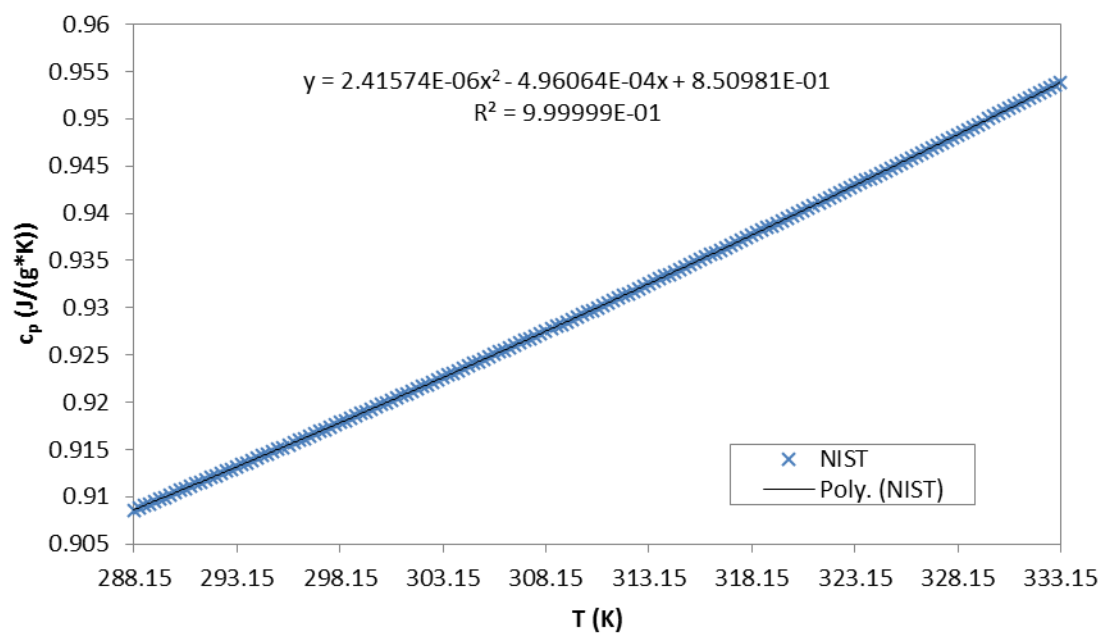


Figure 67: Liquid Specific Heat of Freon 113

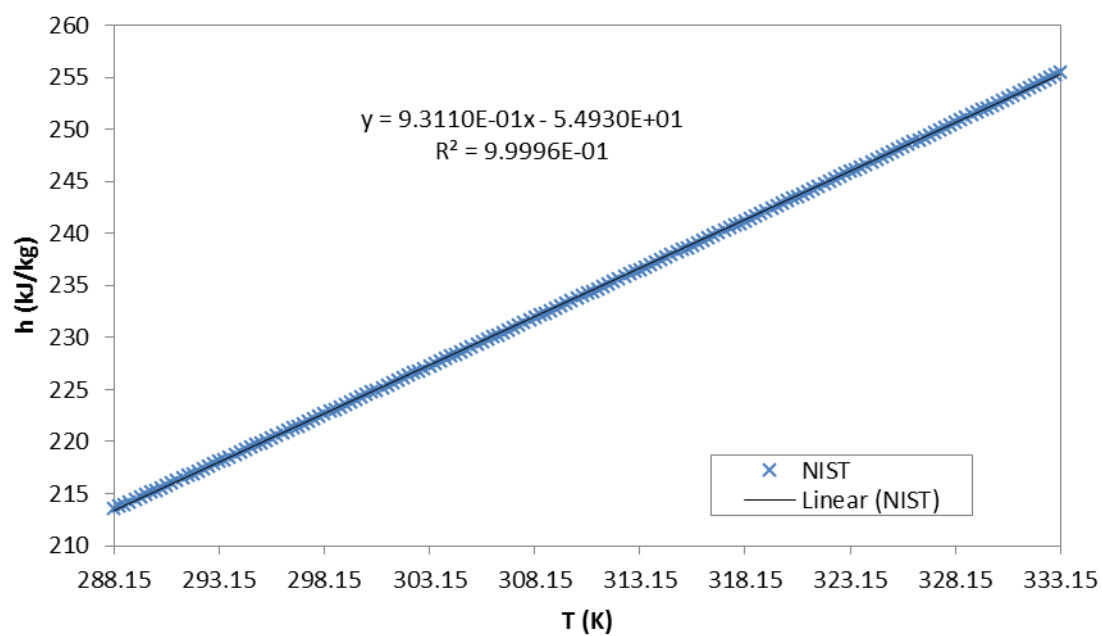


Figure 68: Liquid Enthalpy of Freon 113

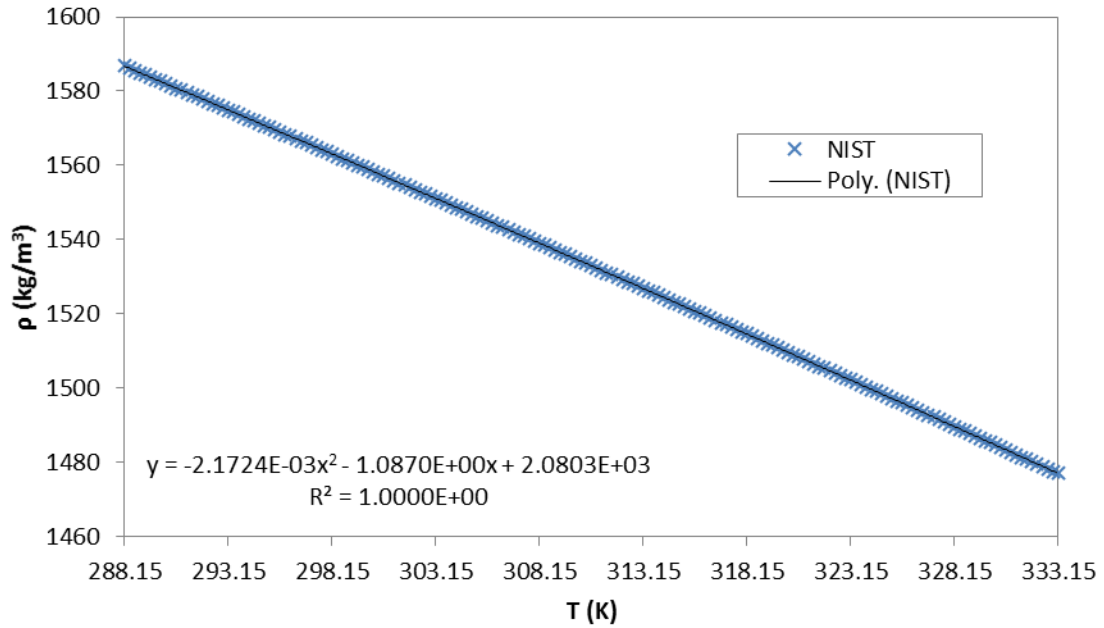


Figure 69: Liquid Density of Freon 113

The thermal expansion coefficient of Freon 113 was not given by the NIST Chemistry WebBook (Eds. Linstrom & Mallard, 2011). In order to obtain this property, the definition of the thermal expansion coefficient (Cengel & Boles, 2006) was used:

$$\beta = \frac{1}{v} \left(\frac{\partial v}{\partial T} \right)_p \quad \text{Equation 28}$$

For this calculation, the specific volume of the liquid Freon 113 under saturation conditions, as given by the NIST Chemistry WebBook, (Eds. Linstrom & Mallard, 2011) was used. The result is shown in Figure 70.

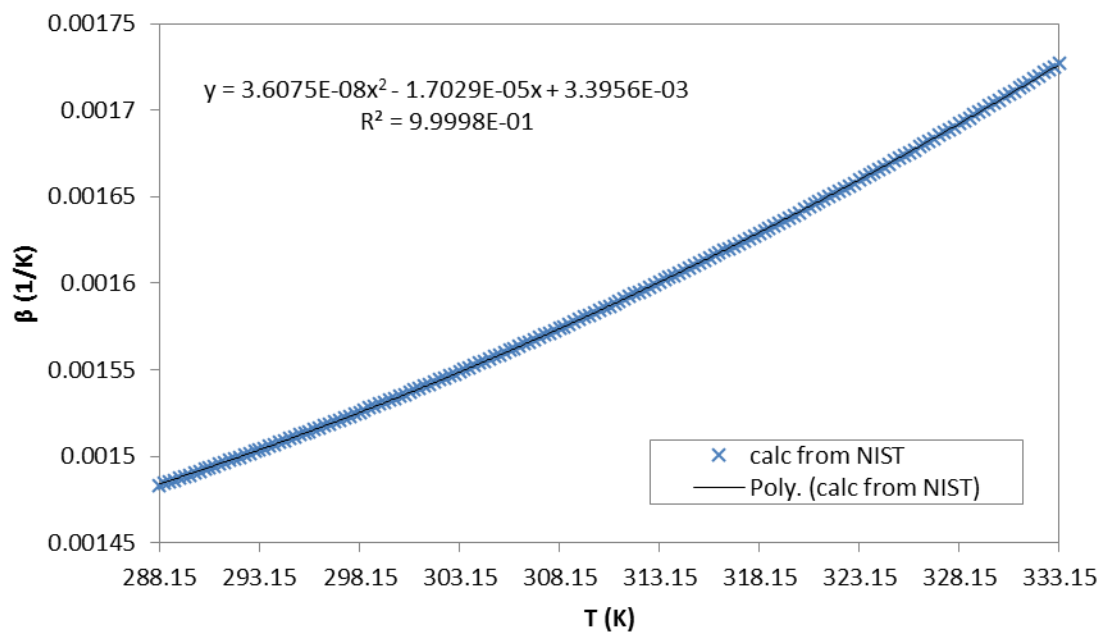


Figure 70: Liquid Thermal Expansion Coefficient of Freon 113

APPENDIX B

CURVE FITS OF THE TEMPERATURE AT HEATER A

The temperature at thermistor T3 (Hasan, Lin, Knoll, & Bentz, 1996), which was attached to heater A, was digitized for test 6. Curve fits were made of the temperature with respect to time over the entire self-pressurization and boiling periods. The equations for these curve fits are shown in Table 9; plots of these curve fits are shown in Figure 71 and Figure 72.

Table 9: Curve Fits of T3 during test 6

time (s)	Temperature (K)
$t < 14.28$	$T = 0.002709e0*t + 295.889611$
$14.28 < t < 164.7$	$T = -0.000075*t^2 + 0.06213*t + 295.056352$
$164.7 < t < 176.82$	$T = 0.0037319*t^2 - 1.417933*t + 435.5613741$
$176.82 < t < 191.04$	$T = 0.0009523*t^2 - 0.3954358*t + 341.6679248$
$191.04 < t < 210.54$	$T = -0.0130154*t + 303.3653591$
$210.54 < t < 221.88$	$T = -0.0353616*t + 308.0701212$
$221.88 < t < 255.18$	$T = -0.006009*t + 301.5573789$
$255.18 < t < 271.56$	$T = 0.0204212*t + 294.8129066$
$271.56 < t < 277.2$	$T = -0.016578*t + 304.8604255$
$277.2 < t < 291.0$	$T = 0.0009855*t + 299.9918174$
$291.0 < t < 299.4$	$T = -0.0143214*t + 304.4461357$
$299.4 < t < 313.08$	$T = 0.0127266*t + 296.3479535$
$313.08 < t < 321.54$	$T = -0.0221158*t + 307.256427$
$321.54 < t < 335.4$	$T = -0.0028788*t + 301.0709455$
$335.4 < t < 362.88$	$T = 0.0087737*t + 297.1627166$
$362.88 < t < 387.9$	$T = -0.0085042*t + 303.4282494$
$387.9 < t < 404.46$	$T = 0.0072826*t + 297.3079761$
$404.46 < t < 420.72$	$T = 0.032091*t + 287.2739657$
$420.72 < t < 431.82$	$T = -0.0084144*t + 304.3154124$

$431.82 < t < 437.34$	$T = 0.0024275 * t + 299.6336413$
$437.34 < t < 448.44$	$T = -0.0035946 * t + 302.26736$
$448.44 < t < 470.82$	$T = -0.0179133 * t + 308.6884472$
$470.82 < t < 484.62$	$T = 0.0019565 * t + 299.3333304$
$484.62 < t < 506.76$	$T = 0.0000136 * t + 300.2749333$
$506.76 < t < 523.32$	$T = 0.0040519 * t + 298.2284428$
$523.32 < t < 536.7$	$T = 0.0559865 * t + 271.0500202$
$536.7 < t < 567.3$	$T = -0.0082908 * t + 305.547699$
$567.3 < t < 575.58$	$T = 0.0048671 * t + 298.0831659$
$575.58 < t < 589.5$	$T = -0.0115158 * t + 307.5128668$
$589.5 < t < 606.3$	$T = -0.0190893 * t + 311.9774339$

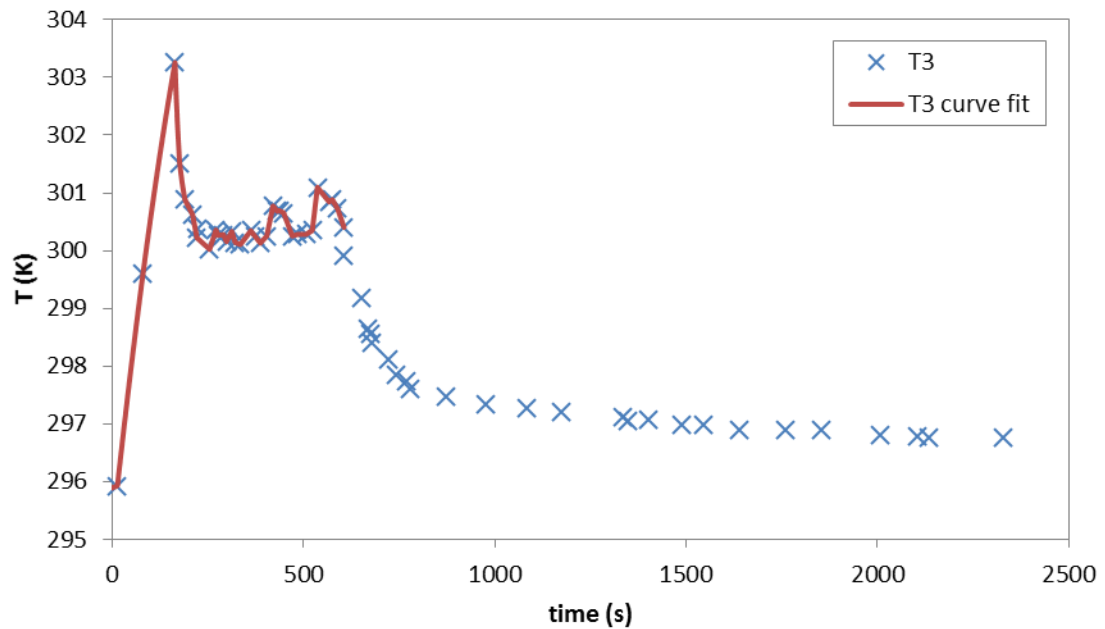


Figure 71: Curve fits of T3 during test 6

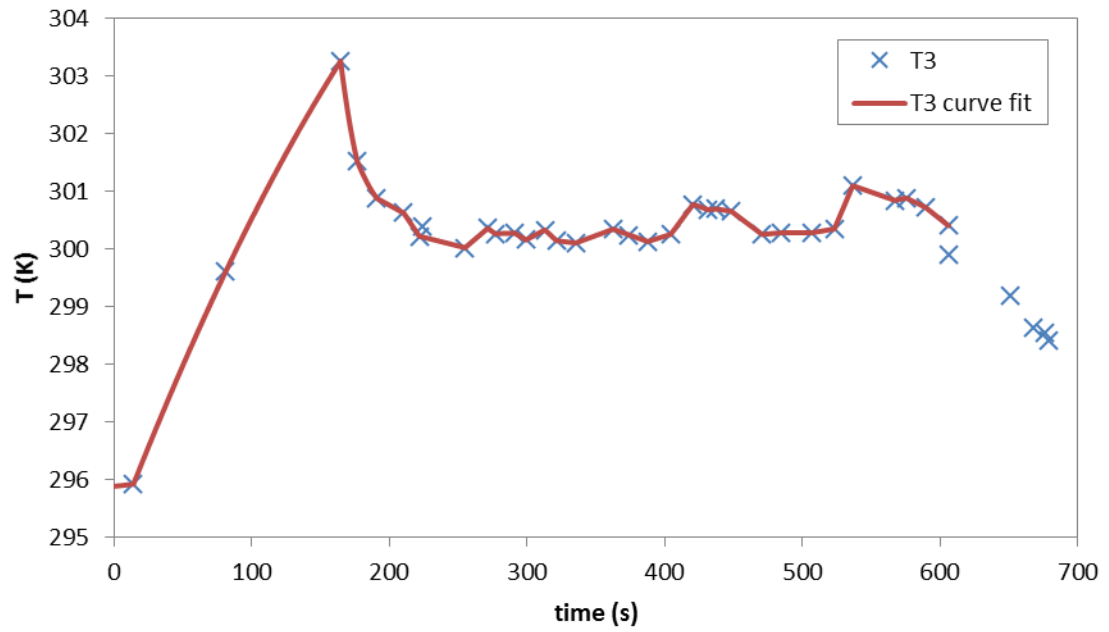


Figure 72: Curve fits of T3 during test 6: zoomed in